Switchable Surfaces: Mono- and Multilayers of Stimuli-Responsive Supramolecules on Solid Supports

Dissertation zur Erlangung des akademischen Grades
des Doktors der Naturwissenschaften (Dr. rer. nat.)

eingereicht am
Fachbereich Biologie, Chemie und Pharmazie
am Institut für Chemie und Biochemie
der Freien Universität Berlin

vorgelegt von

Thomas Heinrich, M.Sc.
aus Berlin

am 9. August 2016

Erstgutachter: Prof. Dr. Christoph A. Schalley
Zweitgutachter: Prof. Dr. Rainer Haag

Disputation am: 02.11.2016

Die vorliegende Arbeit wurde unter Anleitung von Christoph A. Schalley und Wolfgang E. S. Unger am Institut für Chemie und Biochemie des Fachbereichs Biologie, Chemie und Pharmazie der Freien Universität Berlin, an der Bundesanstalt für Materialforschung und –prüfung (BAM) sowie am BESSY-II-Elektronenspeicherring der Helmholtz-Zentrum Berlin für Materialien und Energie GmbH im Zeitraum von April 2013 bis August 2016 angefertigt.

Kurzzusammenfassung:

Rotaxane sind mechanisch verriegelte Moleküle, die als exzellente Prototypen für die Entwicklung von molekularen Maschinen gelten. Sie bestehen aus einer diskreten Anzahl an Molekülen, die über nicht-kovalente Wechselwirkungen miteinander binden. Mechanisch verriegelt bedeutet, dass eine kovalente Bindung gebrochen werden muss, um die Moleküle voneinander trennen zu können. Sind die Rotaxane außerdem mit unterschiedlichen Bindungsstellen versehen, können sie über die Anwendung eines externen Stimulus eine Konformationsänderung und dadurch eine nanoskopische Bewegung durchführen. Diese Bewegung ist in Lösung jedoch nicht gerichtet und ein makroskopischer Effekt ist dadurch, wenn überhaupt, nur sehr schwer zu realisieren. Die Einbettung von Rotaxanen in ein Bezugssystem z.B. durch die Immobilisierung auf einer Oberfläche gilt als eine vielversprechende Möglichkeit, die erzeugte nanoskopische Bewegung in einen makroskopischen Effekt umzuwandeln.

Im Rahmen dieser Arbeit wurden Chlorid-schaltbare Rotaxane mithilfe verschiedener Methoden auf Oberflächen immobilisiert. Im Detail handelt es sich bei den angewendeten Methoden um die metallinduzierte Schicht-auf-Schicht-Selbstassemblierung (*layer-by-layer self-assembly*, LbL) und die kovalente Abscheidung mittels Click-Chemie, die gegensätzliche Ansätze darstellen.

Bevor jedoch die Rotaxane immobilisiert werden konnten, wurde zunächst auf Grundlage von früheren Ergebnissen durch die Verwendung von verschiedenen Makrozyklus- und Gastmolekülen die Anwendung der genannten Abscheidungsmethoden etabliert und sukzessive verbessert. Dabei wurden unterschiedliche Templatschichten – so genannte *self-assembled monolayers* (SAMs) – verwendet, die je nach Gebrauch mit Pyridin oder Terpyridin (für die metallinduzierte LbL-Abscheidung) oder mit Azid (für den kovalenten Ansatz) terminiert sind.

Hierbei konnten folgende Ziele erreicht werden: Die Abscheidung von diterpyridin-funktionalisierten Makrozyklen in Multilagen mit einer Vorzugsorientierung wurde mit Transmission-UV/Vis, Röntgenphotoelektronenspektroskopie (XPS) sowie Röntgen-Nahkanten-Absorptions-Spektroskopie (NEXAFS) untersucht und nachgewiesen. Zur Herstellung der Multischichten wurden abwechselnd Metallionen und Makrozyklen auf verschiedenen SAMs abgeschieden. Um eine weitere Prozesskontrolle für die LbL-Abscheidung zu ermöglichen, wurde Flugzeit-Sekundärionen-Massenspektrometrie (ToF-SIMS) mit der Analysemethode Principal Component Analysis (PCA) kombiniert und gezeigt, dass damit selbst kleinste Unterschiede in der Abscheidungsprozedur nachgewiesen werden können. Durch die Verwendung von zwei unterschiedlichen Makrozyklen und vier Metallen konnte eine gemischte Multilage hergestellt werden, die sich durch die Abscheidungssequenz programmieren lässt. Bei der Behandlung der Multilagen mit geeigneten Gastmolekülen konnte einerseits gezeigt werden, dass die Makrozyklen bis in die tiefgelegenste Lage durch einen externen Stimulus adressierbar sind und

andererseits, dass sie in der Lage sind – trotz ihrer dichten Packung – eine relativ große Menge des Gastes zu binden. Darüber hinaus konnte gezeigt werden, dass die kovalent abgeschiedenen Supramoleküle auch in der Lage sind, Gäste aufzunehmen und sich deren Struktur anzupassen. In beiden Fällen wurde die Reversibilität durch geeignete Experimente belegt. Abschließend konnte durch die Einführung von Pyridin-funktionalisierten Nanopartikeln in die Multilagen die Gastaufnahme erhöht werden, was durch die Verringerung der Makrozyklusordnung aufgrund der ungleichmäßigen Oberfläche der Nanopartikel zu erklären ist.

Aufbauend auf diesen Ergebnissen wurde anschließend die Abscheidung der Rotaxane mithilfe von verschiedenen Analysemethoden wie Transmission-UV/Vis, XPS und Rasterkraftmikroskopie (AFM) etabliert und ein regelmäßiges Schichtwachstum gezeigt. Außerdem wurde mithilfe von NEXAFS-Spektroskopie beobachtet, dass die koordinativ abgeschiedenen Mono- und Multilagen durch Chlorid-Zugabe zwischen zwei geordneten Zuständen geschaltet werden können. Daraus lässt sich eine konzertierte Schaltung der Rotaxane auf der Oberfläche schließen. Die kovalent immobilisierte Rotaxanschicht dagegen zeigt nach der Chlorid-Zugabe keinen linearen Dichroismus auf. Jedoch wurde der geordnete Zustand nach der Entfernung der Chlorid-Ionen wieder beobachtet, was wiederum auf eine konzertierte Schaltung schließen lässt. Durch Kontaktwinkelmessungen konnte darüber hinaus eine Veränderung der Oberflächenbenetzbarkeit gezeigt werden. Durch die Verwendung von verschiedenen Templatschichten wurde außerdem gezeigt, dass für eine geordnete Multilage sowie eine konzertierte Schaltung eine dichte Packung der Rotaxane notwendig ist.

Abstract:

Rotaxanes are mechanically interlocked molecules (MIMs) that are considered to be excellent prototypes for the development of molecular machines. They comprise a discrete number of molecules that are bound to each other via non-covalent interactions. Mechanically interlocked means that a covalent bond must be broken in order to separate the molecules from another. If the rotaxanes are furthermore provided with different binding sites, they can perform a conformational change and thus a nanoscopic movement by the application of an external stimulus. However, this movement is not directed in solution and a macroscopic effect is therefore, if at all, very difficult to realize. The integration of rotaxanes into a reference system by, for example, the immobilization on a surface is regarded as a promising approach to convert the generated nanoscopic motion into a macroscopic effect.

The present work describes the immobilization of chloride-switchable rotaxanes onto surfaces using a variety of methods. In detail, the applied methods are the metal-mediated layer-by-layer (LbL) self-assembly and the covalent deposition using click chemistry, which can be considered as separate approaches. Before the rotaxanes were immobilized, the deposition methods were first established and gradually improved on the basis of earlier results by using different macrocycle and guest molecules. Various template layers – so-called self-assembled monolayers (SAMs) – were used. These are terminated with pyridine or terpyridine for the metal-induced LbL deposition. Azide-terminated SAMs are used for the covalent deposition.

In the course of that, the following objectives were achieved: The deposition of diterpyridin functionalized macrocycles in multilayers with a preferential orientation was investigated and verified by transmission-UV/Vis, X-ray photoelectron spectroscopy (XPS) as well as near edge X-ray absorption fine structure (NEXAFS). In order to produce the multilayer, metal-ions and macrocycles were alternately deposited onto various SAMs. To enable further process control for the LbL deposition, Time-of-Flight Secondary Ion Mass Spectrometry (ToF-SIMS) has been extended by use of Principal Component Analysis (PCA) which is capable of analyzing even very small changes in the deposition procedure. By using two different macrocycles and four metals, a mixed multilayer was fabricated that can be programmed by its deposition sequence. The treatment of the multilayers with appropriate guest molecules showed that they are on one hand addressable to the lowest layer by an external stimulus and that they are on the other hand able to incorporate a relatively large amount of the guest. Additionally, the covalently deposited supramolecules are also able to bind guests and to adapt to their structures. In both cases, the reversibility could be shown by appropriate experiments. Finally, the introduction of pyridine-functionalized nanoparticles into the multilayers led to a higher guest uptake, which can be explained by the reduction of the macrocycle-order due to the uneven surface of the nanoparticles.

Based on these results, the deposition of the rotaxanes was established and a regular layer growth was shown by various analytical methods such as transmission-UV/Vis, XPS and atomic force microscopy (AFM). It was observed that the coordinately deposited mono- and multilayers can be switched between two ordered states by the addition of chloride-ions. This effect was ascribed to the presence of a coupled rotaxane-switching in the multilayer. In contrast to that, the covalently immobilized rotaxane-layer showed no orientational effect after chloride addition. However, the ordered state was again observed after removal of the chloride-ions, which in turn indicates a coupled switching. Furthermore, a change of surface wettability was shown by contact-angle measurements. The utilization of different template layers showed that a dense packing of the rotaxanes is necessary for an ordered multilayer and a coupled switching.

Table of Contents

1. Introduction

The creation of miniature factories or machines was already envisioned in the late 1950s by Robert Feynman when chemists and physicist did not have the necessary analytical techniques to investigate the proposed motion or fabrication at the nanoscale. In his lecture "There's plenty of room at the bottom", he led the audience to all kinds of new possibilities, forces, effects, and different manufacturing problems in the nano-realm.[1] Since then, the ability to control and manipulate matter or processes on the atomic or molecular scale has inspired a large number of scientists to unravel arising questions and problems in this field called nanotechnology. Therefore, it became one of the most promising future technologies in today's research – potentially delivering groundbreaking solutions to major problems in material science, medicine, as well as data and energy storage. In particular, the development of sophisticated analytical techniques like NMR, electron microscopy or mass spectrometry – just to name a few – made a large number of breakthroughs in molecular nanotechnology possible.

Taking the scientific progress in the last three decades in the field of molecular nanotechnology into account, it can be concluded that mechanical motion and the manipulation of objects at the nanoscale is not a vision anymore. Outstanding examples of molecular nanotechnology have been developed in the last years where single molecules can externally be addressed, show intramolecular motion, are able to transport molecular or nanoscopic cargo, or catalyze chemical transformations towards a desired product.[2] For example, David Leigh and coworkers have created a small molecule that is able to target a cargo molecule, pick it up, place it in a new position and release it.[3] While such a sequence of actions is trivial on a macroscopic scale, synthetical achievement of this with small molecules is unique. Furthermore, the researchers around Jong Hyun Choi have developed a synthetic DNA motor that transports nanoparticles along carbon nanotubes over the course of 2 µm responding to the increase of Mg^{2+} concentration and thus mimicking the path of the kinesin complex along a cytoskeletal fiber.[4]

However, giving nanoscale motions a clear and determined direction on a larger scale let alone harnessing this motion seems to be a major goal and a huge obstacle at the same time. Although, the few examples that have been reported are sophisticated in their structure and arise from a complicated synthesis, their performance is rudimentary and does not fulfill a useful task above and beyond the molecular scale.[5] Obviously, individual molecules cannot move or manipulate cargo that is several orders of magnitude larger than themselves. This is due to the fact that molecular switches reported in solution underlie the principle of Brownian motion which makes them move around randomly and therefore the mechanical motion is cancelled

out when a large number of molecules is considered. This is in fact the main distinction between a molecular switch and a machine: No net-effect is gained from molecular switches. A macroscopic output (or net-effect) can only be achieved when a large number of molecular switches is integrated into an array with a superior order where they can perform tasks, motion or build up structures in concert, synchronous and aligned. In other words, the switches need to have a certain reference system that minimizes the degrees of freedom hindering a mechanical, directional motion over larger arrays. This reference system gives rise to a feature that is not achievable by conventional devices and that also enables future application: Possible movements of these machines cover the range of Ångstrøms which leads to an actuation that has a molecular-scale precision.

A similar phenomenon can be found in natural molecular machines. Static complexes use lipid membranes as reference systems in order to gain directionality. ATP synthase in particular uses the energetically favored proton transport along a proton gradient in order to perform a rotational motion within its synthase complex. This torsional moment is then used to liberate previously formed ATP – energy is converted from one form to another. For a simple replication however, this and biological molecular machines in general are far too complex. Therefore, other approaches to produce artificial molecular machines have to be found.

In order to design suitable molecules for artificial molecular machinery, one has to break away from the classical top-down approach where macroscopic devices are taken and miniaturized for their implementation on a much smaller scale. This worked well for transistors in data storage which have excessively been reduced in their size in the last decades. However, this development has its limits: Different problems and properties arise when mechanical elements work on the molecular scale. For example, switching or actuation differs very much from that at the macroscopic level and no clear separation of cause and effect is present anymore. In fact, the activation of a molecular switch leads to the change in relative energies of two possible conformational states but the actual switching between the two states is ultimately driven by thermal noise.

The bottom-up approach serves as an alternative. As in natural systems, molecular self-assembly is exploited to fabricate functional architectures from small molecules. Stimuli-responsive mechanically interlocked molecules (MIMs) such as bistable rotaxanes, that share the same topology as ATP synthases and bacterial flagellar motors, are assembled in this way. They comprise at least two different components that are able to move relatively to each other when treated with an external stimulus. This makes them excellent precursors for the development of artificial molecular machines that can deliver a macroscopic effect. Various of these structures have already been designed that exhibit impressive and diverse machine-like behaviors. As already stated, they however need to be incorporated into a suitable reference

system to get a directional motion that can be harnessed. Several examples have been reported where MIMs are either immobilized at interfaces, on surfaces[6] or into metal organic frameworks (MOFs).[7] A detailed understanding of the factors that induce a coupled or concerted switching should allow to determine the steps that are needed to achieve directional motion or even a macroscopic effect.

2. Motivation

The fundamental idea behind this work is to provide evidence for a coupled molecular switching of chemically-addressable interlocked molecules in mono- or multilayers on solid supports. The term coupled in this work refers to the switching of whole arrays of rotaxane switches that are aligned in a well-ordered state before and after switching. Furthermore, a reversible switching is only provided when the initial order is completely restored.

On the basis of template layers that have already been established in the course of the overall project, it is desired to fabricate multilayers of switchable rotaxanes on solid supports by a layer-by-layer (LbL) approach. The utilized template layers either have pyridine- or terpyridine-termini to deposit a linking metal-ion layer. Subsequently, supramolecules such as tetralactam macrocycles, that are doubly functionalized with pyridines or terpyridines, can be immobilized. If the last two steps are repeated in an alternate fashion, a multilayer of the used molecule can be obtained. The main advantages of this layer-by-layer self-assembly lie in the convenience of its utilization and that it delivers reproducible results as it uses the dynamic error correction of self-assembly. If the molecules are – as a result – densely packed, the layers are expected to be preferentially oriented which is one essential element for the development of a directional switching. To ensure a thorough analysis of the rotaxane multilayers, it is desired to develop and establish an efficient approach for the deposition of analogous macrocycle multilayers first and follow their self-assembly with suitable analytical methods.

The following steps shall be taken to achieve this aim of the thesis:

(I) Suitable macrocycles and rotaxanes for surface deposition shall be synthesized.

(II) The macrocycles are deposited into programmable multilayer with different metal-ions followed by X-ray photoelectron spectroscopy (XPS) and transmission-UV/Vis spectroscopy.

(III) In order to ensure the deposition of high-quality layers, principal component analysis (PCA) assisted time-of-flight secondary ion mass spectrometry (ToF-SIMS) shall be introduced as a process control with a high sensitivity for impurities as well as imperfections in the layer structure.

(IV) Employing two differently functionalized macrocycles is ought to deliver multilayers of a higher complexity and a designed sequence. This shall act as a proof-of-concept for multilayers that are built up with different rotaxanes. The stepwise growth of these multilayers shall be also investigated by XPS, ToF-SIMS, and transmission-UV/Vis to ensure the sequential programmability.

(V) Additionally, near-edge X-ray absorption fine-structure (NEXAFS) spectroscopy is used to investigate whether the multilayers are preferentially oriented.

(VI) To show the accessibility of the multilayers for an external stimulus, they are treated with squaraine guests that have an optical read-out for their incorporation into the macrocycle.

(VII) By integrating nanoparticles into the multilayers, their order shall be reduced which shall lead to a higher uptake of guest molecules.

(VIII) Different supramolecules such as crown ethers, tetralactam macrocycles, ammonium ions, and diketopiperazines are covalently immobilized onto an azide-terminated self-assembled monolayer (SAM) through a copper-catalyzed azide-alkyne cycloaddition (CuAAC). The accessibility for an external stimulus shall be shown by the reversible deposition of the particular counterpart which is then investigated by XPS and NEXAFS. The covalent immobilization of supramolecules stands in marked contrast to the metal-mediated self-assembly of multilayers on surfaces: An error-correction is not possible.

(IX) On the basis of the gained results, the desired mono- and mulitlayers of switchable rotaxanes are built by metal-mediated LbL self-assembly and the covalent click chemistry approach. Furthermore, the switching behavior of these rotaxanes should be investigated in terms of surface-wettability and well as orientation. Two different template layers are available for that. One pyridine-terminated monolayer that has a rigid structure and a terpyridine-terminated SAM with a flexible structure.

The long-term goal of the overall project is to establish programmable multilayers of rotaxanes that can be switched by different stimuli as depicted in Figure 1. This should lead to an independent switching in every layer that can therefore be addressed in an orthogonal fashion. Depending on the rotaxane, the switching stimuli can be chemical, electrochemical or photochemical. If the rotaxanes are further equipped with opposite stopper units, the direction of the switching can be enhanced and lead to a macroscopic read-out such as bending of a cantilever, lifting of a load or a simple change of color.

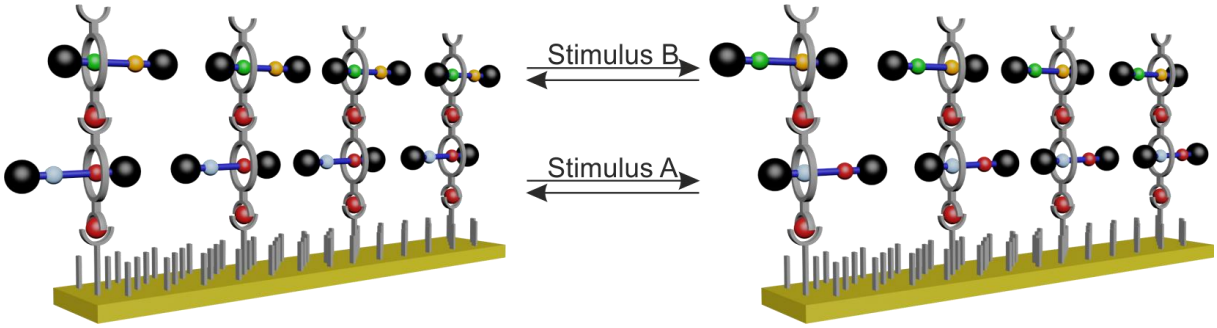

Figure 1. Illustration of a multilayer comprising two rotaxanes that are addressable with different stimuli. In detail, stimulus A switches the lower layer and stimulus B addresses the upper layer.

3. Theoretical Background

3.1. Non-Covalent Bonds in Supramolecular Chemistry

Supramolecular chemistry focuses on the association of molecules into superior structures as for example host-guest chemistry, molecular self-assembly and mechanically interlocked molecular architectures. The molecules in these structures are held together by various intermolecular, non-covalent interactions such as hydrogen-bond, Van der Waals, metal-ligand, cation-π-, π-π-, ion-ion, ion-dipole, or dipole-dipole interactions. Supramolecular complexes may also form via hydrophobic or solvophobic effects.[8] The bond strengths of intermolecular interactions are often within a certain range (Figure 2).

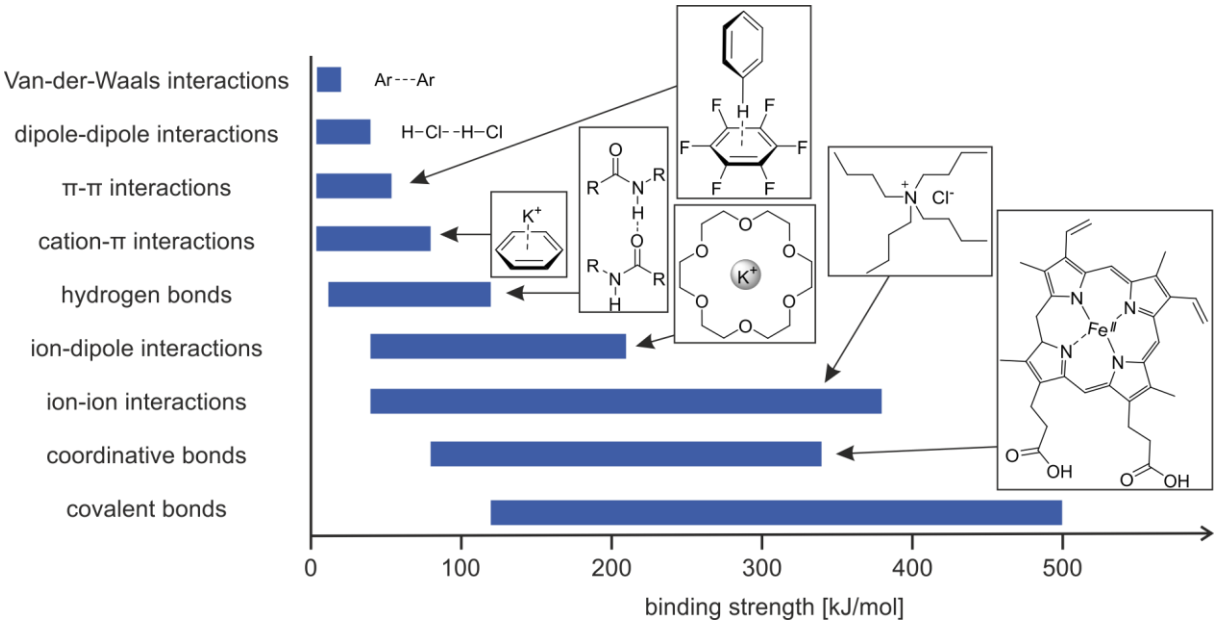

Figure 2. Typical ranges of non-covalent interactions including covalent bonding for comparison.

Non-covalent interactions also play a major role in biological systems. In enzymatic catalysis, for example, a substrate is bound by an enzyme in a catalytic pocket with the lock-and-key principle. That means, the specific binding moieties of the substrate fits in a way to the binding sites of the pocket that it has the highest possible binding affinity.

From the principle of non-covalent bonds, core-concepts of supramolecular chemistry can also be derived. One of which is called self-assembly. It refers to processes of structure and pattern formation that autonomously proceed without external influences as a consequence of specific, local interactions among the components themselves. It is defined by the following criteria: (I) The process addresses existing, separate components (eg. molecules). (II) The result is a product of the information that the individual components themselves contain (eg., charge,

mass, shape or surface properties) and thereby are decisive for their mutual interactions. Common examples include the formation of micelles, vesicles, liquid crystal phases, and Langmuir monolayers of surfactant molecules. Further examples of supramolecular assemblies demonstrate that a variety of different shapes and sizes can be obtained using molecular self-assembly. In principle, "self-assembly" is clearly seperated from "self-organization". While self-organization describes the formation of non-equilibrium structures (dissipative systems) under constant consumption of energy (“fuel”), self-assembly describes the formation of thermodynamic minimum structures. In literature, this distinction is not always clearly followed, so that - despite the clear definition - both terms are strongly mixed up. The reason could be that especially in biological systems, a combination of both mechanisms often occurs at the same time.
Supramolecular chemistry has now long developed into a field of interdisciplinary research that unites and appeals not only chemists, but also physicists, biologists and physicians. New, independent research fields have emerged, which extensively use the core concepts of supramolecular chemistry. These include areas of materials science and nanotechnology. Furthermore, the concepts of supramolecular chemistry have helped to create new chemical classes of substances such as molecular machines, non-covalent polymers, metal-organic frameworks (MOFs) and interlocked molecules.

3.2. Host-Guest Complexes

The core-concepts of supramolecular chemistry that are extensively used in this work and therefore should be discussed in more detail are host-guest chemistry and the assembly of mechanically interlocked molecules (MIMs). Here, two or more molecules are held together by specific intermolecular bonds with a smaller guest (axle) molecule that coordinates into the cavity of a larger host (macrocycle) molecule.[9] Host-guest chemistry mainly includes the idea of molecular recognition by non-covalent bonds. It should be noted that the different reception of different hosts is hereby exploited. While, for example, crown ethers or cryptands are particularly suitable as host molecules for cations, cyclodextrins encapsulate various nonpolar organic molecules through hydrophobic effects in water. Since cyclodextrins are water soluble, the trapped organic guest molecules get an improved water solubility by the complex formation.[10] Therefore, they are used in food, pharmaceutical, and chemical industries, as well as drug delivery, agriculture and environmental engineering.
Architectures of mechanically interlocked molecules (MIMs) can be regarded as an extension of host-guest chemistry. They are referred to as supramolecular complexes in which two or more molecules are joined together so that a covalent bond must be broken in order to separate the complex. A number of structures are classified as mechanically interlocked molecules which include rotaxanes or catenanes. Rotaxanes consist of at least one molecule with a linear

unit, also referred to as axle or dumbbell, and one or more cyclic molecules, the macrocycle. Catenanes, however, are systems in which two cyclic molecules are mechanically intertwined. Nomenclaturewise, it is important to know that a number in square brackets is placed in front to the word rotaxane or catenane. It stands for every single molecule involved in the complexes. In Figure 3, a pseudorotaxane is additionally shown as a precursor of a rotaxane, which resembles also a classical host-guest complex and is not mechanically locked.

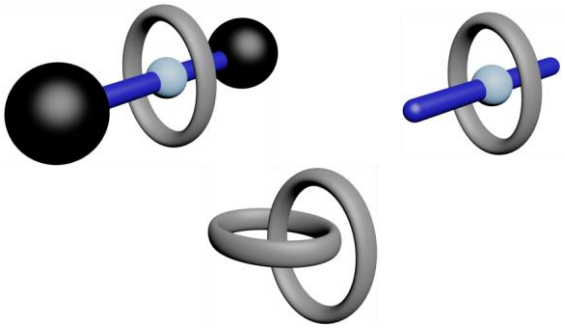

Figure 3. Schematic representation of mechanically interlocked molecules and a pseudorotaxane.

For the synthesis of rotaxanes, various methods have been developed. Four extensively used template-directed methods are shown in Figure 4. A template is – in this special case – a functional group, ion or molecule that can build up certain intermolecular forces and therefore promotes a particular product.

In this work, the rotaxanes have mainly been synthesized using the capping method. This involves the threading of an unstoppered axle into the cavity of a previously synthesized macrocycle – i.e. a pseudorotaxane is formed. This process involves an intrinsic template which, for example, utilizes hydrogen bonds or hydrophobic effects. The rotaxane is then formed by reaction of the axle molecule with suitable stoppers which prevent its dissociation without breaking a mechanical bond. The clipping method is comparable: Here, the dumbbell-shaped axis is formed before the rotaxane synthesis and binds to an incomplete macrocycle which is subsequently closed. In the case of the slipping method, both the macrocycle and the axle are formed prior to the rotaxane synthesis. During the synthesis process, the energy is increased by excessively increasing the temperature so that the kinetic barrier for the threading process is overcome. The recently developed active-template method involves the catalytic influence of a template ion to the threading of two (different) axle fragments into a cyclic molecule (macrocycle) and the formation of a covalent bond, which results in a mechanical bond between the macrocycle (host) and the axle (guest).[11]

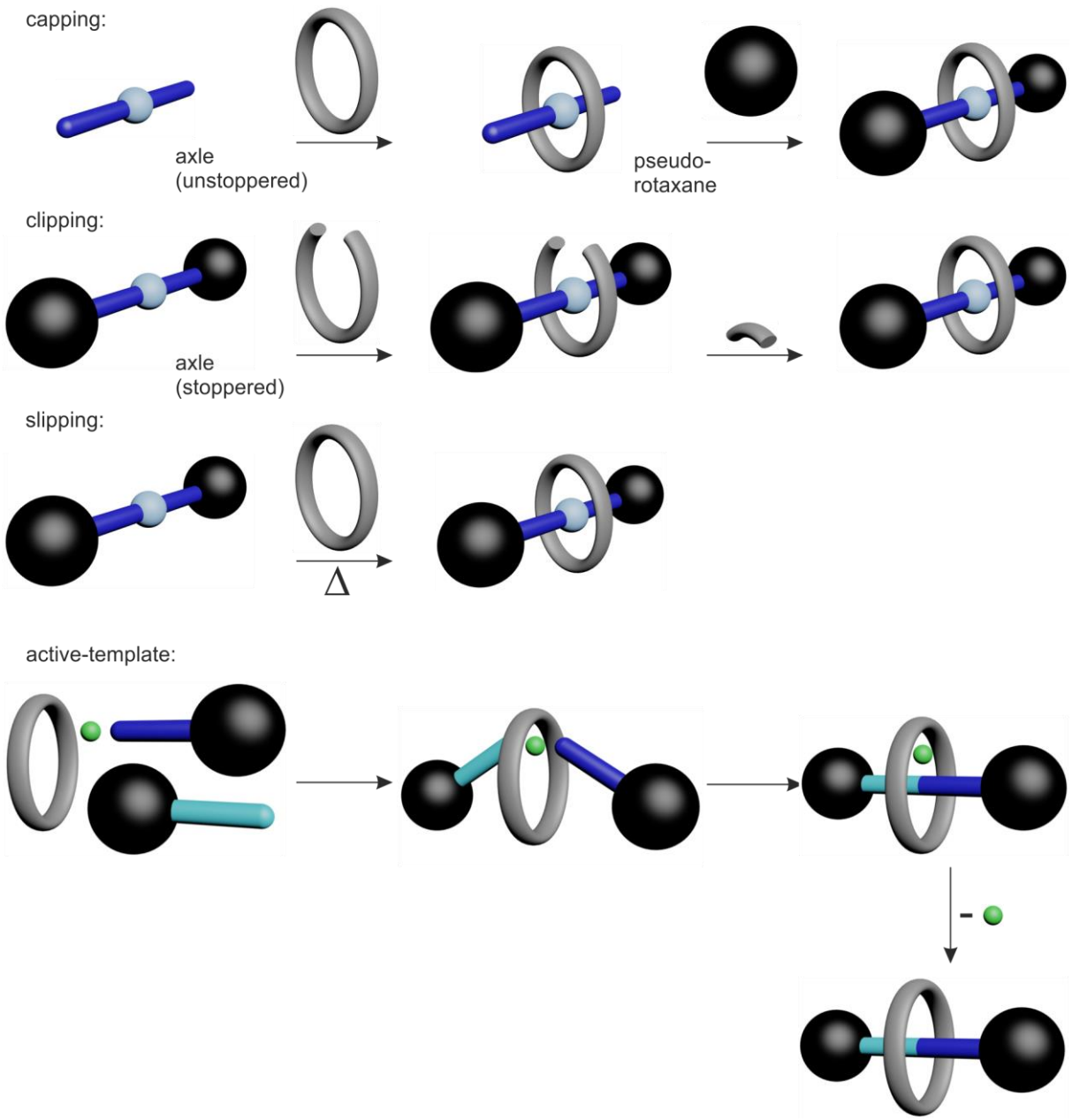

Figure 4. Overview of the main strategies for the synthesis of rotaxanes.

In this work, rotaxanes and host-guest complexes, that are based on the Hunter-Vögtle tetralactam[12] and the crown ether[13] macrocycle, were investigated. The tetralactam macrocycle is mainly characterized by the binding of anions[14] or dipoles[15] to amides in the cavity of the macrocycle via hydrogen-bonding. Furthermore, the formation of π-π interactions is possible as a template for axle threading into the macrocycle.[16]

In Figure 5, the first synthesis of a rotaxane with a tetralactam macrocycle is shown that uses an anion template effect.[17] Initially, the phenolate stopper, highlighted in red, binds into the cavity of the macrocycle through hydrogen bonds – an anionic complex is formed. This subsequently attacks the brominated methylene group of the second axle piece as it can act as a nucleophile. Thus, the rotaxane is formed.

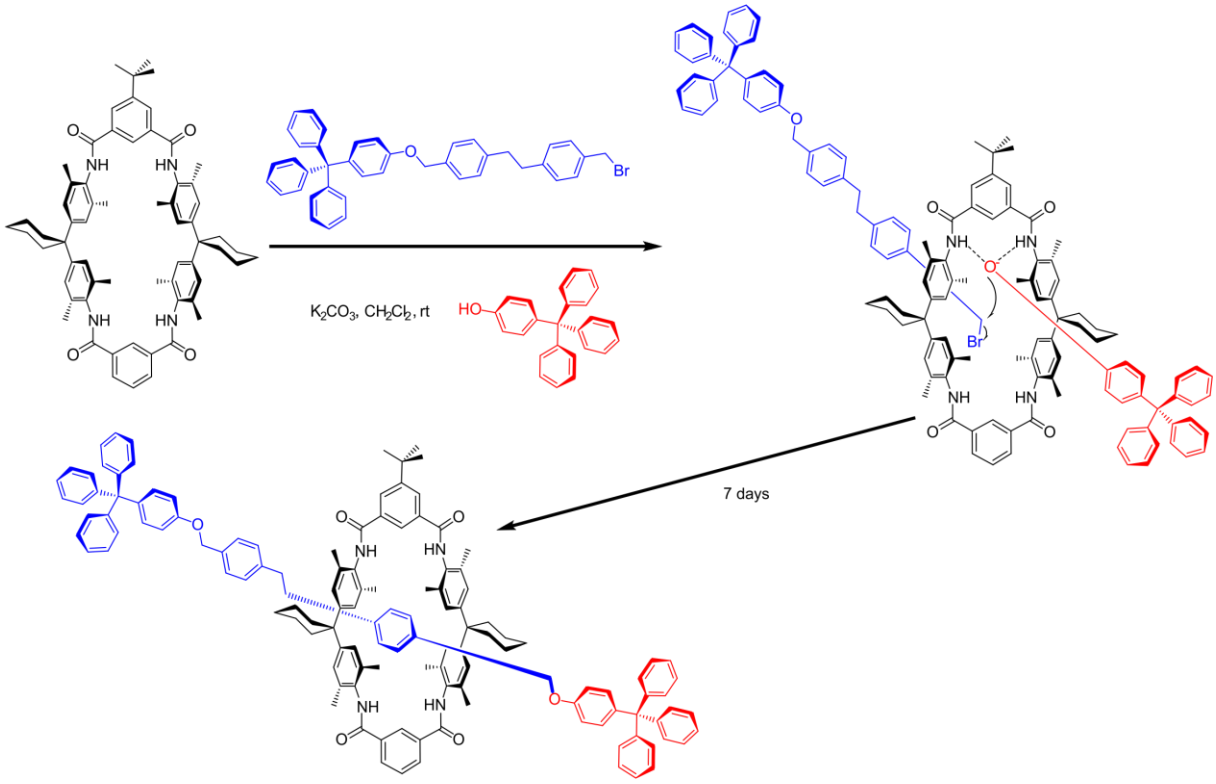

Figure 5. Synthesis of a [2]rotaxane through an anion-templating effect by Vögtle.[17]

For this project, the macrocycle is particularly appealing due to it conformational characteristics. The fact that the macrocycle, despite its rigidity, has a remarkable conformational flexibility and can thus build up an extremely dense packing in the solid state, is an essential factor.[18] Furthermore, it was demonstrated that they can form an orderly two-dimensional structure on gold surfaces.[19] Therefore, it is quite reasonable that they also exhibit a high order upon a gradual deposition on self-assembled monolayers. At the terminal isophthalic-moieties, tetralactam macrocycles can also be functionalized by organochemical cross-couplings in a straightforward fashion.[20] For the formation of macrocycle multilayers, (ter-)pyridine functionalities are particularly suitable, as they form very stable complexes with e.g. iron and nickel for terpyridines or palladium and platinum for pyridines.

In principle, the development of switchable rotaxanes is also possible with this macrocycle, which makes it even more interesting for the present work. The field of molecular switches based on rotaxanes will be subsequently discussed in more detail.

3.3. Artificial Molecular Switches

Molecular switches can be defined as molecules that are designed to change their shape in a controllable and reversible fashion under the influence of different external stimuli. Moreover, they possibly can be employed as devices that create motion (molecular motors), paving the

way towards the smallest possible entities capable of performing useful work (molecular machines). The research on artificial molecular switches and motors is indeed interdisciplinary. Organic chemists design and study diverse families of molecules capable of performing reversible switching motions. Computational chemists contribute to understanding these processes and improve the molecular designs. Colloidal, polymer, and material chemists as well as engineers provide the ability to integrate molecular switches into higher-order architectures, giving rise to macroscopic devices (see chapter 3.4.5) which physicists help to quantitatively understand (see chapter 3.5). Artificial molecular switches can also be employed in biological systems, where they are used to study and alter various biological processes like insulin secretion[21] or mitosis and cell death[22] in a field that has been named photopharmacology[23] due to the employed switching stimulus.

The class of light-switchable molecules is in fact the most prominently used in this matter. There exist numerous simple (bistable) molecular switches that undergo various types of chemical bond rearrangement upon light irradiation. One of the most widely used classes are azobenzenes.[24] It isomerizes between the *E*- and *Z*-conformations around a double bond and therefore can mimic a flapping motion. The overcrowded alkenes that have been established by Feringa *et al.*, however, behave as rotors that can revolve about a rigid internal axis.[25] Just these two molecular switches show how simple molecules can exhibit complex behavior on the nanometer scale upon an external stimulus. However, as the described intramolecular conformational changes do not provide coupled let alone controllable motion on a larger scale, the molecules have to be incorporated into arrays of more complexity as well a larger scale. MIMs and especially rotaxanes are one possibility to gain at least more complexity and controlled mechanical motion. In order to make rotaxanes switchable, their axles have to be employed with at least two different macrocycle recognition sites with different affinities. The stations should additionally reverse their affinity to the macrocycle when the rotaxane is treated with a suitable stimulus which can be chemical, electrochemical, or photochemical.[26] Figure 6 schematically shows the general mechanism of a rotaxane-switching.[27] A distinction is made between two stable states. In state a), the macrocycle binds to the preferred blue station. If an external stimulus now acts upon the rotaxane, the relative binding constant of the macrocycle to the stations changes and the second station (red → orange) becomes the preferred binding site. Consequntly, the rotaxane located in state b) illustrates an energetically unfavorable transition state. Out of this state, the macrocycle does a translation to the second station and is therefore again in a stable state (power stroke). Now, if a reaction occurs (triggered by another external stimulus), which converts the second station to its initial state (orange → red), the binding of the macrocycle to this station (state d) is again in disadvantage compared to the binding to the blue station and the macrocycle travels back to its starting position (recovery stroke).

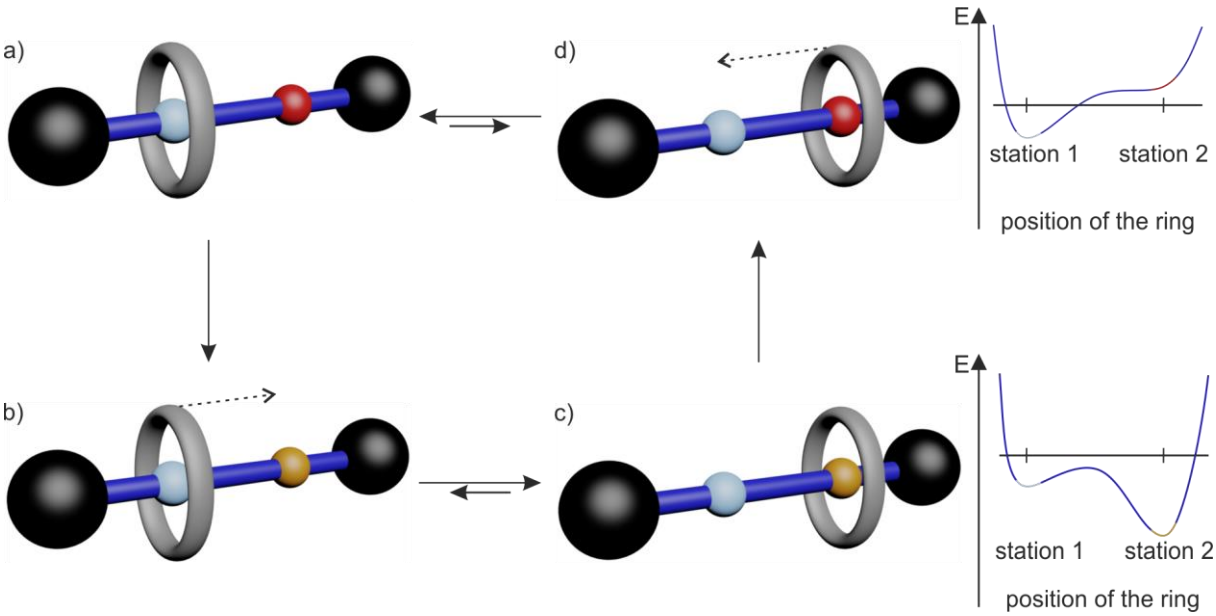

Figure 6. Switching mechanism of a bistable two-station [2]rotaxane.

The described intramolecular motion of one component in a rotaxane (MIM) relative to another gives way to different co-conformational states, which have different stabilities, as well as spectroscopic and physical properties. On the right side of Figure 6, a devised potential energy curve is schematically depicted in order to clarify the relative stability of the macrocycle binding-states: In order to discretely observe the two different binding states, they need to have sufficiently high binding energy differences. As a result, at room temperature, an energy difference ($\Delta\Delta G$) of 8.4 kJ·mol^{-1} between the binding of the macrocycle at the two axle-binding stations has to be present, so that the macrocycle binds to the better binding station in 95% of the times.

The first examples of a switchable MIM represent two station rotaxanes or catenanes. Starting from a molecular shuttle[28] – a rotaxane that has two identical sites for the macrocycle – the group of Fraser Stoddart reported a bistable rotaxane in 1994.[29] Switching can be carried out both chemically and electrochemically, utilizing a π–π donor/acceptor recognition motif. At equilibrium, the cyclophane macrocycle preferentially encircles the benzidine unit (orange) with a ratio of 84:16 due to the stronger π-donor properties of this recognition site. However, the macrocycle can be shuttled to the biphenol unit by oxidation (top) or protonation (bottom) of the benzidine which leads to the reduction of its binding affinity. Once it is again reduced or deprotonated, the benzidine station is again the better π-donor in comparison to the biphenol and consequently the macrocycle translates back to the benzidine station.

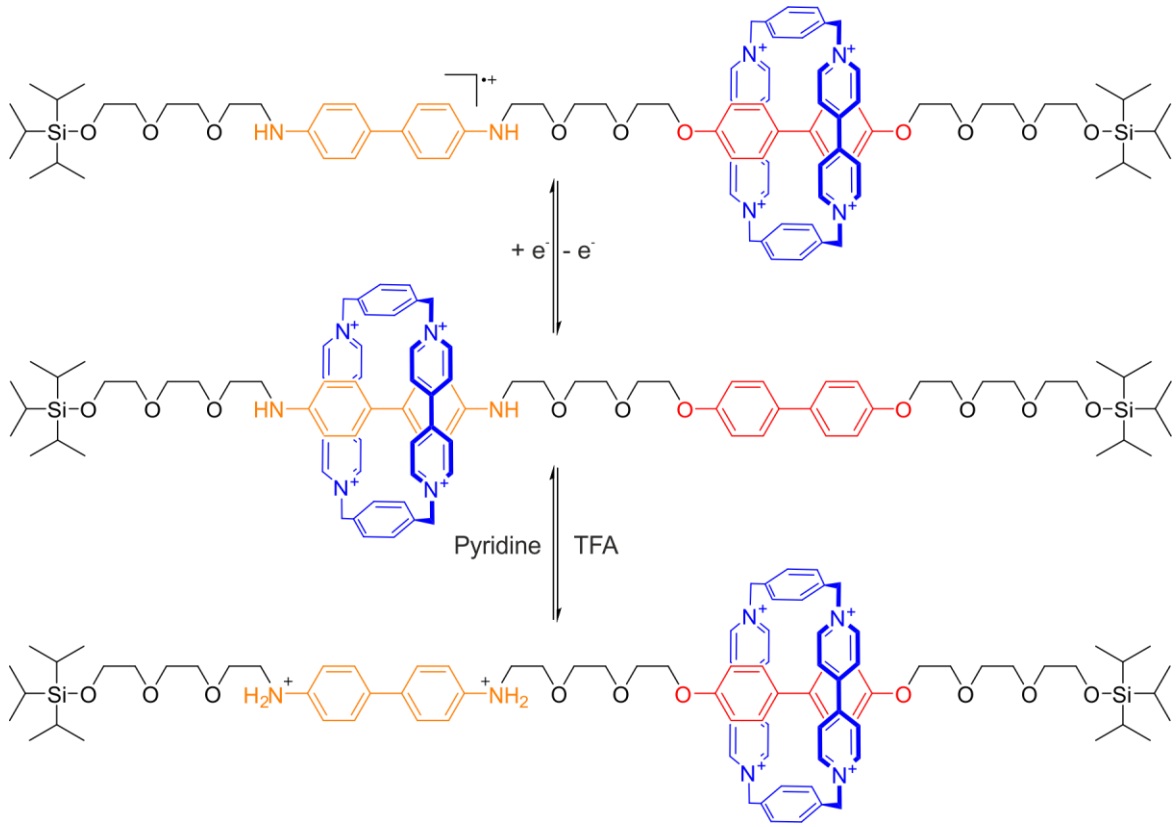

Figure 7. A bistable [2]rotaxane (middle), which can be switched through an electrochemical stimulus (top) or an acid / base equillibrium (bottom).[29]

Leigh, Zerbetto and coworkers reported in 2003 a rotaxane with a benzylic amide-macrocycle (smaller cavity than the Hunte/Vögtle macrocycle) that can be switched by light irradiation into one state and with heat back to the initial state.[30] The switching process is initiated by a photoinduced isomerization of the double-bond that is incorporated in the fumaramide/maleamide station. The trans-olefin bisamide acts as an excellent template for the formation of amide macrocycle-based rotaxanes, because the amide carbonyl groups of the thread are held in position so that they fit the hydrogen-bond-donating sites of the forming macrocycle. Irradiation at 254 nm produces the corresponding *cis*-maleimide and the potential intercomponent hydrogen-bonds are reduced from four to two. Since succinamide is incorporated into the axle as a second binding site, the macrocycle translates approximately 1.5 nm relative to the axle. The succinamide can also form four hydrogen-bonds with the macrocycle. The – compared to fumaramide – relatively small binding strength is due to a competitive intramolecular hyrdogen-bond which results in a $\Delta\Delta G$ of 15.1 kJ·mol^{-1} of the two stations in the ground state and a $\Delta\Delta G$ of -12.5 kJ·mol^{-1} in the excited state. Heating drives the rotaxane back to the initial state. All of the mentioned features lead to a photo- and thermally responsive shuttle where the macrocycle translates between two stations with remarkable positional integrity caused by matched and mismatched hydrogen-bonding motifs.

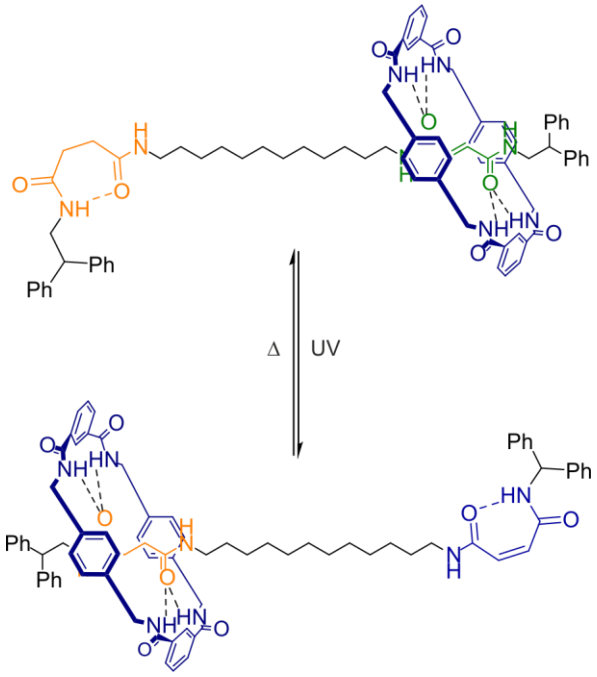

Figure 8. Bistable [2]rotaxane of Zerbetto and co-workers that is switchable by light irradiation.[30]

A station that is very well suited for the formation of a switchable rotaxane with tetralactam macrocycles is the squaraine unit, as the switching can be detected by simple spectroscopic methods and even by the naked eye.

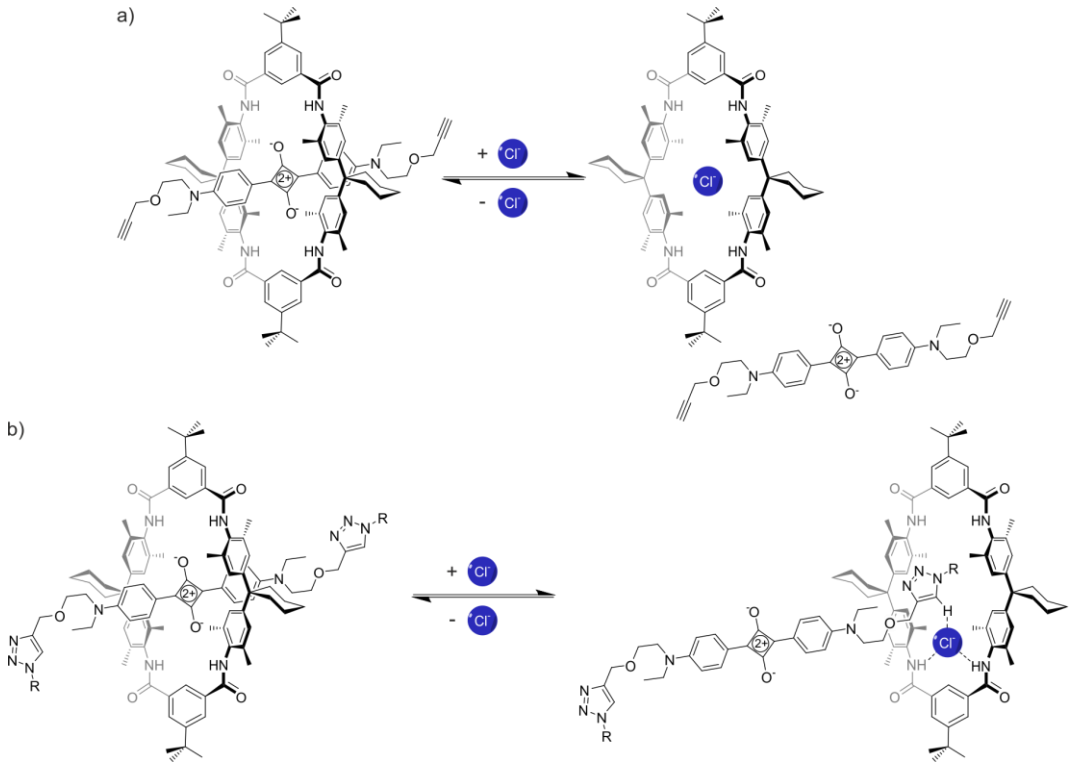

Figure 9. Displacement of the squaraine-unit from a tetralactam macrocycle and the switching of the corresponding rotaxane.

The deep red fluorescence of squaraine is shielded when it binds to the cavity of the macrocycle. Furthermore, the absorption of the squaraine molecule undergoes a change in wavelength by about 10 nm, which can be recognized by a color change of the solution. Bradley Smith and coworkers showed that when the squaraine is in a pseudorotaxane and exposed to chloride ions, it is displaced from the macrocycle so that the initial fluorescence is detectable again (Figure 9).[31] If the squaraine station is part of a rotaxane with a second macrocycle binding site such as a triazole, the macrocycle moves to the triazole upon chloride-addition and the fluorescence – as in the free station – can be detected again (Figure 9b). In this case, the chloride-ion together with the triazole binds stronger to the amides of the tetralactam macrocycle than the squaraine unit. This detection mechanism could be demonstrated both in rotaxanes immobilized on silica plates and in solution.[32]

Analogous to squaraine, a rotaxane can also be set up as a molecular switch with one diketopiperazine and two triazole stations. Here, the binding characteristics are similar to a squaraine rotaxane and can be analogously modified by the addition of chloride. The macrocycle is shifted from the diketopiperazine to the triazole(s) by the binding of chloride to the amide protons of the macrocycle (Figure 10).[33]

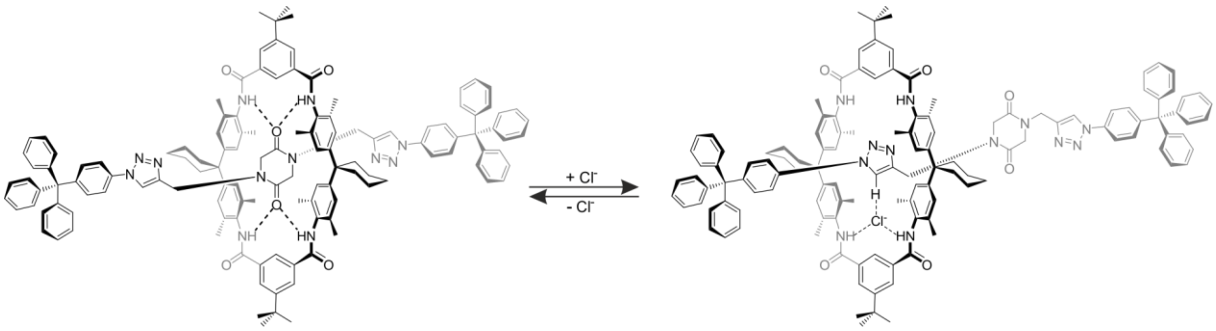

Figure 10. Switching of a three-station diketopiperazine [2]rotaxane.[33]

These rather simple examples of switchable MIMs that admittedly exhibit relative wheel-translocation but apart from that do not deliver any function or a net amount of work. Therefore, more complexity concerning structure, behavior, and function is needed. One recent molecular machine, that is based on a rotaxane, mimics the biogenic non-ribosomal peptide synthesis.[34] Here, the macrocycle is covalently linked to a short peptide chain the first residue of which is a cysteine (trityl-group protected) and tracks along an axle functionalized with three or four amino acids. The macrocycle could randomly shuttle back and forth between the stoppered end of the axle and the site of the first corresponding amino acid group on the thread. Following deprotection, the thiolate group of the cysteine residue undergoes transacylation with the first amino-acid blocking group, removing it from the axle. A subsequent reaction between the terminal amine of the peptide chain on the macrocycle extends the peptide chain and regenerates

the thiolate group. This process is repeated until the final blocking amino acid is transferred to the growing peptide chain and the macrocycle dissociated from the axle. Finally, the complete oligopeptide is cleaved from the macrocycle and the remaining protecting groups are removed.

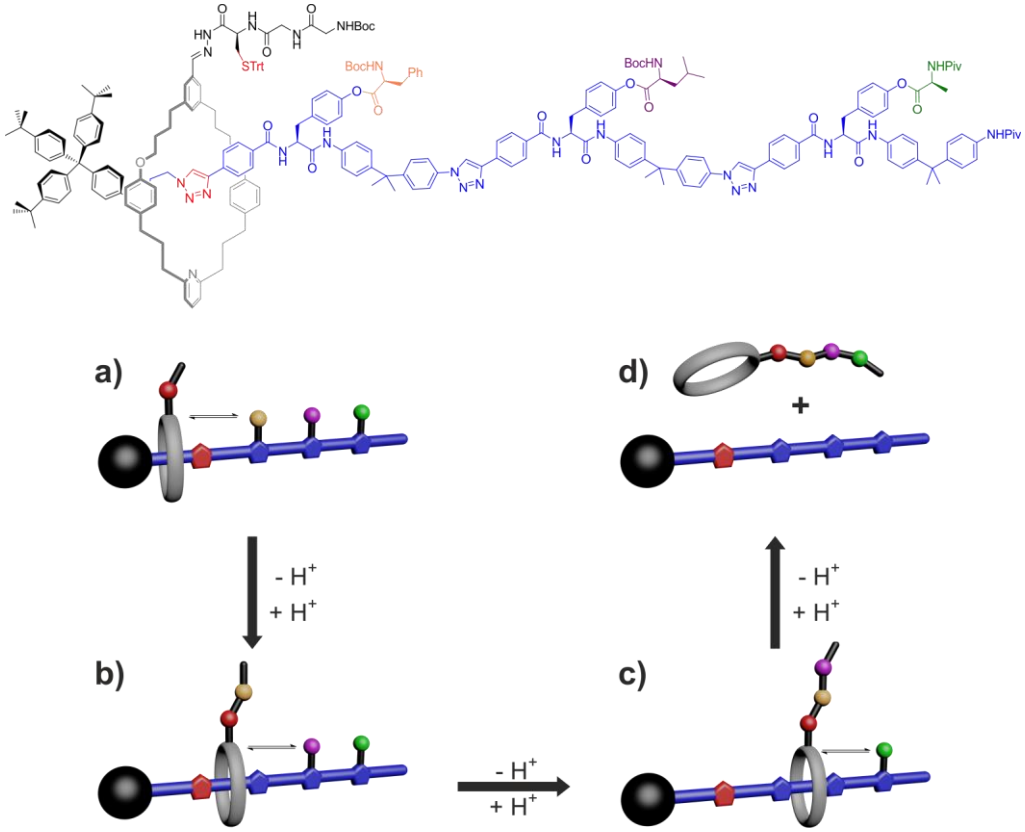

Figure 11. [2]Rotaxane-based synthetic ribosome analogue. It is in fact an artificial small-molecule machine that travels along a molecular strand, picking up amino acids that block its path, to synthesize a peptide in a sequence-specific manner.[34a]

The ribosome mimic is already very impressive as the macrocycle can move along the axle in a quasi-directional fashion. However, it is not working against the thermodynamic minimum and molecular machines should be able to drive multiple chemical processes uphill and away from their ‘‘inherent’’ equilibria, just as motor molecules do in biological systems.[5] A topologically interlocked molecule has recently been shown to act as a rudimentary molecular pump mimicking the functionality of a transmembrane ion-pump in biological systems and therefore working against a concentration gradient. The system comprises a molecular axle that can store up to two macrocycles. When the positively charged viologen-units on both the macrocycle and the axle are reduced to their radical form, the repulsion between the macrocycle and the axle is decreased. The macrocycle is then able to thread onto the partially reduced viologen station on the axle. Following threading, the viologen units on the macrocycle and axle are re-oxidized using $NOPF_6$. The electrostatic repulsion between the macrocycle and the positively charged end of the axle is now sufficient to overcome the steric barrier presented by the isopropylphenyl group such that the macrocycle becomes trapped on the stoppered alkyl chain.

Repetition of the cycle of reduction, oxidation and reduction allows a second macrocycle to be 'pumped' onto the alkyl chain in an overall energetically uphill process.[35]

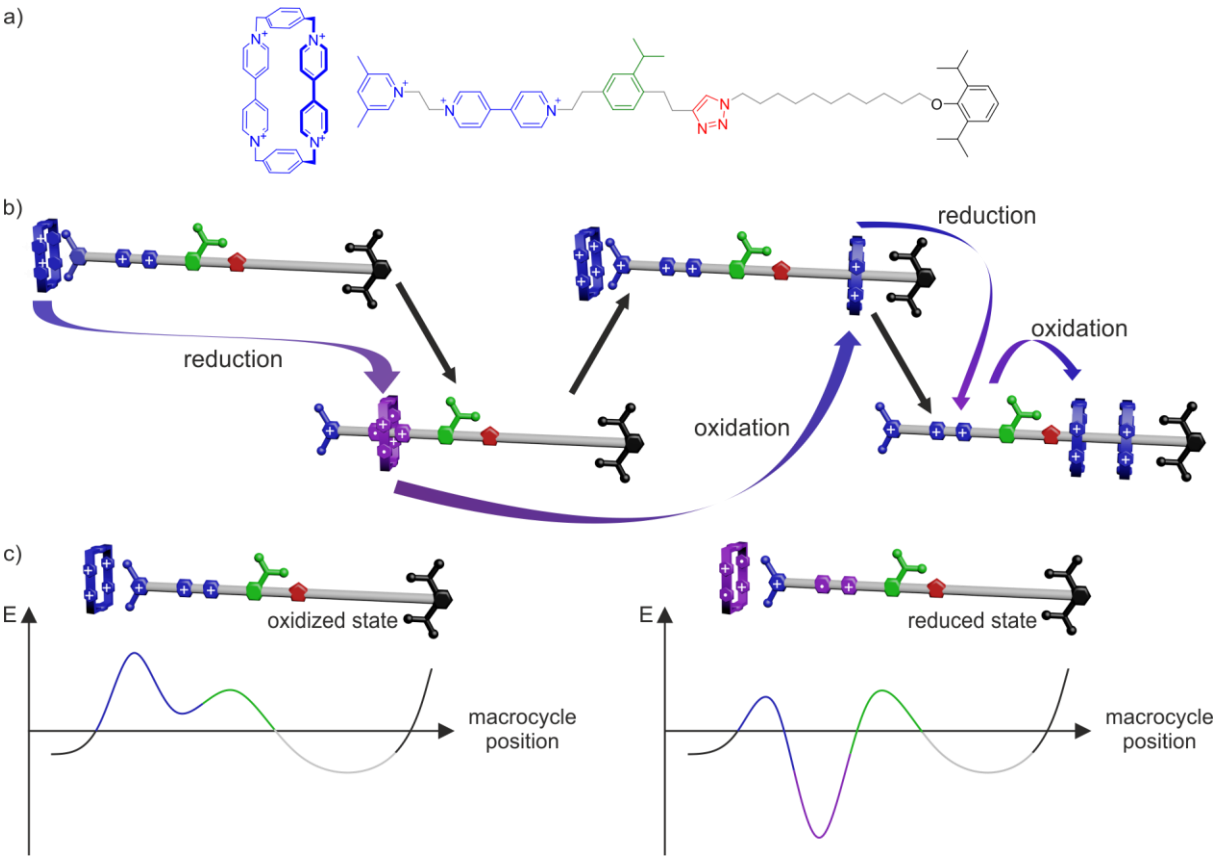

Figure 12. An artificial molecular pump driven by external redox-switching conditions. a) Molecular structures of the macrocycle and the axle, b) Behavior of the two components upon reduction and oxidation in two cycles, and c) energy profiles for oxidized and the reduced state.[36]

Credi *et al.* reported a synthetically easy example that resembles one key attribute of biological molecular machines which is not present in the previous example: An autonomous nanomechanical operation in repetitive cycles that dissipate energy supplied by a chemical or electromagnetic potential.[37] Two components are involved in the system that is depicted in Figure 13: A 2,3-dinaphtho[24]crown-8 ether macrocycle (purple) and a molecular axle containing a photoisomerisable azobenzene moiety (E green, Z red), a cationic ammonium recognition site (blue) and a cyclopentyl terminus (grey). Although the macrocycle axle binding equilibria for both the *E* and the *Z* axle isomers lay towards the complex, binding to the *E*-isomer is more favorable. They also showed that the barrier of macrocycle threading over the *E*-azobenzene moiety is lower than of the cyclopentyl group, while the macrocycle preferably unthreads over the cyclopentyl group in comparison to the *Z*-azobenzene moiety. Additionally, the *E*-complex was more sensitive to *E/Z*-photoisomerisation than the free *E*-axle and the lifetime of the *Z*-complex was long enough that dethreading preferentially occurred over the cyclopentyl unit.

As a consequence of the differing energetic barriers to threading/unthreading and the differing rates of isomer interconversion, threading and dethreading proceed with a directional bias under constant photoirradiation.

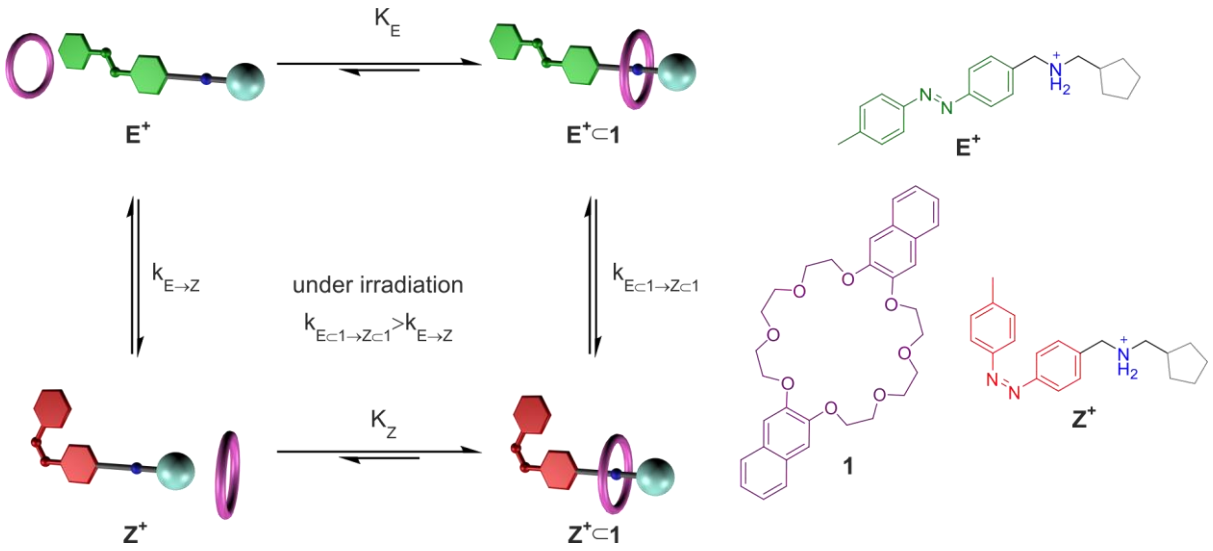

Figure 13. Light-driven autonomous cycle of unidirectional supramolecular assembly/disassembly.[37]

Although the examples mentioned show a relative motion of the macrocycle on the axle, these are far away from performing work as directionality is lost when summed over the random orientations of the freely moving assemblies in solution. The following chapter successively describes techniques to overcome this problem by the incorporation of the described (or analogous) switches into monolayers or even multilayers. This should potentially mimic the oriented embedment of biological molecular machines into membranes.

3.4. Organic Thin-Films

3.4.1. Self-Assembled Monolayers (SAMs)

Since the first systematic investigation of self-assembled monolayers (SAMs) started about 25 years ago,[38] they have developed into an important section of research in the field of nanotechnology. The ease of preparation, the huge diversity, and the enormous potential of these organic thin films continue to drive a number of new developments. These organic materials can noticeably modify the interfacial properties and are able to increase the stability of the coated metals or electrically insulate them. They can be referred to as arrays of amphiphilic molecules that adsorb on certain metal surfaces from solution or gas phase by chemisorption in which intermolecular forces play a crucial role. Each of the molecules has a terminal (functional) group, a backbone (spacer unit) and a head group affinitive to metal surfaces which can be both covalently and ionically bound to the surface (Figure 14). The head group guides the self-assembly process on each type of metal substrate, linking the backbone to the metal with a strong bond. The molecules can – due to the reduction in free energy between the surface and its surrounding medium – spontaneously adsorb on the metal.

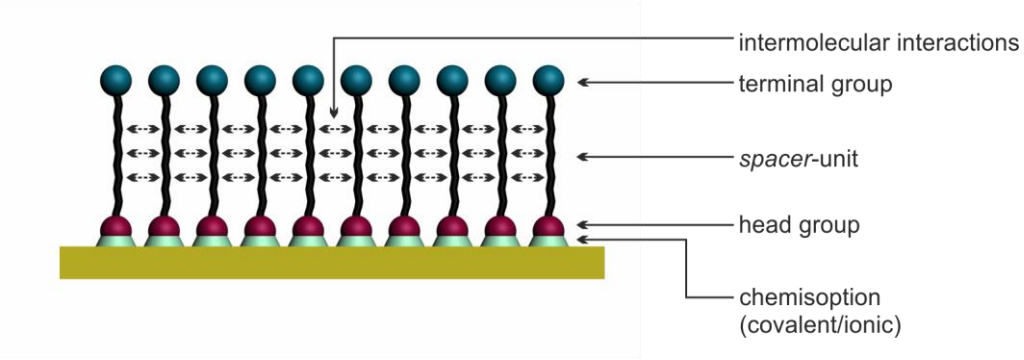

Figure 14. General scheme of a chemisorbed self-assembled monolayer in a standing up configuration.

The interactions between the molecules in the backbone involve for example van der Waals or hydrophobic forces, ensure an efficient packing of the monolayer, and stabilize the structures with increasing chain length. However, the effects of SAM-molecules on the properties of the surface depend only on the end group which can also be used to anchor different molecules, biomolecules, supramolecules, or nanostructures by weak interactions or covalent bonds (see chapter 3.5.2).[39] The fact that it is possible to prepare SAMs with different terminal groups (an important issue for many applications) make them the most important type of organic monolayer. Additionally, SAMs can be formed not only on planar surfaces, but also on objects of all sizes and with a variety of shapes like nanoparticles or nanotubes.

They can also be regarded as the interface between ‘‘two worlds’’: metals, semiconductors, and inorganic compounds, on one hand, and simple organic compounds, polymers, complex supra- and biomolecules, and even cells on the other.[39] They thus represent an easy way to link materials with totally different physical and chemical properties. Moreover, the self-assembly process can involve different levels of construction, in a similar way to protein formation.[40] This is the reason why SAMs are so important in the ‘‘bottom-up’’ methods that are widely used in nanotechnology involving very different areas of expertise. Among applications of SAMs in nanotechnology are their use for stabilization and functionalization of nano-sized objects (nanoparticles, nanorods and nanowires),[41] which in turn also have plenty of applications. Other important uses of SAMs are in the field of material protection as ultrathin layers for corrosion prevention.[42] In the area of device fabrication, SAMs are used as building blocks in biosensors,[43] actuators, and molecular motors.[44]

The most popular SAMs are those of thiols and dithiols (or disulfides and sulfides) on different oxide-free metals like gold due to their promising and current applications in several fields of nanotechnology. In this particular case, SAMs are used in the field of device fabrication as inks or resists in lithography for ‘‘writing’’ molecules and biomolecules on gold,[41a, 45] in molecular electronics (as passive or active parts in transistors and switches),[46] in sensors and biosensors (to immobilize different types of biomolecules, like DNA, enzymes, phospholipid membranes, bilayers and hybrid membranes, either on planar or irregular surfaces, or in nanoparticles and nanowires),[47] etc. In the synthesis of gold nanoparticles, thiol SAMs play an important role for stabilization of those nanostructures against aggregation[48] and to control the cluster size by tuning the hydrocarbon chain length.[49] Furthermore, thiol and dithiol SAMs are used in the field of biomedicine as linkers or protective groups for biomolecule carriers (e.g., for drug delivery purposes),[50] and also to functionalize the surface of medical devices such as gold stents.[51] Other applications include their use as chemical templates for crystallization of salts.[52]

The mechanism of thiol-monolayer formation on gold is generally divided into four different phases (Figure 15). First, the disordered adsorption of the metal-affine head group takes place (a). The intermediate phase is comprised of flat on the surface lying, disordered molecules, which already form the first bonds to the substrate (b). Subsequently, isolated islanding by the erection of the molecules is described (c), which then results into an ordered, densely packed monolayer on the surface (d). Here, the already mentioned interactions between the backbones of the molecules, which have a strong influence to the resulting order of the monolayer, play a crucial role.

The energy related to each part of the molecule has different orders of magnitude: in the area of 200 kJ mol^{-1} for the thiolate bond; around 4-8 kJ mol^{-1} for the van der Waals interactions per methylene between the arylic backbones; and only small energies for the interactions between

the terminal groups.[53] However, all parts contribute to the structure as well as the properties of the monolayer. Even though SAMs have been extensively studied with a huge variety of analyzation methods, many aspects of monolayers remain controversial.[54] Indeed, the knowledge of the thiol-Au bond is incomplete at best until today. There are two models on how this moiety can occur in the monolayer. Against the classical picture of a static, unreconstructed Au(111) surface with molecules adsorbed at specific sights building up thiolate bonds[55] holds new experimental and theoretical data which suggest that the interactions between the monolayer molecules and the surface molecules are rather dynamical and that this induces a strong reconstruction of the surface which involves the formation of thiolate-adatom moieties.[56] For clarity, this work concentrates on the classical picture which is shown in Figure 16. The central bonding habit with a maximum coverage of thiols in this picture is based on an overlayer with a 5 Å x 5 Å lattice where the sulfur atoms (red circles) are positioned in the 3-fold hollows of the gold lattice (yellow circles) with an atom radius of 2.88 Å.[57]

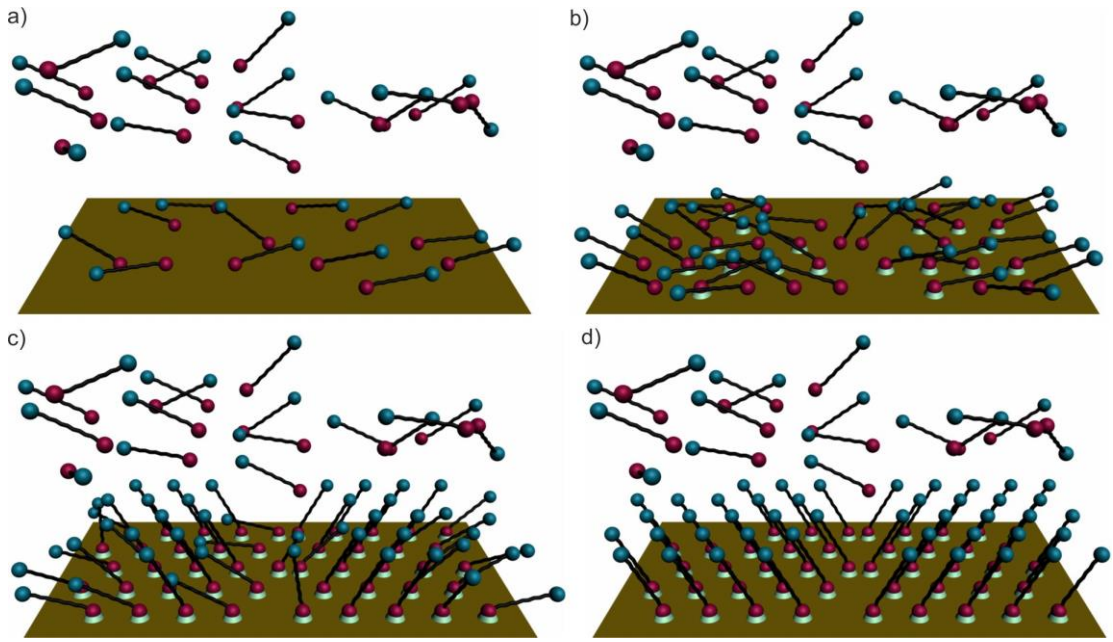

Figure 15. Schematic illustration of the self-assembly processs of thiols on Au(111). a) First surface-adsorption of thiol molecules that adopt the highly mobile lattice-liquid phase at very low concentrations; b) Intermediate phase with flat on the surface lying, disordered molecules; c) Isolated islanding and d) an ordered, densely packed monolayer is formed.

The SAMs formed by *n*-alkanethiols are described as thiolate overlayers (chemisorbed structures formed by the activation of the S-H bond at the gold surface). Despite the present order of the molecules in a hexagonal packing, isolated errors emerge in the molecular composite thiol-monolayers and the 'perfect' assembled monolayer depicted here is far from reality which somehow limits their applicability. The orientation or the order of the SAM is highly influenced

by the choice of the molecule backbone. While alkyl groups exhibit a tilt angle of around 30°,[57] aryl groups have an angle of nearly 0° to the surface normal.[58]

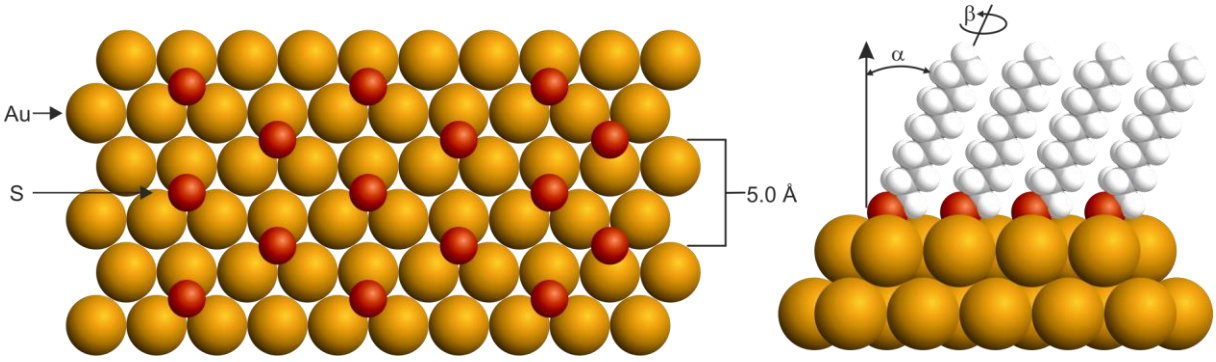

Figure 16. Schematic illustration of the arrangement of decanethiolates on a Au(111) lattice when maximum coverage of the thiolates is present. Left: Structural model of the commensurate adlayer formed by thiols on the gold lattice where the thiols sit in the 3-fold spaces between the gold-atoms. Right: Cross-section of the SAM formed from decanethiol with α as the tilting angle and β as rotation angle.[41a]

For SAM formation on hydroxylated surfaces, well-studied alkoxysilanes are taken.[59] Besides silicon dioxide[60] and glass,[61] these monolayer precursors can functionalize aluminum oxide,[62] titanium oxide,[63] and mica[64] as well. The formation mechanism of these SAMs significantly differs to that of thiol-SAMs. Not only a connection between the molecules and the surface takes place; an intermolecular connection forms which leads to a polymerization of the silanes. This causes to an adsorption of not only individual molecules but also of whole domains that are preorganized and coalesce with increasing surface coverage. The molecular distance is determined by the Si-O-Si bond to be 4.4 Å which then also influences the tilting angle of the monolayer to a smaller value of around 20° to the surface normal.[53]

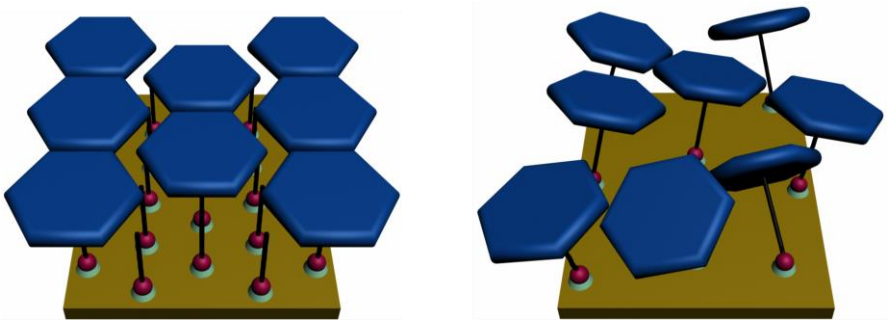

Figure 17. Schematic illustration of a self-assembled monolayer with bulky terminal groups.

As the SAM serves as a template for many different chemical processes, it is necessary to functionalize the head group. This can for example be done with a moiety that enables a chemical reaction, or with a functionality that allows to use coordination chemistry like pyridine.[65]

Furthermore, bulky terminal groups like terpyridine can be used. However, these groups may hamper intermolecular interactions between the molecular backbones due to their steric demand. In this case, it happens that the molecules randomly distribute on the surface (Figure 17, right) and the end group is only partially or not at all available for functionalization (see chapter 3.5.3).[66] In order to solve this restriction, the functionalized SAM molecules can be deposited together with non-functionalized SAM molecules in a specific ratio on the surface. Thus, the order can be established with the aid of a mixed SAM and it can then be used as a template for a subsequent (metal-) deposition (Figure 13, left).

3.4.2. Chemical Modification of Self-Assembled Monolayers

Besides the adsorption of pre-functionalized molecules onto surfaces, the subsequent modification of monolayers represents an excellent possibility to prepare a large variety of differently functionalized substrates.

Table 1. Overview of selected modification concepts to obtain functional self-assembled monolayers.[67]

reaction type	substrate	reaction partner	product
radical bromination[68]	--CH_3	Br_2/CCl_4	-CH_2Br/-$CHBr_2$
nucleophilic substitution[69]	--Br	NaN_3	--N_3
		KSCN	--SCN
		Na_2S	--S--
	--Br	1. Potassium phthalimide	--NH_2
		2. CH_3NH_2	
reduction[70]	--CN	$LiAlH_4/NaAl(OEtOMe)_2H_2$	--NH_2
nucleophilic addition[71]	--NH_2	RNCS	--NH_2CSNH_2R
Michael addition[72]	--maleimide	RSH	--maleimide-SR
thiol-ene reaction[73]	--SH	CH_2=CH-R	--S-CH_2-CH_2-R
acylation[74]	Active ester	NH_2R,	--CONHR,
	(CO_2R)	NHR^1R^2	--$CONHR^1R^2$
condensation[75]	--OH	RCO_2H	--O_2CR
(imine formation)[76]	--NH_2	OCHR	=NR
(oxime formation)[77]	--COR^1	H_2NOR^2	--CR^1NOR^2
Diels-Alder cycloaddition[78]	quinone	cyclopentadiene	cyclohexene
1,3-dipolar cycloaddition[79]	--N_3	HCCR, RCCR	triazole

For the functionalization of SAMs, certain criteria must be fulfilled: (I) The reaction should work in high yield under mild reaction conditions. (II) The end group should have certain compatible reaction partners. (III) No byproducts should be formed during the reaction. Additionally, it is

advantageous – but not necessary – to have a reaction that does not require a catalytic activation. Table 1 summarizes a selection of reactions that have been established in recent years. Out of this selection, the nucleophilic substitution and addition, the Michael addition, the thiol-ene reaction as well as the catalyst-free 1,3-dipolar cycloaddition ('click'-reaction) are most frequently used and most important as they can for example be applied to immobilize biomolecules onto the surface.[80]

As seen in **Table 1**, the amino moiety offers a wide range of possibilities for functionalization. In 2010, Dietrich *et al.*[71a] for example investigated the accessibility for functionalization of two newly synthesized amino-terphenyl (**ATPn**) monolayers that contain alkyl linkers with different lengths. The reaction they tested was a nucleophilic addition of an amine with an isothiocyanate derivative which was shown to be successful for aliphatic amines in an earlier study.[71b] The reaction leading to fluorine-containing thiourea **ATPn-F** products is shown in Scheme 1.

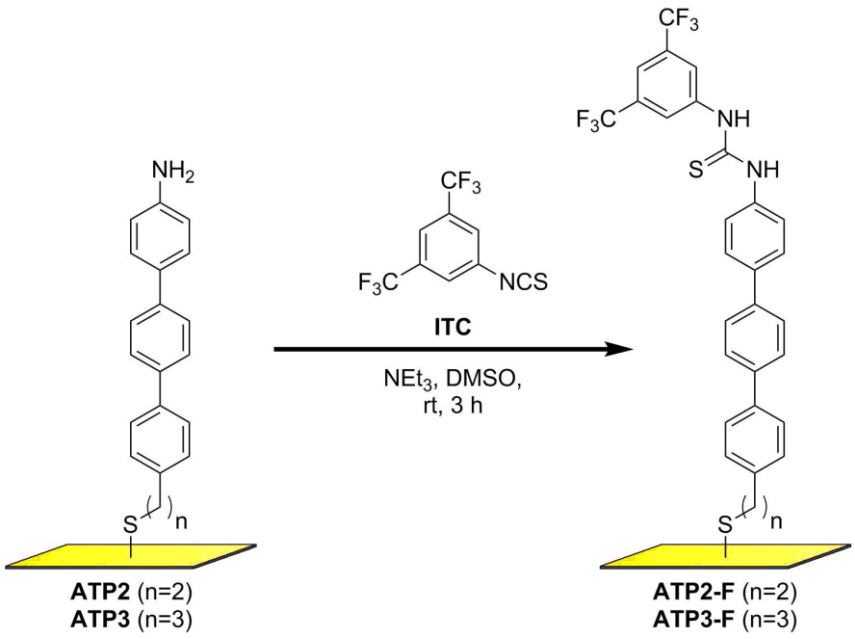

Scheme 1. Derivatization of ATPn SAMs with 3,5-Bis(trifluoromethyl)phenyl Isothiocyanate (ITC).[71a]

As the SAMs used combine the advantages of saturated and aromatic thiols, their order is a result of the strong interaction between the rigid aromatic parts and the flexibility of the alkyl chains that permits the aromatic moieties to adopt ideal packing. Even hydrogen bonds, that are known to cause significant disorder in aliphatic thiolate monolayers, are not able to break this tight packing.[81] Furthermore, the aromatic amino-function should not be protonated by the thiol as it has a significantly lower pKa-value. For the reaction, it has to be also considered that the amine could react with water which is minimized by the use of anhydrous conditions. The reaction product was then studied with XPS and NEXAFS.

The most important SAM modification for this work is the 1,3-dipolar cycloaddition – in particular the copper-catalyzed azide-alkyne Huisgen cycloaddition (CuAAC) as the premier example of a click reaction that has been reported first in 2002.[82] Its high regioselectivity towards the 1,4-regioisomer as well as the fact that it usually works with quantitative yields under mild conditions make it very attractive for the deposition of defined (bio-)molecular architectures. The numerous examples in literature confirm that a wide variety of reaction conditions can be successfully employed, too. Collman *et al.* reported a possibility to functionalize mixed azide self-assembled monolayers that are prepared by mixing azidoundecanethiol amd decanethiol as diluent with an alkyne-modified ferrocene in solution as shown in Scheme 2.

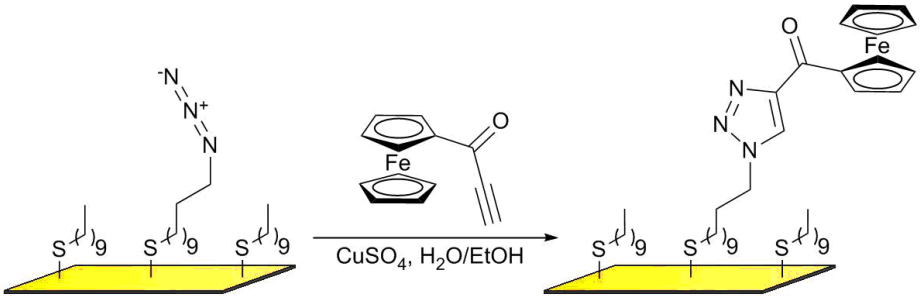

Scheme 2. SAM modification by 'click'-chemistry according to a procedure of Collman *et al.*[79a]

For the deposition of biomolecules however, the described reaction has to be altered as the Cu-salts used are potentially cytotoxic. This has been achieved by the implementation of ring-strained cyclooctynes and dibenzocyclooctynes in strain-promoted azide-alkyne cycloadditions.[83] In combination with a high retention of activity, this yielded a rapid reaction under mild conditions. Although this modification offers a wide range of possibilities for biological applications, the present work focuses on the Cu-catalyzed version described above.

3.4.3. Microcontact Printing (µCP)

In the course of developing bottom-up methods for the fabrication of materials at the micro- and nanometer scale, the most efficient and applied method is the self-assembly of molecules and (nano)particles. For example, self-assembly applied to a solid surface leads to the creation of structures with a vertical dimension of nanometers called self-assembled monolayers as seen in chapter 3.4.1. However, the possibility of area and volume pattern fabrication by this approach is very limited. This is why soft-lithography and microcontact printing (µCP) in particular was introduced. The combination of the self-assembly of SAMs with the capabilities of top-down techniques to pattern large surface-areas opens up the way to cheap and easily accessible nanofabricates.[84]

The original idea behind this method was to find a fast and easy method to replicate patterns generated by photolithography: The surface of a silicon wafer is usually coated with a thin and uniform layer of a UV-light-sensitive polymer (photoresist) which is then exposed to light through a metal photomask. As seen in Figure 18, the light passes through the mask only at the non-metallized areas and generates an area-selective degradation of the polymer according to the designed pattern on the mask. The remaining polymer is then used as a resist in the subsequent etching step in order to get a patterned silicon surface. The novelty of µCP was the use of an elastomer – usually a poly(dimethylsiloxane) (PDMS), casted from the above described silicon master (Figure 18) – as a tool to generate a patterned SAM on a solid surface. In the stamp-preparation step, the liquid vinyl-terminated precursor and the curing agent, which consists of a short hydrosilane crosslinker containing a platinum complex as a catalyst, are mixed and poured onto the patterned template.[85]

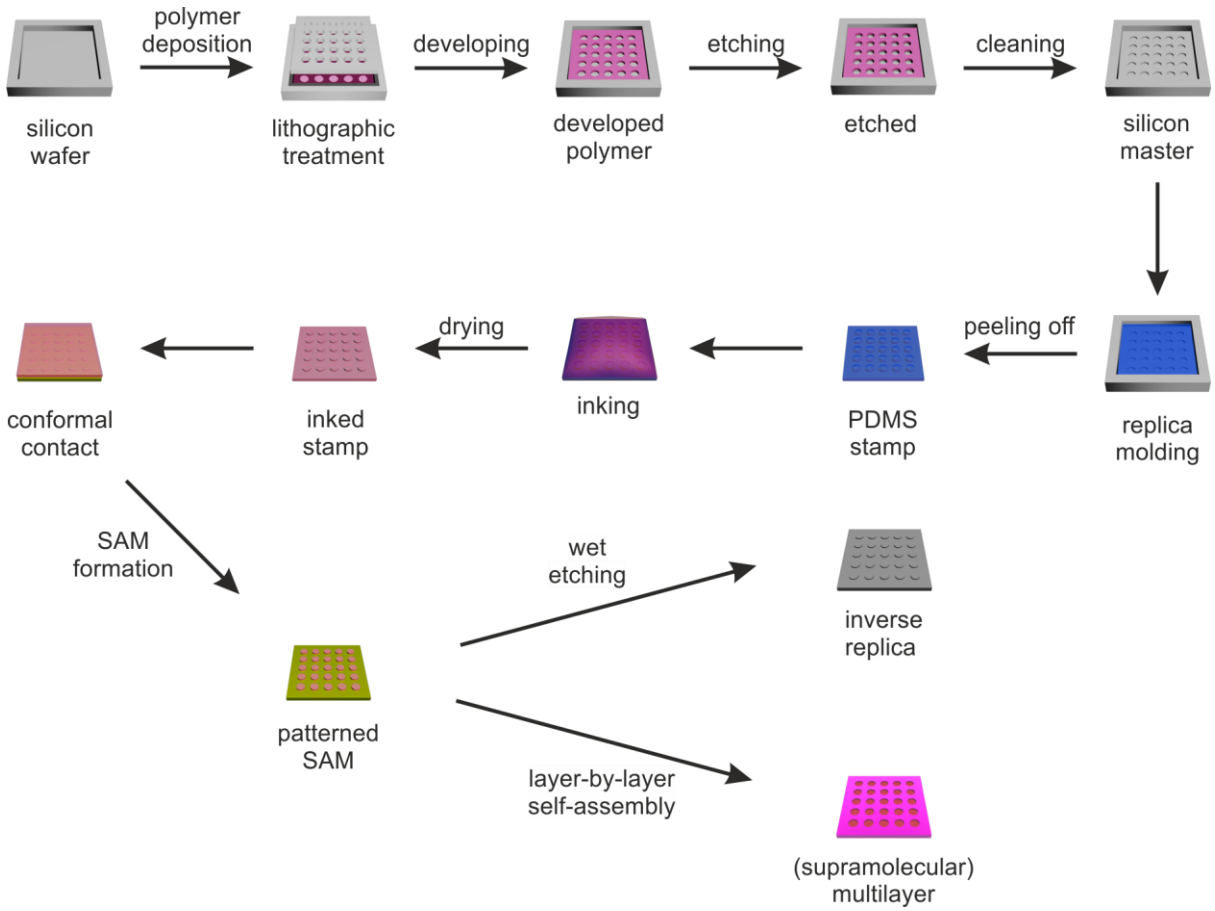

Figure 18. Schematic representation of the photolithographic production of a silicon master and the successive transfer of the pattern to a PDMS stamp that is used for a patterned SAM formation. Subsequent uses are the production of an inverse replica by wet etching and also the layer-by-layer self-assembly of supra- or biomolecular architectures.[86]

The PDMS is cured at higher temperatures that are usually around 60 °C, which forms a solid but elastomeric polymer. After peeling it off, the stamp is cut to proper size and inked with a

solution of the monolayer forming molecule. Wet inking is achieved either by immersion of the stamp in the ink solution or by placing a few droplets of the solution on the patterned side of the stamp. Hydrophobic long-chain molecules not only stay on top of the stamp surface but they also diffuse into the bulk of the stamp material. After inking, the solvent (ethanol) is evaporated in a stream of nitrogen and the stamp surface is dried. By bringing the inked stamp in contact with the gold surface, the molecule is transferred to the surface. Due to the patterned structure of the stamp, only the jutted areas are able to contact the surface, and the SAM-molecule is selectively transferred according to the pattern of the template. The order and quality of the SAMs of long-chain thiols formed by printing are indistinguishable from those formed in solution when a proper concentration of a few mM is used.[86]

Apart from its use to pattern SAMs as etch resist on different substrates, microcontact printing can also be used for chemical synthesis on gold and silicon as well as the deposition of supra- or biomolecular assemblies.[70a, 87] In the field of the fabrication of micro-patterned surfaces, the scientists at the University of Twente are world leading, and conducted and devised countless studies and applications. In 2006, they employed a Huisgen 1,3-dipolar cycloaddition induced without any catalyst by µCP of acetylenes onto azido-terminated SAMs on silicon oxide substrates.[88] Azido-terminated SAMs on silicon oxide were prepared by the substitution of a bromo-terminated monolayer with NaN_3 (Figure 19).[69a]

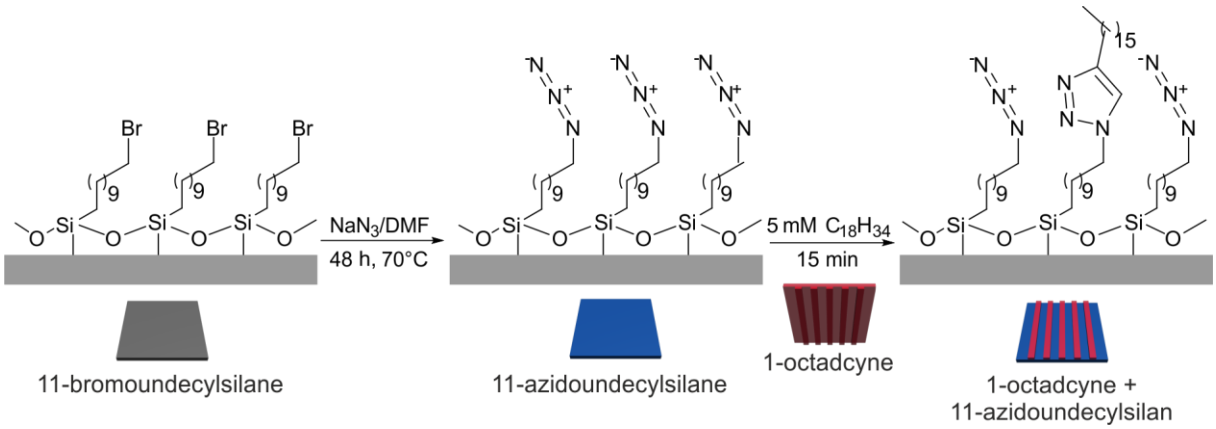

Figure 19. Click chemistry by µCP. (Left) Bromo-terminated SAM on a Si/ SiO_2 substrate, (middle) azido-terminated SAM and (right) triazole SAM after µCP of 1-octadecyne onto azido-terminated.[88]

Subsequently, the PDMS stamp is inked with a solution of 1-octadecyne in ethanol for 1 min, then dried under a nitrogen stream, and brought into contact with the substrate SAM for 15 min with a load of 35 g in order to have good contact and constant load during the entire printing time. After rinsing with ethanol, the deposition was confirmed by AFM (see chapter 3.5.5) and XPS (see chapter 3.5.2).

In 2012, Ravoo and coworkers prepared micropatterned azide/benzaldoxime-surfaces by microcontact printing.[83a] Subsequently, the areas with an azide terminal-group are modified by reaction with a cyclooctyne-conjugate using strain-promoted azide–alkyne cycloaddition (SPAAC). The benzaldoxime areas, however, are activated by in situ oxidation to the reactive nitrile oxides and subsequent nitrile oxide cycloaddition with alkene- or alkyne-functionalized bioconjugates is then carried out (Figure 20). In addition, orthogonal double immobilization was achieved by consecutive and independent SPAAC and nitrile oxide cycloadditions. This was then analyzed by ToF-SIMS (see chapter 3.5.4), XPS, AFM, and, after deposition of fluorescing biomolecules, with fluorescence microscopy.

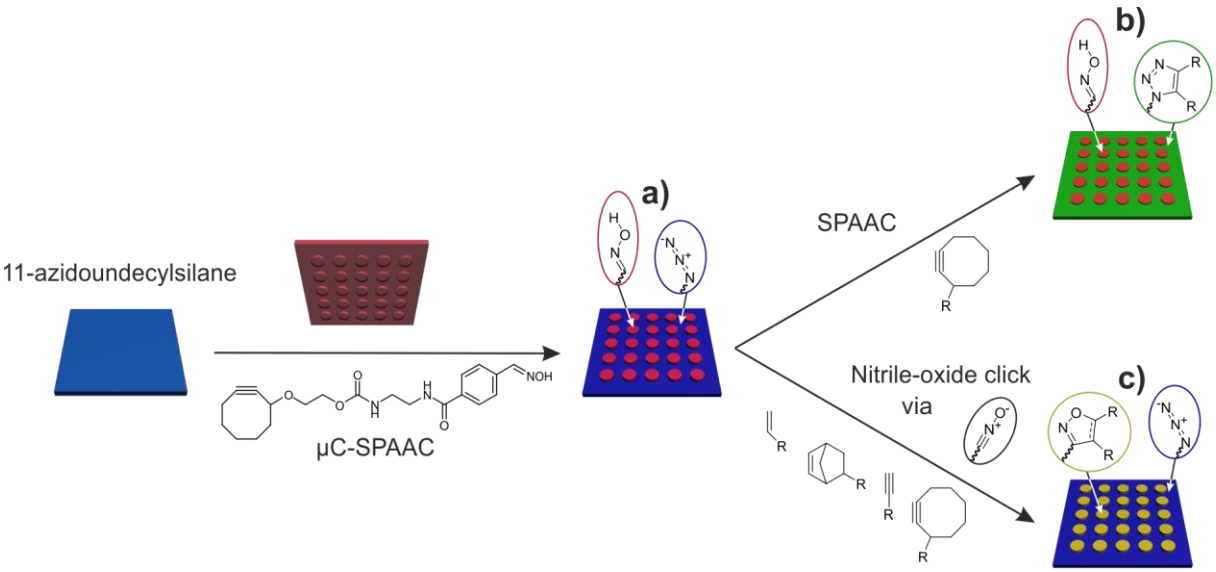

Figure 20. Immobilization of cyclooctyne oxime linker by (a) μC-SPAAC, (b) surface modifications by nitrile oxide cycloadditions, and (c) Surface modification by SPAAC.[83a]

In this work, μCP is only used as tool for the analysis of the layer-thickness of layer-by-layer self-assembled rotaxanes as it is necessary to know with which angle the rotaxanes are oriented on the templating self-assembled monolayers. The underlying method will be described in the following chapter.

3.4.4. Layer-by-Layer Assembled Metal-Organic Multilayers

Over the past few decades, layer-by-layer (LbL) assembly of thin films has been of considerable interest because of its ability to exert nanometer control over film thickness and its extensive choice of usable materials for coating interfacial and colloid substrates. Additionally, the choice of materials allows for responsive and functional thin films to be engineered for various applications, including catalysis, optics, energy, membranes, and biomedicine.[89]

In general, LbL assembly can be considered as a cyclic process in which a (charged) material is adsorbed onto a substrate or template layer, and after washing, a material with opposite properties is deposited on top of the first layer. For the implementation of layer-by-layer self-assembly different binding motifs have already been employed like metal-to-ligand binding,[90] positively- to negatively-charged (macro-)molecules,[91] hydrogen-bond binding [92] or a click-chemistry approach.[93] This generates single bilayers with thicknesses in the nanometer scale. Subsequently, the process can be repeated until a multilayer with the desired thickness is achieved. The simplicity, versatility, and nanoscale control make LbL assembly a widely used technology for coating interfacial as well as colloidal systems in a diverse range of applications. The widespread use of the technology has led to the development of different assembly techniques which include dipping (immersing),[94] spraying[95] or spinning[96] of which the first two are most important for this work. The choice of method affects both the process as well as the material properties and should therefore be well reflected. Due to its easy applicability, immersive LbL-assembly is the most widely used method and referred as standard compared to newer technologies. It is typically performed by manually immersing a substrate into a solution of the desired material, followed by washing to remove unbound material (see Figure 21).[89]

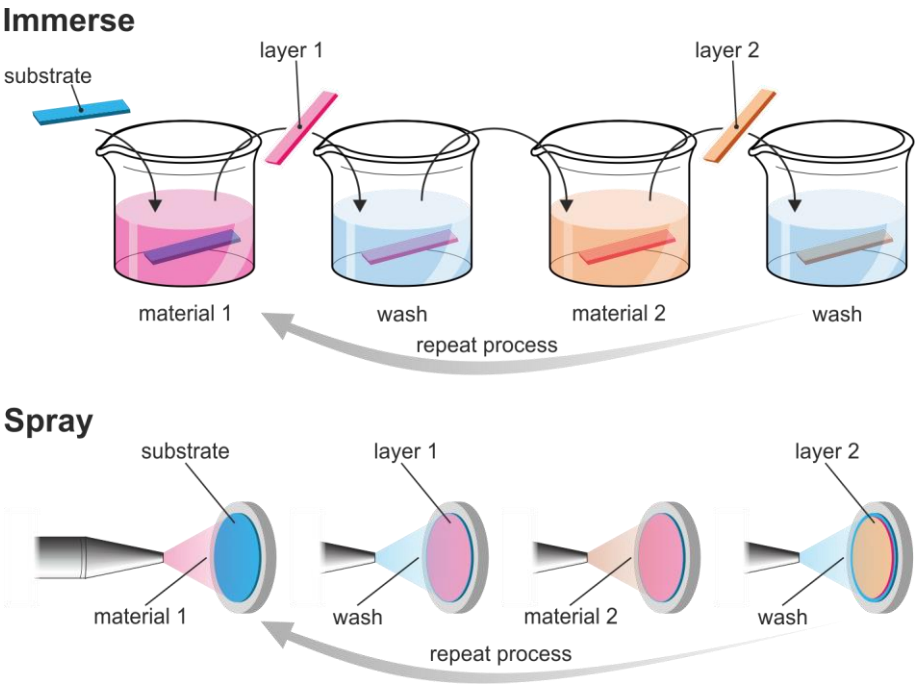

Figure 21. Schematical illustration of the technology-categories relevant for LbL assembly in this work. Adapted from J. J. Richardson, M. Björnmalm, F. Caruso, *Science* 2015, *348*, aaa2491 2491-2411 with permission from AAAS.

A second method to develop nano-assembled multilayers is the spraying technique. Here, the material is applied by aerosolizing the solution and sequential spraying it to the substrate.

Standard spray assembly is much faster than immersive assembly and can also be accelerated by using vacuum. For the systems used in this work, this could be seen as a major disadvantage because their assembly time is much longer than that of charged polymers that are usually used in this process and there is not sufficient material present for a longer exposition. The method of dipping is based on a concept by Iler *et al.* who applied oppositely charged, colloidal particles on a glass substrate.[97] Here, the formation of multilayers is based on electrostatic interactions between the individual particles. In order to form these multilayers, the affinity of the particles to their oppositely charged particle is employed as with each coating step only one layer should be deposited to the substrate. In this way, it is possible to display defined layers with discrete thicknesses. In 1997, Gero Decher succeeded in the deposition of negatively and positively charged polyelectrolytes on to a charged substrate.[94] Like in the work of Iler, the formation of the multilayer is based on complementary charges and thus to electrostatic interactions. As already mentioned, the concept can be extended to organic compounds and also other interactions apart from electrostatic ones.

An in recent years very important concept for the construction of multilayers are coordination complexes. Here, metal-organic complexes are formed that have octahedral, tetrahedral, square planar or linear coordination spheres. The multilayers are constructed of alternating layers of organic molecules and metal ions for which a SAM provides the basis (template). Figure 22 shows the basic principle for the formation of a multilayer of organic ligands and metal ions by means of LbL self-assembly using the example of sterically demanding organometallic compounds.

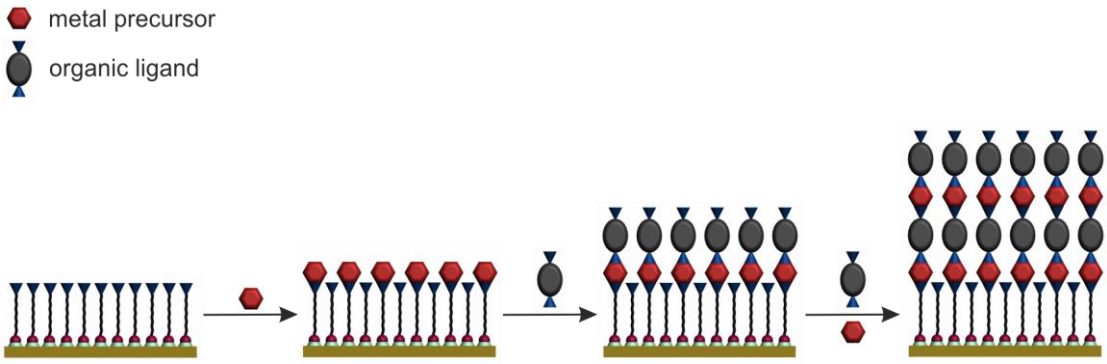

Figure 22. LbL self-assembly of a metal-organic framework on surfaces.

That this technology is in principle applicable to the immobilization of bulky molecules was shown by Christof Wöll *et al.* [98] through a stepwise growth of so-called metal-organic frameworks (MOFs) on surfaces. A SAM with a terminal carboxylate moiety acts as the template layer. Subsequent to the monolayer formation, the surface is dipped alternately into a solution of the metal-precursor Cu(II)-acetate and the organic ligand benzene-1,3,5-tricarboxylic acid

to produce a three-dimensionally connected framework which is characterized by a high order and stability.

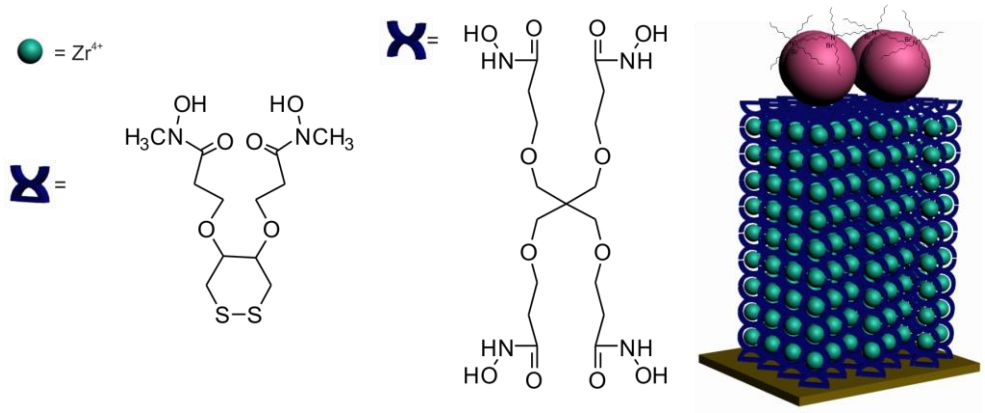

Figure 23. Metal-organic multilayer capped with TOAB gold-nanoparticles according to Rubinstein *et al.*[99]

Another example of a multilayer with metal-organic complexes represents the work of Rubinstein *et al.*[99] They showed that not only organic molecules can build multilayers on coordination complexes, but also core-shell gold nanoparticles could be integrated into a molecular multilayer as depicted in Figure 23. Nanoparticle mono- and multilayers prepared in this manner were characterized by UV-Vis spectroscopy, AFM, and cross-sectional transmission electron microscopy (TEM) showing a regular growth of NP layers.

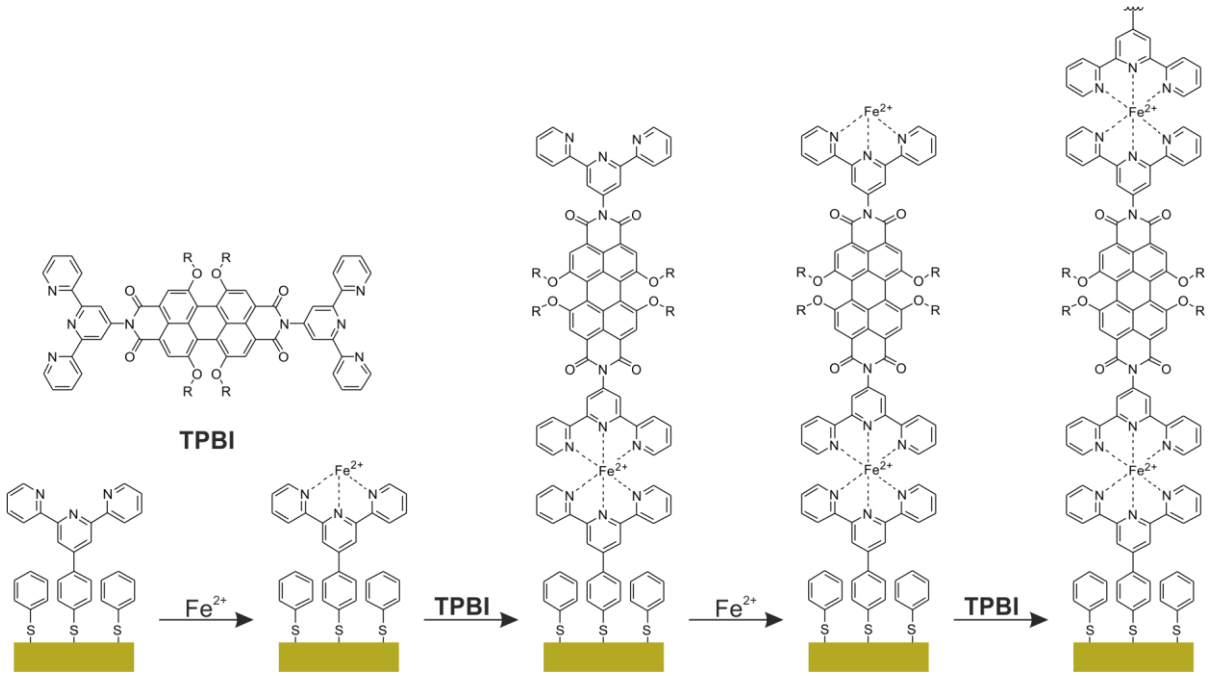

Figure 24. LbL self-assembly according to Licciardello *et al.*[100]

For the present work, especially multilayers are interesting, which are constructed by metal-organic complexes whose organic ligands have a terpyridine or pyridine as binding units. In recent years, quite a few reports have been published.[90b, 101] Especially, the work of Licciardello *et al.*[100] is of great interest. In this study, multilayers of highly fluorescent perylene-diimides could be deposited on gold surfaces by LbL self-assembly (Figure 24). It was shown that the metal–ligand chains grow approximately perpendicular to the gold surface.

An example of multilayers, which use two different interactions, was established by Ishida *et al.*[102] Here, both coordination chemistry as well as hydrogen bonding are used as the connections between different layers. However, van der Boom *et al.*[103] used linearly coordinating palladium(II) metal-complexes for the LbL self-assembly to connect pyridyl-terminated organic ligands with each other. The multilayer structure shown in Figure 25 was obtained by an iterative two-step deposition method using identical template layers. The functionalized substrate was immersed in a solution of $PdCl_2(PhCN)_2$, washed, and subsequently dipped into a solution of the chromophore depicted in Figure 25. This was repeated until the desired layer number was obtained.

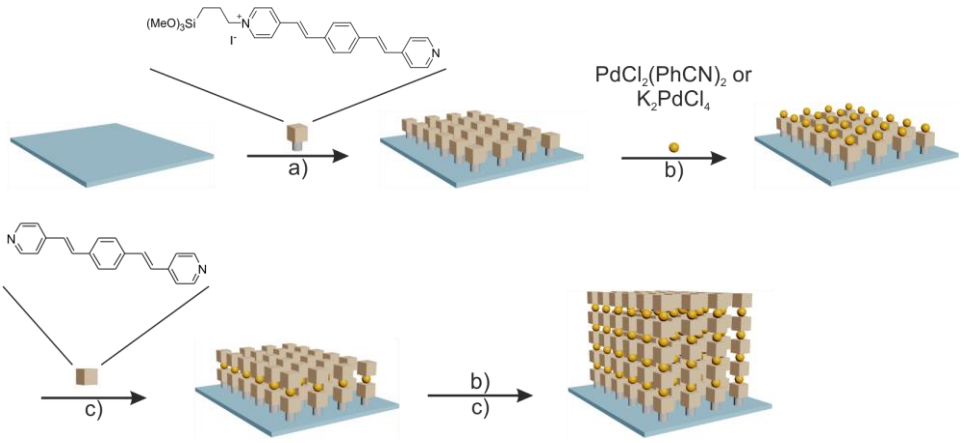

Figure 25. LbL deposition of pyridine-terminated compounds with *trans*-coordinating $PdCl_2$ according to a work of Milko van der Boom *et al.* with (a) template layer formation, (b) deposition of the metallic adhesion layer, and (c) deposition of the chromophore.[103]

Zharnikov *et al.*[104] described the preparation of ordered multilayer assemblies, namely multi-component coordination-based oligomer films on siloxane-based template layers by an immersive LbL deposition process. They combined optically rich iron and ruthenium polypyridyl-complexes with pendant pyridine groups and copper- or silver-ions as metal connector between the polypyridyl-complex moieties depicted in Figure 26. The multilayers showed a linear increase in the film thickness upon addition of every next layer, which suggests that the long-range order of the system is determined by the octahedral structure of the metal-ligand and square-pyramidal/tetrahedral geometry of the metal linker.

Recent works of van der Boom *et al.*[90b, 105] could also show the preparation of multicomponent coordination-based multilayers with several different metal centers as the connecting units. The discussed examples show that a technique, which is easy to handle, also delivers reproducible results with chemical compounds of a huge variety. Therefore, LbL self-assembly provides the perfect basis to build up surface-bound molecular machines in a bottom-up fashion.

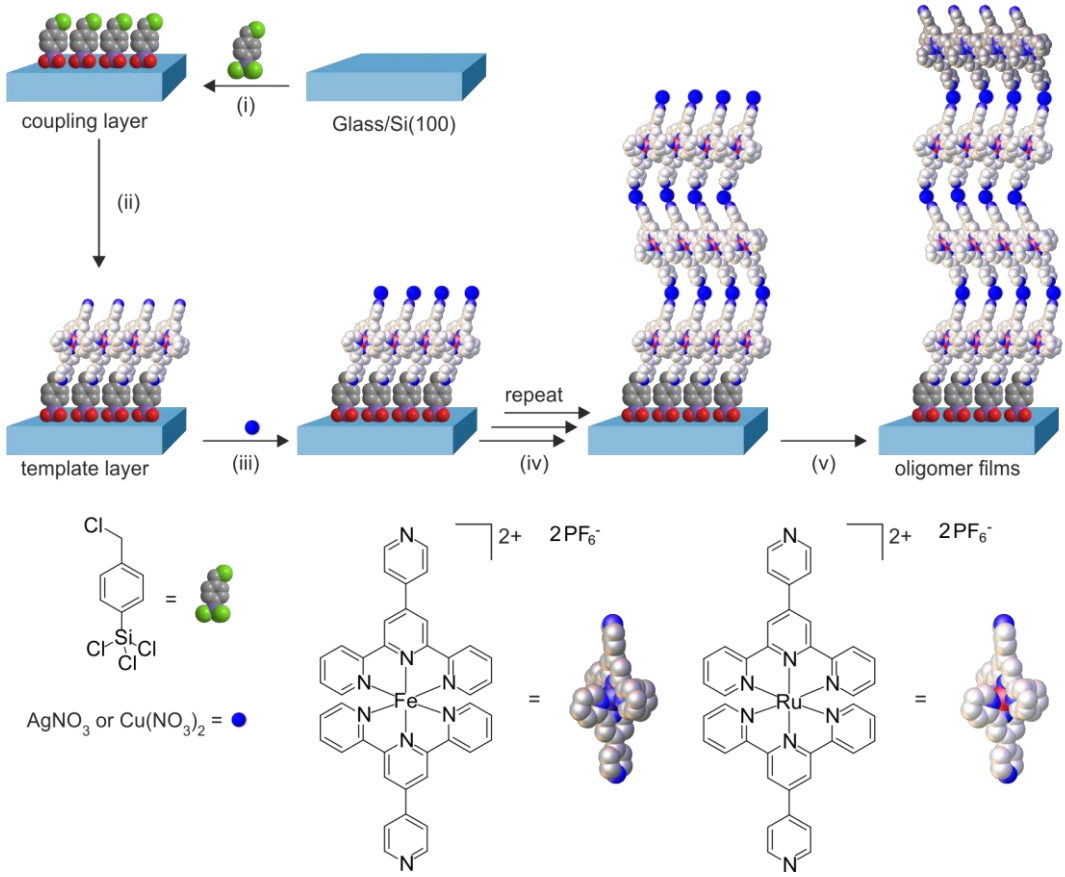

Figure 26. Multicomponent coordination-based multilayer as introduced by Zharnikov *et al.* (i) Chemisorption of trichloro-(4-chloromethyl-phenyl)-silane on hydrophilic substrates to form a "coupling layer"; (ii) covalent assembly of the first metallo-ligand to form a "template layer"; (iii) coordination of silver/copper nitrate with the terminal pyridyl groups of the template layer; (iv) repetition of steps (ii) and (iii); and (v) coordination of the second metallo-ligand with the metal-terminated oligomers. Adapted with permission from P. C. Mondal, J. Yekkoni Lakshmanan, H. Hamoudi, M. Zharnikov, T. Gupta, *J. Phys. Chem. C* 2011, *115*, 16398-16404. Copyright 2011 American Chemical Society.

3.4.5. Host-Guest Chemistry and Switchable Rotaxanes at Surfaces

The in chapter 3.3 mentioned molecular switches represent systems in relative isolation. Without a suitable reference system, even systems capable of contracting and expanding in micrometer scale as for example described by Stoddart[106] and Giuseppone[107] are difficult to utilize for practical applications. These motions are independent from each other and therefore lack the direction needed for the application of work or force. In order to direct the mechanical

motion of ensembles of molecules, certain coupling is needed to overcome the chaotic motion and therefore its reciprocal cancellation. Like already stated, monolayers assembled on surfaces should deliver the desired direction and order as they mimic the directional function of biological membranes. Three approaches to gain macroscopic effects from (supra-)molecular switches embedded into mono- and multilayers on surfaces should be discussed here: (I) A molecular switch is synthesized, provided with surface active functional group and then deposited onto the surface. (II) A reversible host-guest-complexation including pseudorotaxane formation can be established on the surface. And (III) a stimuli-addressable mechanically interlocked molecule is formed in solution prior to surface deposition. Especially the group of Ben Feringa has been pioneering on the deposition of simple molecular switches directly on the surface with three outstanding examples using overcrowded alkenes. They for example let a molecular car move a path along a surface;[108] a micrometer-sized glass rod could be directionally rotated when a liquid crystal of the switch underneath is irradiated by light;[109] and when a tripodal monolayer of the alkene switch equipped with a perfluorinated alkyl chain is deposited on a gold surface the hydrophobicity of the surface can be affected by the irradiation of UV light.[110] Moreover, Gwénaël Rapenne and coworkers showed that a molecular motor that comprises a piano-stool Ru-complex is able to perform a unidirectional rotational motion induced by the electrons from an STM tip.[111] This approach does not play a big role for the research in this work. Therefore, the focus will be on the other two approaches which use the methods of supramolecular chemistry: The first of which is the formation of host-guest complexes directly on the surface. Switchable host-guest complexes gained more and more attention in the last years. Numerous examples exist with a diverse number of hosts or guests. Two strategies exist: First a suitable macrocycle is immobilized on a surface and then a fitting axle or guest is deposited to form the desired host-guest complex or pseudorotaxane. Second, it is also possible to first deposit an axle molecule on a substrate, and then a macrocycle to bind the axle.

A macroscopic effect can be already achieved by the implementation of simple host-guest complexes. For example, numerous studies have been reported recently where the hydrophobicity can substantially be altered by different host-guest pairs.[112] This makes it potentially available for the sensing of pesticides. Li *et al.* recently published a study where calix-crown – a calixarene equipped with a partial crown ether – is deposited onto the surface by CuAAC and is the exposed to a solution of Carbaryl (G), which is a widely used and well known insecticide.[113] When the host is ‘clicked’ to an azide-monolayer, the contact angle has a value of ~160° and after the guest is deposited, the contact angle drops to the value of ~20°. The guest is then released by adding potassium ions and then a crown ether to remove the potassium. Consequently, the surface can be switched between a superhydrophobic and a highly hydrophilic state.

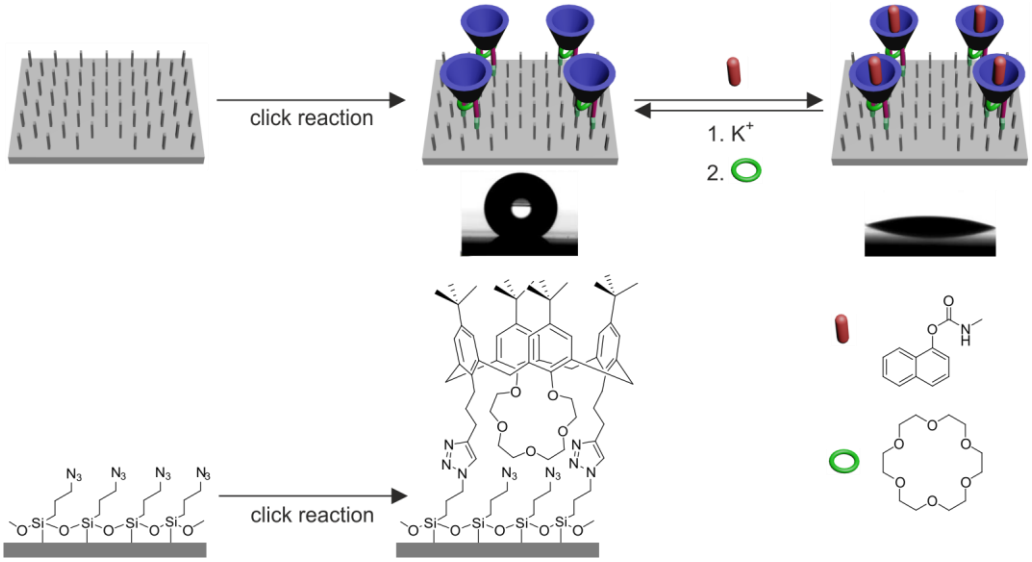

Figure 27. Illustration of the calixcrown deposition-process and the subsequent reversible host-guest experiments which lead to a significant change in surface wettability.[113]

The same group very recently reported a pillararene-functonalized surface which is slippery for pure water but when the solution contains a tiny amount of methylviologen or paraquat, which is used as contact herbicide, the water droplet sticks to the surface as a result of the dynamic host-guest complex formation.[114]

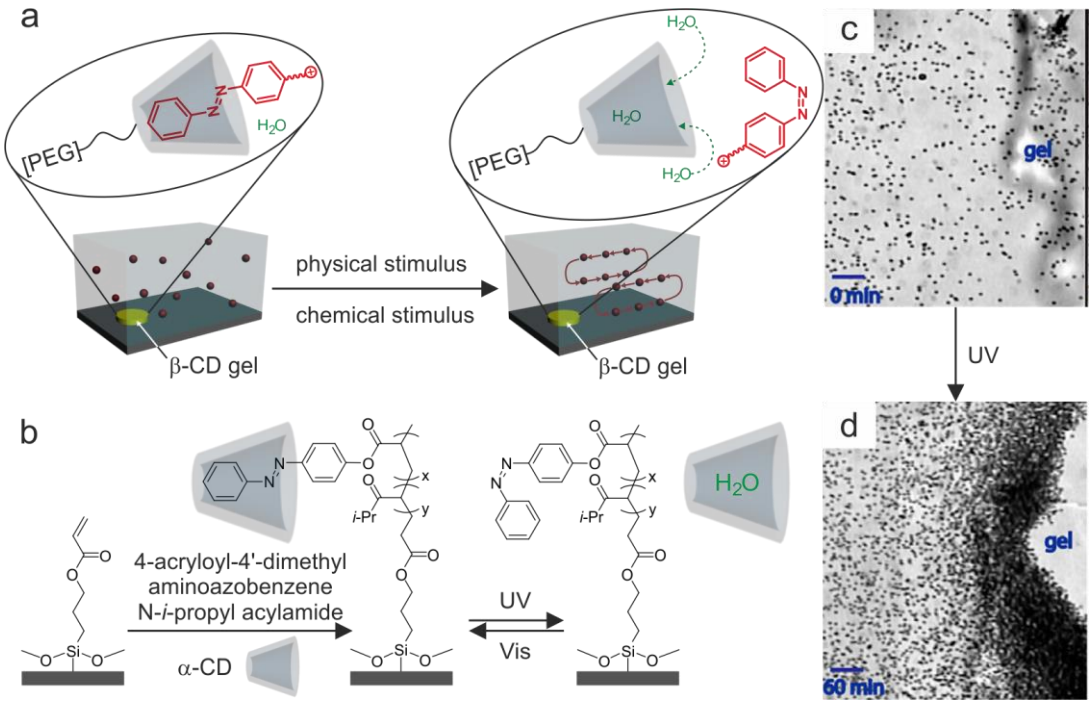

Figure 28. (a) Schematic illustration of the dual-responsive micropump on a glass surface reported by Sen and coworkers. (b) Illustration of the direct functionalization of glass surfaces by covalently tethering azobenzene-containing molecules and the reversible formation of the host-guest complex with α-cyclodextrin. (c) Solution with trace particles before light-irradiation and (d) after 60 min of irradiation.[115]

Another example, where a macroscopic effect is achieved by the implementation of host-guest chemistry or molecular recognition on interfaces, was published by Patra *et al.* in 2014.[115] The They demonstrated that host-guest molecular recognition between α- and β-cyclodextrin and *trans*-azobenzene can induce the movement of small particles in a solution and thereby constructed a micropump. The host-guest complexes can form both within hydrogels and on surfaces. Both hydrogels and surface coatings based on the host-guest partners were used as scaffolds to devise the micropumps. These soft micropumps are dual stimuli-responsive and can be actuated either by light or by introducing guest molecules. Upon UV light absorption, the azobenzene molecules isomerize into their cis-isomer which leads to the dissociation of the host-guest complexes. The cavities of the cyclodextrin-hosts are then filled with water molecules which induces a steady flow of fluid around the surface towards the gel at the rate of ~2 µm/s. The same happens when a chemical stimulus is applied: An adamantane guest is able to replace the azobenzenes from the cyclodextrins and thus as well creates a fluid flow. The micropumps can also be recharged through reversible host guest interactions.

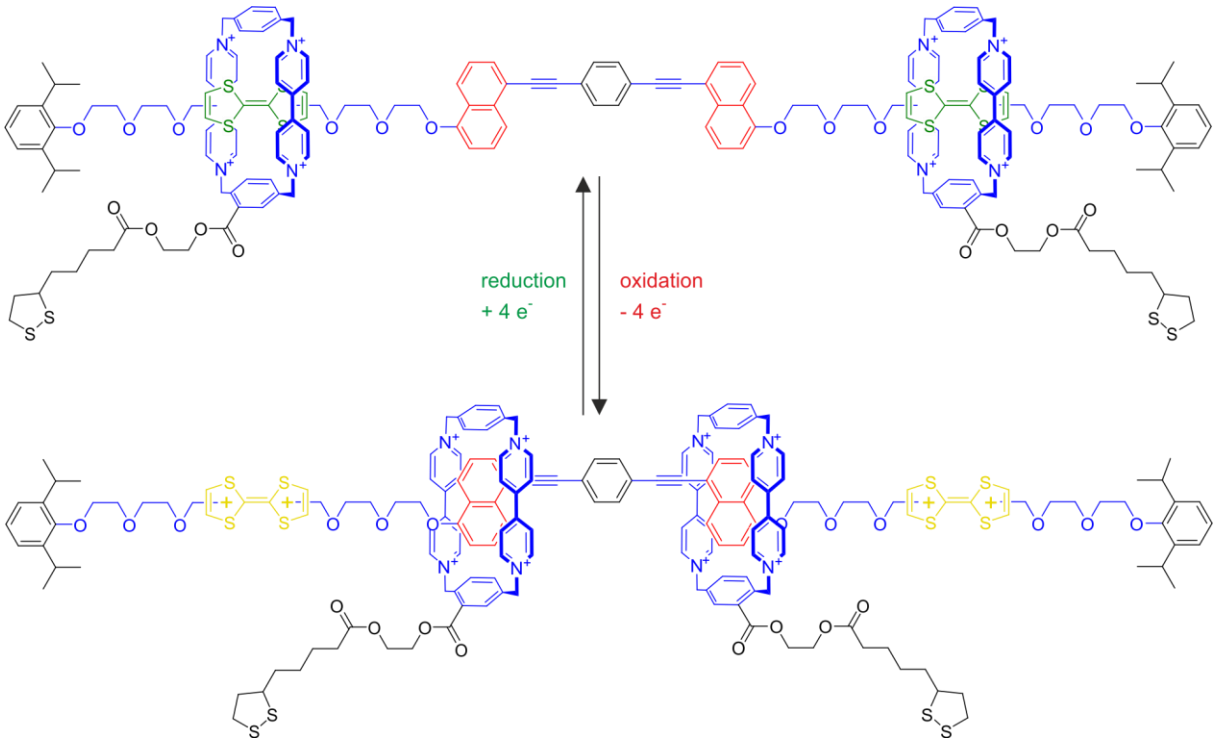

Scheme 3. Molecular structure of the redox-switchable [3]rotaxane that can be deposited onto gold surfaces via the attached lipoic acids.[116]

An outstanding example of the third approach was presented by the group of Fraser Stoddart in the year 2005.[44, 116] Here, a switchable [3]rotaxane, which consists of an axle and two mechanically mobile macrocycles, is deposited onto a gold cantilever.

The axle has two different binding sites, of which four are arranged symmetrically on the axis. The cyclobis(paraquat-p-phenylene) ($CBPQT_4^+$) macrocycles are also symmetrical coordinated on the axis. In the reduced initial state, they are located on the outer tetrathiafulvalene (TTF) binding sites. If the TTFs are now oxidized, the macrocycles move to the inner naphthalene (NP) stations (Scheme 3). This leads to a decrease of the distance between the two macrocycles from 4.2 nm to 1.4 nm. In order to make the rotaxane available for surface deposition, the macrocycles are functionalized with lipoic acids. A monolayer of these rotaxanes is then deposited onto a gold cantilever.

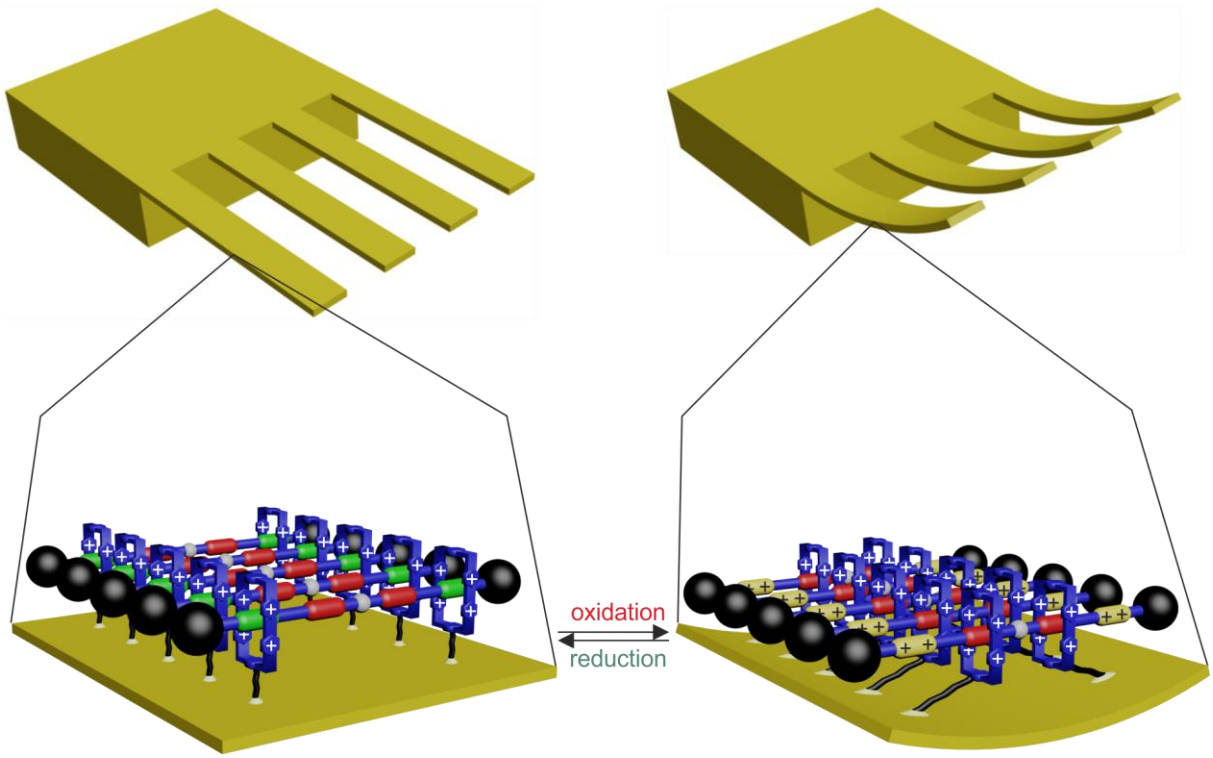

Figure 29. Schematic representation of the electrochemically controlled bending and relaxation of cantilever on top of which a monolayer of the previous described [3]rotaxane is deposited.[116]

If the TTF binding sites are oxidized, the macrocycles move inwards and the cantilever is forced into a bending position which leads to a curvature of up to 35 nm (Figure 29). 'Relaxed' by a subsequent reduction of the TTFs, the cantilever returns into its initial position again. This electrochemically controlled contraction and relaxation process may be repeated in several cycles and emulates the movement of a natural muscle.

When the rotaxane discussed in chapter 3.3 (Figure 8) is modified in a certain way it can be deposited to a monolayer of 11-mercaptoundecanoic acid and its switching can lead to a macroscopic effect.[117] By irradiation of the surface-deposited rotaxanes, it is possible to move a diiodomethane droplet uphill. The switching mechanism obviously resembles the one of the previously described rotaxane. However, the weaker binding diamide-station was equipped

with fluorines instead of hydrogens in order to have a significant polarity difference between the stations. The terminal pyridines at the macrocycle enable the rotaxane's surface-deposition. The switching process is again initiated by a photo-induced E/Z isomerization of the double bond in the fumaramide-station, which affords a 50:50 mixture of E/Z isomers, so that about half of the macrocycles translate along the axles. If this rotaxane is deposited onto a surface, the wettability of the surface should be significantly influenced by the switching process.

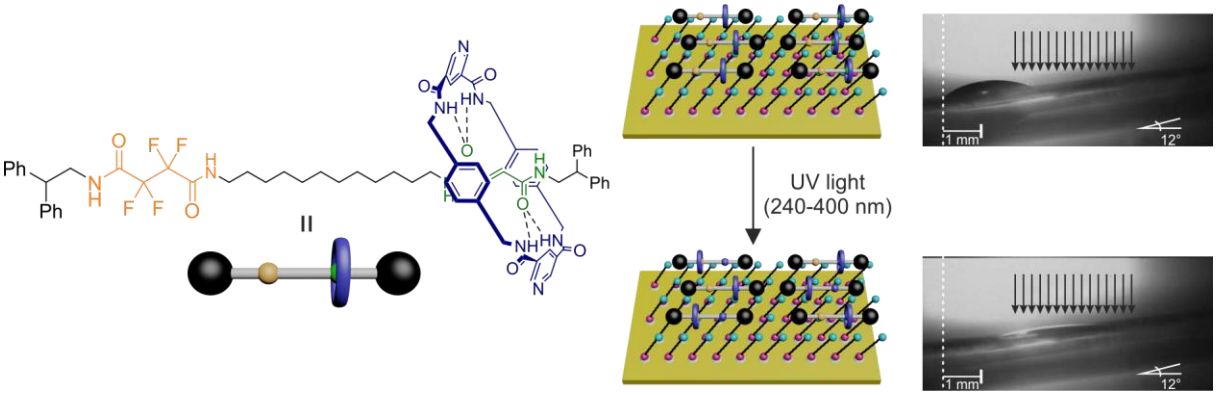

Figure 30. Uphill movement of a droplet along a surface functionalized with a switchable surface when its irradiated with light. Reprinted and adapted by permission from Macmillan Publishers Ltd: Nature Materials (J. Berná, D. A. Leigh, M. Lubomska, S. M. Mendoza, E. M. Pérez, P. Rudolf, G. Teobaldi, F. Zerbetto, *Nat. Mater.* 2005, *4*, 704-710.) copyright (2005).

The described rotaxane was deposited in an organized fashion and was switched by light with a wavelength of 254 nm. Due to the isomerization of the double bond, 50% of the macrocycles bind to the perfluorinated station. This significantly changes the wettability resulting in the uphill-movement of the diiodomethane (Figure 30). Back-switching only occurs upon heating the system.

These examples clearly demonstrate that there are quite already useful applications for switchable rotaxanes. However, the mechanical energy generated could not be harnessed and it has not yet been proven to be ordered or even directional. Therefore, new approaches must be developed and followed, that can help to accomplish the set goal.

Recently, Stephen Loeb and coworkers reported a possibility to put the rotaxanes in line by incorporating them into a metal-organic framework (MOF).[118] They applied the method of modifying the organic strut in a way that it can be utilized as the axle of a rotaxane. In fact, it is a molecular shuttle that operates inside a Zn-based MOF where a [24]crown-8-ring performs a degenerate shuttling motion between two benzimidazole recognition sites on an H-shaped organic molecule with two triphenyldicarboxylic acid struts. Consequently, the dynamical motion of the crown ether has a significantly higher energy barrier when the rotaxane is incorporated into the framework than in solution.

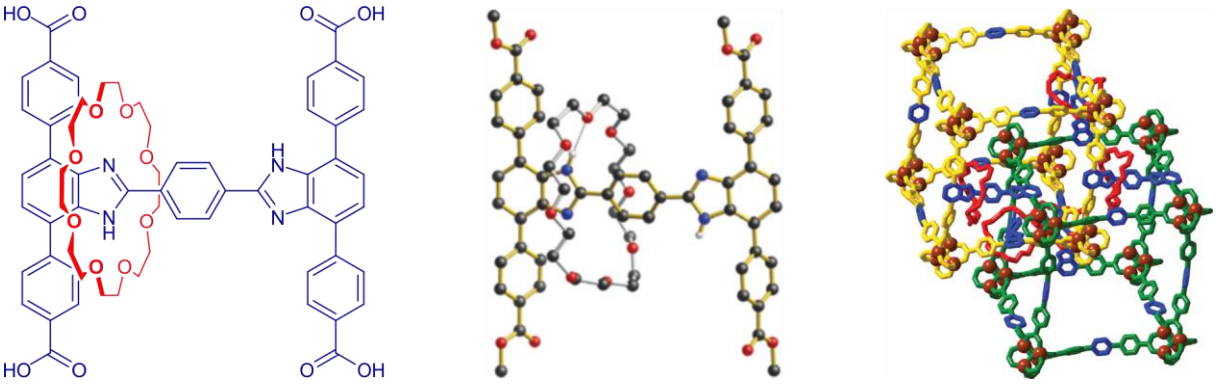

Figure 31. Molecular structure (left) and X-ray structural characterization (middle) of the rotaxane linker used by Loeb *et al.* to construct a well-ordered framework with an incorporated molecular shuttle. Right: Two cubes of the lattice formed by the triphenyl struts (green and yellow) with connecting crossbar MIMs (axle in blue and wheel in red); only crossbars actually connecting these two cubes are shown. Reprinted by permission from Macmillan Publishers Ltd: Nature Chemistry (K. Zhu, C. A. O'Keefe, V. N. Vukotic, R. W. Schurko, S. J. Loeb, *Nat. Chem.* 2015, *7*, 514-519.) copyright (2015).

A second example also shows how rotaxanes can be embedded into the ordered structures of MOFs subsequent to the formation of the frameworks. Omar Farha and Fraser Stoddart and coworkers developed a strategy for the organization of MIMs within the channels of a MOF by a postsynthetic approach.[119] A pseudorotaxane, which first forms in solution, binds to the co-ordination site of the MOF. In this way, it is immobilized in the structure of the MOF and also undergoes the transition to a kinetically trapped rotaxane under relatively mild conditions, which possibly makes it applicable for also other supramolecular systems. Although the described rotaxane does not undergo a mechanical switching, the study showed that the rotaxane incorporated in the MOF is in principle electrochemically addressable to some extent.

The understanding of the assembly of artificial molecular machines at interfaces or in the solid state is crucial for their implementation into bigger systems. For that, it is necessary to find suitable methods to get an insight into the processes happening in/at the aimed phases. In the solid phase, X-ray crystallography as well as solid-state NMR are necessary to solve the dynamic/static features of (interlocked) molecules. For surfaces as used in this work, various methods are available. The ones utilized to get an understanding of the assembly process as well as the behavior upon an external stimulus of the used supramolecules, will be extensively described in the following chapter in order to comprehend the importance of the gained results in this work.

3.5. Characterization of Organic Thin-Films

A detailed and reliable understanding of molecular geometric and electronic properties is highly important for a fundamental analysis of the macroscopic and microscopic behavior of materials. For functionalized interfaces this rather general statement is even more accurate as the enormous importance of molecular properties for the general behavior of nano-, macro- and micro-scaled systems is accompanied by a huge experimental challenge to gather this information. These problems are caused by the fairly small amount of material, which governs the properties of an interface.[120] Therefore, a reliable characterization of interfacial properties requires the utilization of highly surface-sensitive methods. Regarding the elemental as well as chemical characterization of interfaces, the development of energy dispersive analyzers (1960s) in succession of the quantum mechanical interpretation of the photoelectric effect and ultra-high vacuum (UHV; $<10^{-7}$ mbar) techniques as a consequence to improved pumping systems lead to the introduction of X-Ray photoelectron spectroscopy (XPS). This discovery had the largest impact to the improvement of surface characterization. Following that, imaging techniques for surface analysis like scanning tunneling microscocopy or atomic force microscopy in the 1980s have been developed which made the analysis easier to conduct and to interpret as they delivered direct results in the form of images that show direct results. In order to gain a proper picture of the processes, it is necessary to apply a number of complementary methods.

3.5.1. Transmission UV/Vis-Spectroscopy

UV/Vis spectroscopy – usually used for liquids/solutions – is subject to the principle that electrons of a chemical compound are excited by electromagnetic radiation in the ultraviolet and visible region (λ = 200 nm - 800 nm) into a high energy state. Hereby, it is important that the energy of the irradiant light is exactly equal to the energy gap between binding (occupied) and antibonding (unoccupied) orbital.

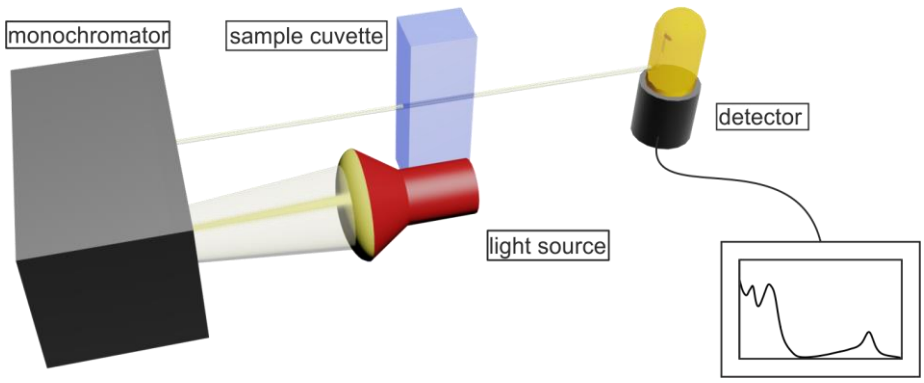

Figure 32. Schematic representation of a single-beam UV/Vis-spectrometer.

Light of the appropriate wavelength is absorbed by the sample, which is then detected and can give an indication of the investigated compound. In a UV/Vis experiment, the intensity change ($I = I_0 - I_{abs}$) of a monochromatic light beam (initial Intensity I_0) with the wavelength λ, that is directed through a homogeneous solution with the layer thickness d and the concentration c, is measured. Figure 32 shows how this is done in a single-beam spectrometer. The extinction E_λ of the solution can be calculated following the Lambert-Beer law.

$$E_\lambda = \lg\left(\frac{I_0}{I_{abs}}\right) = \varepsilon_\lambda \cdot c \cdot d$$

Equation 1. Lambert-Beer-law; ε_λ: molar attenuation coefficient, I_0: intensity of the incident beam, I_{abs}: intensity of the emerging beam, c: concentration, d: layer thickness.

The radiation excites transitions of molecular electrons with different properties in organic molecules. While π → π* transitions occur because of their smaller splitting at wavelengths in the far-ultraviolet range up to the visible range, σ → σ* transitions occur due the comparatively large splitting at shorter wavelengths and thus usually out of the spectrometer range. Thus, especially π → π* transitions but also electron excitations into non- or anti-bonding orbitals (HOMO-LUMO transitions) are detected by UV/Vis spectroscopy.

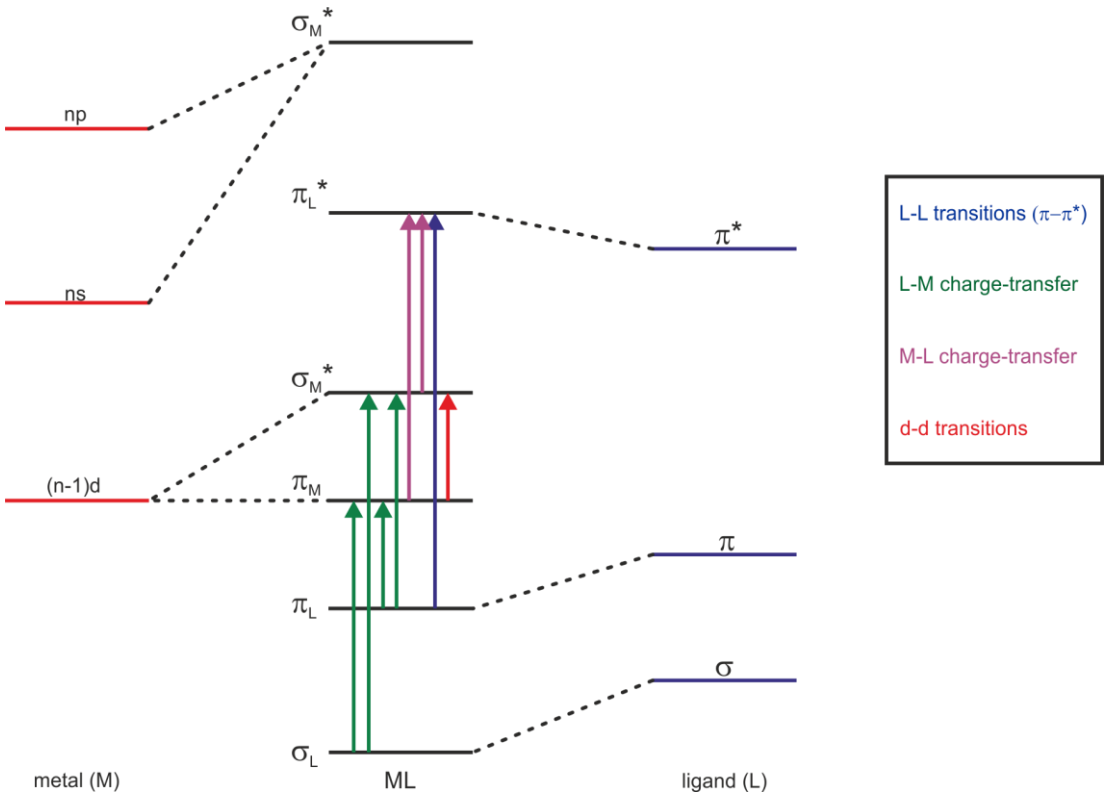

Figure 33. Simplified MO diagram for a generic transition metal complex and relative spectroscopic excitation transitions.

In metal-organic complexes, three additional transitions can play an important role – for example, the electron transitions from the metal to the ligand (metal-to-ligand charge transfer, MLCT), where the metal acts as the electron donor (d-orbital) and the ligand as acceptor (π*-orbital). These are primarily present in charge-transfer complexes with metal ions that have a low oxidation number and with ligands having low-lying π* orbitals, especially aromatic ligands. In the opposite case, in which a charge-transfer from ligand to metal (ligand-to-metal charge-transfer, LMCT) takes place, electron-poor and therefore highly charged metal-ions are particularly the reason for the transfer and therefore for occurring colors. Finally, the already described π → π* transitions (ligand-centered, LC band) and also the d-d-transitions at the metal center occur (Figure 33).

Usually, UV/Vis spectra are recorded for substances in solution. In order to investigate the on-surface formed complexes in this work, semi-transparent surfaces instead of the usual cuvettes are placed in the sample chamber of a commercially available spectrometer. A wide variety of substrates are used, such as quartz-glass slides[103, 121] or thin films (up to 20 nm) of gold films deposited by chemical vapor deposition on glass.[122] For the examination by transmission UV/Vis spectroscopy, very large systems that possess a strong absorption band, such as biomolecules or nanoparticles, are particularly suitable, because otherwise the intensity is too low to make appropriate observations regarding the amount of compound that is deposited. In the present work, this method was used to investigate the layer-by-layer growth since the increase of a possibly present absorption band in the layer growth can be detected.

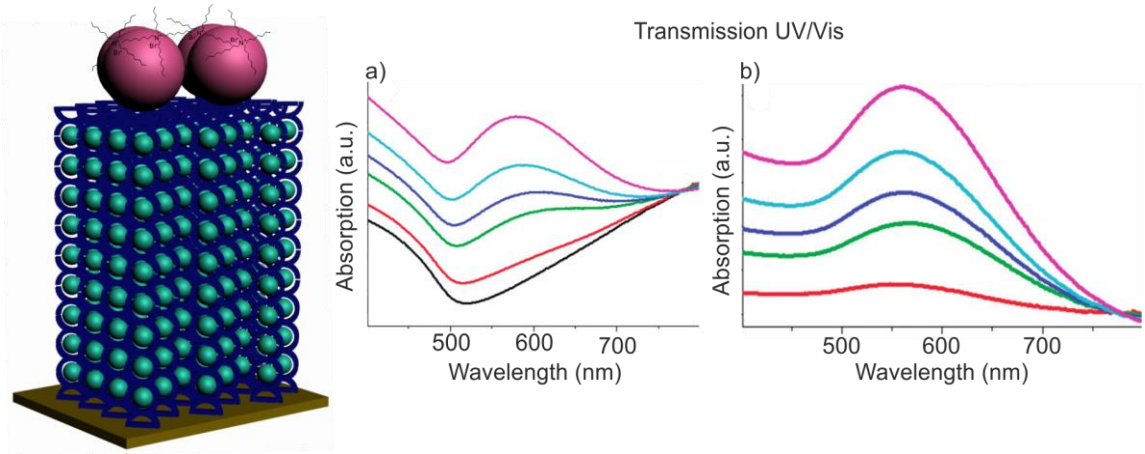

Figure 34. Metal-organic multilayer with a capping nanoparticle layer and the corresponding transmission UV-vis spectra for the coordination self- assembly of gold-nanoparticle multilayers according to Rubinstein *et al.* (a) Spectra obtained using a semitransparent continuous gold substrate; the lowest curve is the spectrum of the bare gold substrate, with spectra of increasing intensity corresponding to consecutive NP binding steps. (b) Difference spectra obtained by subtracting the spectrum of the bare gold from the other spectra in part a. Reprinted and adapted with permission from Y. Chaikin, H. Leader, R. Popovitz-Biro, A. Vaskevich, I. Rubinstein, *Langmuir* 2011, *27*, 1298-1307. Copyright 2011 American Chemical Society.

Previous works by van der Boom *et al.*[103] and Rubinstein *et al.*[99] have successfully applied this procedure (See also sec. 3.4.4). While van der Boom *et al.* used an alternating deposition of linearly coordinating palladium and pyridine-functionalized organic compounds, Rubinstein *et al.* could produce multilayers which contain both organic ligands as well as gold-nanoparticles and examine them with UV/Vis spectroscopy. Figure 34 shows an organic multilayer terminated with a layer of gold-nanoparticles. Based on their gradually increasing absorption – with a characteristic maximum at 570 nm – the layer-by-layer growth of the nanoparticle multilayer can be detected.

Figure 35 shows UV/Vis measurements of the $PdCl_2$-based assembly described in chapter 3.4.4 (Figure 25) that exhibit a linear correlation between the absorption at λ_{max} and the number of organic layers, indicating that this deposition scheme results in the formation of a microstructurally regular multilayer. Another prominent feature is the progressive bathochromic shift in the absorption maximum with each additional layer from 337 nm for the template layer to 379 nm at layer 13, indicating electron communication between the topmost layer and the substrate, and possible *J*-type aggregation.[123]

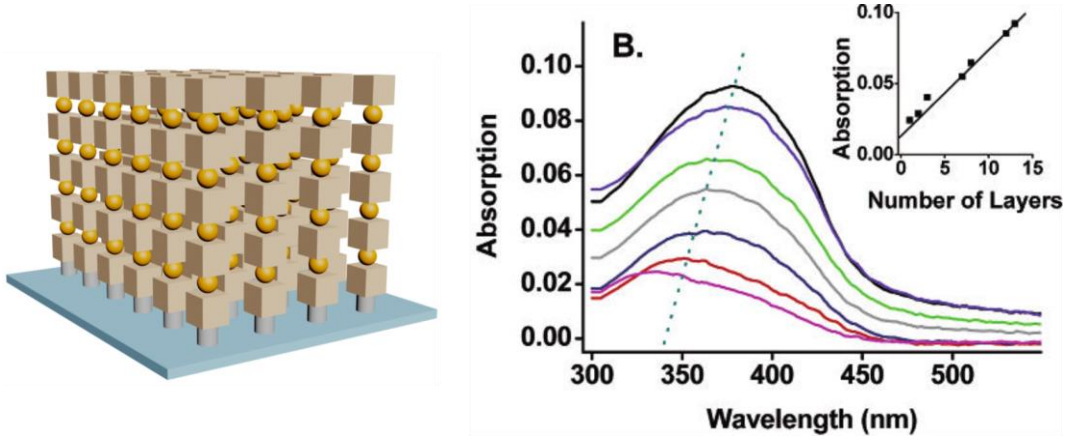

Figure 35. UV-vis spectra from van der Boom *et al.* for selected layers of a $PdCl_2$-based assembly showing a shift in λ_{max} from 337 to 379 nm for layers 1-13, including a linear fit of the 23 nm shift for layers 2-13 (dotted line). Inset: Optical absorption at λ_{max} nm for layers 1, 2, 3, 7, 8, 12, and 13 of a $PdCl_2$-based multilayer. Reprinted and adapted with permission from M. Altman, A. D. Shukla, T. Zubkov, G. Evmenenko, P. Dutta, M. E. van der Boom, *J. Am. Chem. Soc.* 2006, *128*, 7374-7382. Copyright 2006 American Chemical Society.

Another example for the use of transmission UV-Vis spectroscopy of LbL self-assembled multilayers prepared on semi-transparent gold substrates delivers the work of Licciardello *et al.*[100] The UV/Vis spectra of the films show that the typical band of the perylene bisimide iron complex at 580 nm grows with the number of coordination steps (a) on top of the broad gold plasmon band centered at ca. 600 nm. Moreover, the linear correlation between the maximal absorption at 589 nm and the nominal number of layers (b) indicates the formation of a constant number of iron complexes per step.

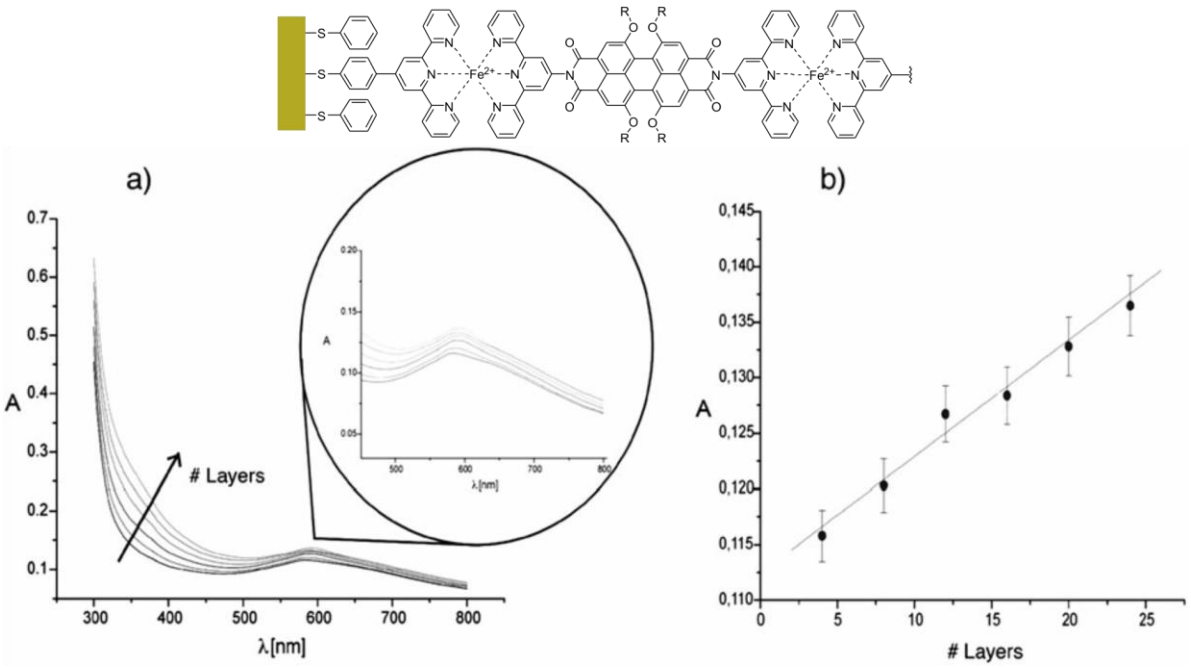

Figure 36. (a) UV-Vis spectra acquired from an increasing number of layers (4–24) and (b) optical density of the characteristic multilayers band at 589 nm as a function of the nominal number of layers. Reproduced from N. Tuccitto, I. Delfanti, V. Torrisi, F. Scandola, C. Chiorboli, V. Stepanenko, F. Würthner, A. Licciardello, *Phys. Chem. Chem. Phys.* 2009, 11, 4033-4038 with permission from the PCCP Owner Societies.

3.5.2. X-Ray Photoelectron Spectroscopy (XPS)

While UV/Vis-spectroscopy is only exceptionally used for the analysis of surfaces, photoelectron spectroscopy can be considered as an information-rich, classical method for surface analysis. It can give – among others – qualitative as well as quantitative information on all the elements present at concentrations > 0,1 atomic-% (except for H and He), semi-quantitative determination of the approximate elemental surface composition (error < ±10%) and information about the molecular environment (oxidation state, covalently bonded atoms, etc.). Furthermore, it is possible to measure non-destructive elemental depth profiles 10 nm into the sample, to do a surface-heterogeneity assessment using angle-dependent XPS studies, and also lateral variations in surface composition (down to a resolution of 40 nm) can be detected. The method in general is based on the outer photoelectric effect, in which photoelectrons can be excited and liberated out of a solid by electromagnetic radiation (photons).[124] Three events may occur when a photon impinges on an atom present on the surface: First, the photon can pass through with no interaction. Second, it can be scattered by an atomic orbital electron resulting in partial energy loss – referred to as Compton scattering – important for high-energy processes. And third, the photon interacts with an atomic orbital electron with a total energy transfer to the electron leading to its emission from the atom. This characterizes the essential

element of the photoemission process that is the basis of the XPS experiment.[125] Depending on the energy of the photons, there are various fields in photoelectron spectroscopy. In the case of ultraviolet-photoelectron spectroscopy (UPS), solids are irradiated by ultraviolet radiation (5 - 50 eV), which has enough energy to excite the valence electrons of a compound or an atom giving information. X-ray photoelectron spectroscopy (XPS) uses excitation energies of about 100 up to 10^6 eV, which is enough to extract underlying core-electrons from the surface.

$$E_B = h\nu - E_{kin} - \phi$$

Equation 2. The modified Einstein-equation with E_B as the binding energy, hν as the energy of the X-ray source, E_{kin} as the (measured) kinetic energy and ϕ as the sample specific work function.

The emitted photon electrons have a certain kinetic energy which is linearly proportional to the frequency of the exciting photons – if photons with higher energy than the needed threshold value are used, the excess photon energy is transferred to the emitted electrons. To obtain the characteristic binding energy, Equation 2 is applied, where the kinetic energy and the specific work function φ of the spectrometer are subtracted from the incident photon energy hν.
The binding energy E_B corresponds to the binding energy of the electron in a certain atom-orbital that is characteristic for the present chemical element(s). For this reason, XP-spectroscopy is also frequently referred to as Electron Spectroscopy for Chemical Analysis (ESCA).

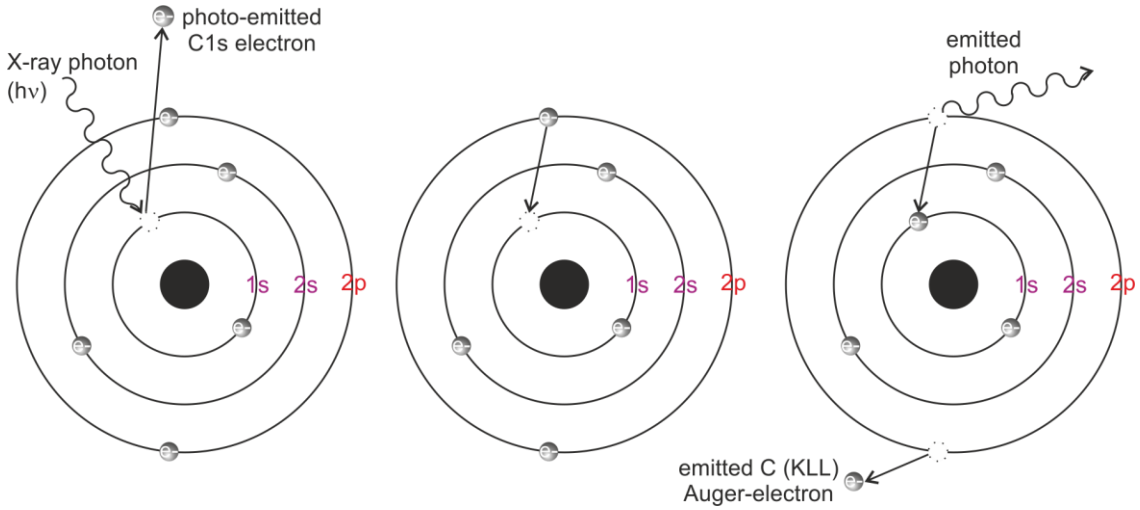

Figure 37. Left: The X-ray photon transfers its energy to a core-level electron imparting enough energy for the electron to leave the atom (photoemission); middle: The atom in an (n-1)-electron state relaxes by dropping an electron from a higher energy level to the vacant core hole; right: Emission of an electron (Auger-electron) or a photon (fluorescence) resulting from the excess energy due to the electron transition.[125]

In Figure 37 (left), it is shown that an energetically unfavorable core-electron hole remains after the emission of a photoelectron. To compensate this state, the hole is filled with an electron from a higher energy level, first. The energy is then released as radiative (fluorescence) or non-radiative (Auger electron) relaxation decay of the core hole which can be referred to as so-called secondary processes. Auger electrons have a kinetic energy which is independent from the excitation energy, can also be detected by an XPS detector and therefore give evidence for the emissive element in the same way. Both processes are also the subject of other spectroscopic methods (AES, XRF) that are not described in this work.

The development of techniques that achieve a vacuum of up to 10^{-11} mbar provides an essential factor for the development of XP spectroscopy. The generated photoelectrons can not be detected under normal conditions as they would be inelastically scattered by the molecules in the atmosphere. There have been admittedly recent advances leading to spectrometers which are working at pressures of up to 100 mbar. This is achieved by planting the analyzer directly above the surface with a distance in the µm-area and using multiple steps of differential pumping.[126] For traditional XPS experiments however, the vacuum chamber shown in Figure 38 is the core element, where a vacuum of ca. 10^{-9} mbar is present.

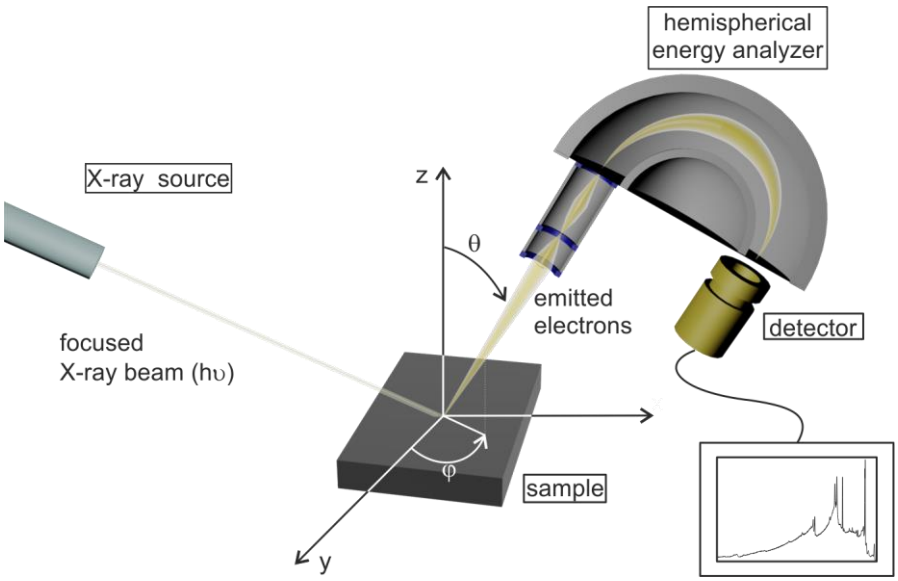

Figure 38. Schematic representation of an XPS-experiment.

At the beginning of a measurement an X-ray beam is focused on the sample. The energy of the beam can be both monochromatic (Al-Kα radiation has an hν of 1436.6 eV) or have a wide range (synchrotron radiation (See chapter 3.5.3)). Subsequently, photoelectrons are emitted from the sample and then taken up by the inlet opening of the lens system. This array is – depending on the analyzer – composed of successively mounted magnetic and electrostatic lenses. It is positioned at a certain angle to the sample and used for focusing the electrons. By

changing the positional angle θ, the level of surface sensitivity can be adjusted. For example, the analysis is substantially more surface-sensitive at θ = 60° than at θ = 0°. Additional to collecting the photoelectrons, the lens system also retards their kinetic energy (KE) to a certain value. Subsequently, electrons that are not retarded completely by the lens due to their higher kinetic energy enter the hemispherical electron-analyzer, which consists of two concentric hemispheres and is adjusted to detect only electrons within a certain energy window (pass energy of the analyzer, PE). After passing the analyzer, the electrons hit the detector.

In order to allow a sufficient analysis by XPS, it is important to understand the influence of the chemical environment to both, the spectral characteristics, as well as the binding energy. Usually, the electron count rate is depicted in an XP spectrum in dependence of the binding energy, which is calculated as shown in Equation 2 and is therefore inversely linear dependent on the kinetic energy of the emitted photoelectrons. The resulting picture is characteristic for every element and can thus give qualitative and semi-quantitative indications for the elements present.

Figure 39 shows a survey spectrum with an energy range of 1200eV. In the spectrum, a stepwise increasing background – schematically traced by the red dotted line – is visible which rises after every intense element signal and then slowly decreases at higher binding energies. This background portrays the electrons that lost a part of their energy due to inelastic scattering but are able to escape the surface. These can therefore be detected and have a continuous kinetic energy.

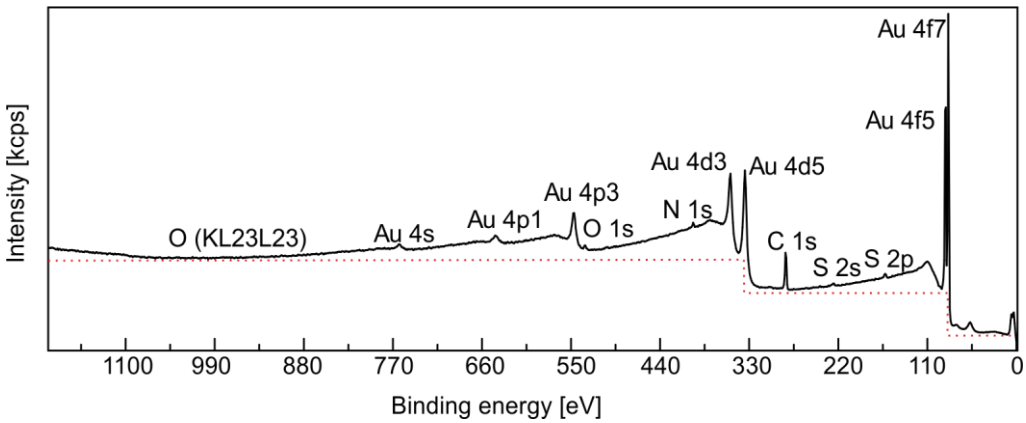

Figure 39. Survey spectrum of a terpyridyldodecane thiol monolayer on a gold-substrate (hν = Al-Kα, pass energy = 80 eV, θ = 0°).

Furthermore, there are two kinds of signals visible. Those can be divided into the already mentioned photoemission signals that are corresponding to the photo-induced ionization of the atoms and the thereby induced Auger electrons. While latter have an excitation source independent kinetic energy and therefore can be observed at different values in the binding-energy spectrum, the kinetic energy of the photoemission electrons is shifted dependently on the

source's energy. To further explain the spectrum's features, gold is taken as an example. It becomes clear that several spectral lines are possible for a single element. In this special case, (strong) emissions should be visible at binding energies of 759 eV (4s), 644 eV ($4p_{1/2}$), 546 eV ($4p_{3/2}$), 352 eV ($4d_{3/2}$), 334 eV ($4d_{5/2}$), 87 eV ($4f_{5/2}$), and 84 eV ($4f_{7/2}$). Especially when the most prominent signals at 87 and 84 eV cannot be observed, it can be assumed that gold is not present on the surface – at least in the detectable depth; the upper most 10 nm. Gold can serve also as an example for the following observable feature: Photoelectrons emitted from atomic orbitals with an azimuthal quantum number larger than 0 (open shell) – like p-, d- and f-orbitals – undergo a spin-orbit splitting.

In Figure 40, the initial state and the final states of an electron pair in a 3p-orbital are schematically illustrated. Two energetically equivalent final states are possible which are either parallel (spin up, s= +1/2) or anti-parallel (spin down, s = -1/2) to their corresponding orbital angular momentum. If there is an open shell (see above) with two states of the same energy, a magnetic interaction of the electron spin and the orbital angular momentum called spin-orbit coupling or *j-j* coupling (quantum number j = |l + s|) occurs and leads to a splitting of the degenerate state into two components. Figure 40 also shows common spin-orbit pairs. The ratio of their degeneracies (2j + 1) then determines the intensity of the signals.

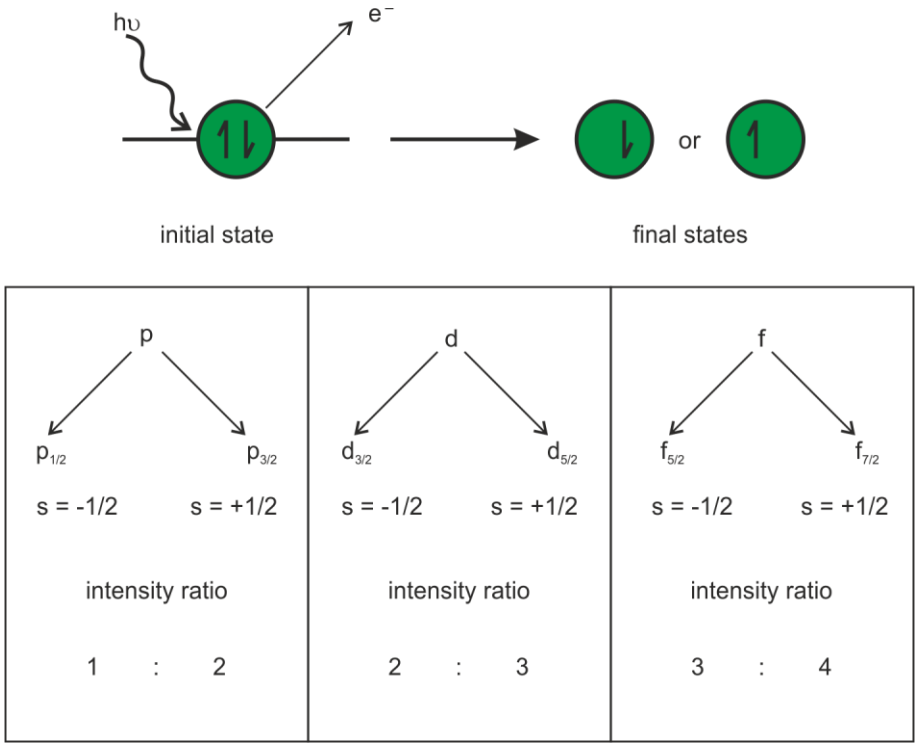

Figure 40. Schematic illustration of the spin-orbit splitting process.[125]

On a second glance at the spectrum in Figure 39, more elements apart from gold can be identified. For example, the characteristic signals at around 400 eV representing the nitrogen 1s photoelectrons and at ca. 285 eV for the carbon 1s emission. In order to get additional information about these elements, high-resolution spectra are measured as the binding energies of the corresponding electrons can be investigated in more detail. General speaking, the binding energy of a photoelectron can be considered as the energy difference between the initial state and the final state of the emitting atom. For the initial state of the atom, the effects of the chemical environment play a crucial role as the alteration of it leads to a different binding energy. If, for example, the formal oxidation state of an atom is increased, the binding energy of the resulting photoelectron usually rises, too. Thus, the binding energy of a carbon 1s electron in an amide group lies at 288.2 eV due to the higher formal charge of the atom while the binding energy of a 1s electron in an aliphatic carbon lies at 285 eV.[125] This is in general called the chemical shift in XP spectra. In the course of the ionization, the resulting electron density redistributes in the emitting atom to minimize the energy. The resulting energy is called relaxation energy E_r, which also contributes to the resulting calculated binding energy as it has an influence on the final state of the emitting atom and consists of internal and external relaxation. The internal relaxation originates from the reorganization of the electron in the core and valence shells. The external relaxation, on the other hand, depends on the investigated material. While the electron holes can be rapidly filled in electronic conducting materials, insulators inhibit a quick compensation of those. In this work, the effects on the final state do not play a significant role as similar material is used for the presented studies.

Often, a photoemission consists of several components that add up to a total signal. In order to enable a qualitative and quantitative description of the individual components, a peak-shape model function is adapted to the measured spectrum, which represents the sum of the functions of the individual components. This is called peak fitting. A detailed explanation of the theoretical background of peak fitting is given elsewhere.[127]

In a recent study, the Schalley group investigated the potential of pyridine-terminated SAMs to coordinate Pd-complexes with a competitive protonation of the pyridyl nitrogen in a detailed XPS study. In order to do that, the high-resolution N 1s XP spectra of the particular chemical modification steps had to be investigated and the N 1s spectra were interpreted by fitting suitable nitrogen peaks into the spectrum and evaluate them concerning their chemical shift and therefore their molecular properties. The pristine SAM (Figure 41a) exhibits one large component peak at BE = 399.7 eV characteristic for the unmodified pyridyl nitrogen accompanied by minor components at higher BEs. These minor components can be assigned to H-bonded (400.9 eV) and protonated (402.3 eV) pyridyl nitrogens.[128] After treatment of the SAM with sulfuric acid, a significant binding energy shift of the major N 1s component to 401.9 eV is

observed indicating the protonation of the pyridine (Figure 41b) while a small amount of unmodified nitrogen at BE = 399.8 eV remains. Rinsing with ethanol restores the major peak for unmodified pyridine nitrogen at BE = 399.7 eV which implies a successful deprotonation step (Figure 41c). However, a part of the pyridyl nitrogens remains protonated or H-bonded. The SAM exhibits significant changes of the N 1s peak after deposition of the Pd(II) complex (Figure 41d): The major component is now observed at a higher BE of 400.8 eV which is assigned to pyridyl and acetonitrile nitrogens coordinating to Pd(II) ions and reveals complex formation with a yield of roughly 90%. The protonated sample shows a different behavior (Figure 41e): Only few of the pyridyl nitrogens coordinate. Only less than 60% of the pyridine nitrogen atoms were complexed by the metal. As also expected, after deprotonation of the PDT SAM, almost complete coordination of pyridines to Pd(II) is possible again (Figure 41f).

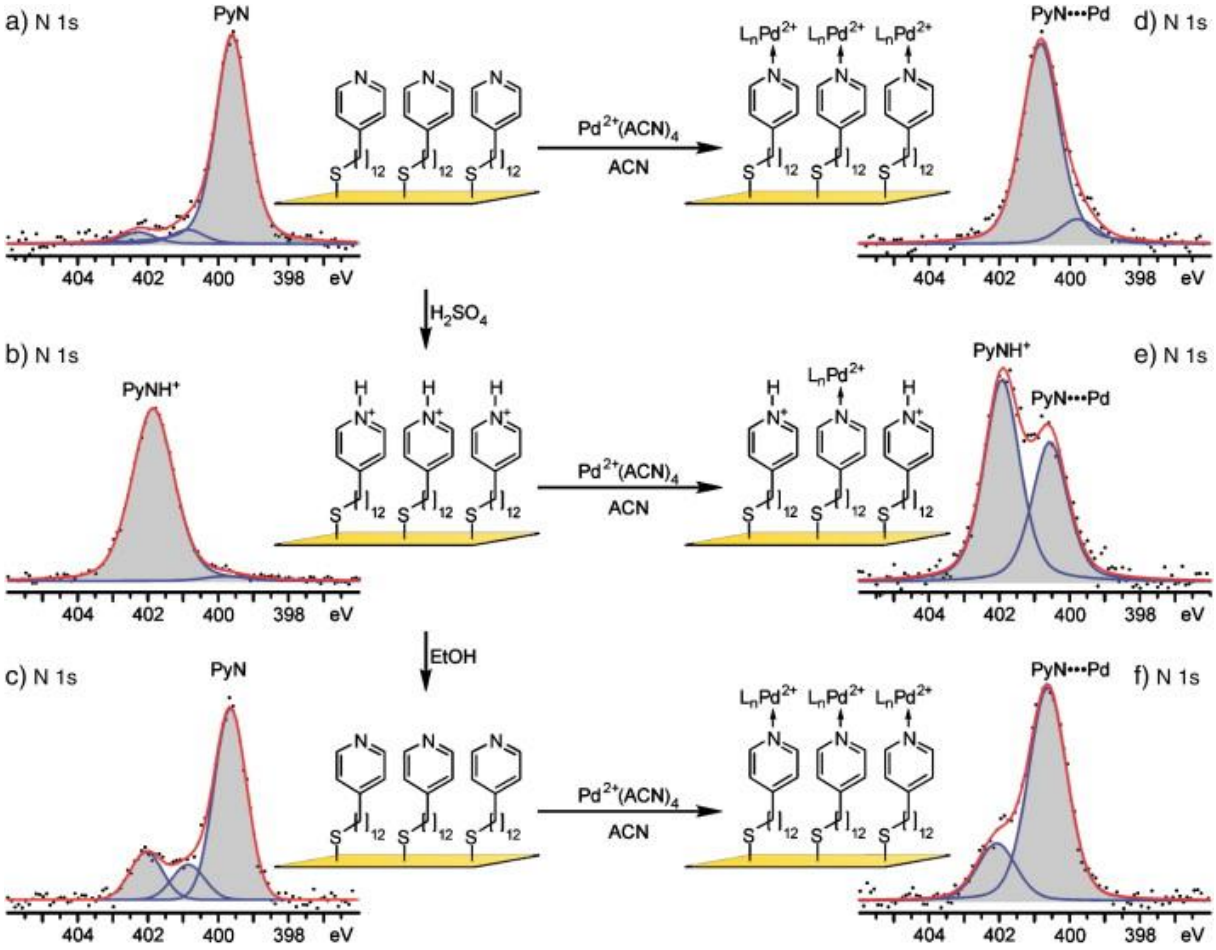

Figure 41. N 1s core level spectra of a pyridine-terminated SAM in different states: a) pristine, b) protonated with H_2SO_4, c) protonated with H_2SO_4 and deprotonated with EtOH, d) Pd(II)-coordinated, e) Pd(II)-coordinated after protonation, f) Pd(II)-coordinated after a complete protonation/deprotonation cycle obtained by Al Kα excitation laboratory XPS at 60° emission angle. Reprinted from J. Poppenberg, S. Richter, E. Darlatt, C. H.-H. Traulsen, H. Min, W. E. S. Unger, C. A. Schalley, *Surf. Sci.* 2012, *606*, 367-377, Copyright (2012), with permission from Elsevier.

The protonation and deprotonation of the terminal pyridine with sulfuric acid proves this process to be a reversible cycle without serious damage of the SAM, demonstrating stability of the monolayer. Furthermore, the study showed that the protonation acts as competitor to metal deposition to the monolayer as most pyridyl nitrogens are occupied by protons. This reduces the binding sites.

Table 2. Binding energies (BE), relative intensities and FWHM values of the detected components (PyN, PyN···Pd, PyNH+) in the N 1s core level spectra of PDT SAMs before and after palladium coordination.

sample	PyN		PyN-H+		PyN-Pd		FHWM
	BE (eV)	area%	BE (eV)	area%	BE (eV)	area%	
pristine SAM	399.7	86	402.3	7	--	--	1.1
protonated SAM	399.8	3	401.9	97	--	--	1.4
deprotonated SAM	399.7	69	402.1	18	--	--	1.1
pristine SAM after Pd-coordination	399.7	3	--	--	400.8	97	1.2
protonated SAM after Pd-coordination	399.8	--	401.9	59	400.6	41	1.2
deprotonated SAM after Pd-coordination	399.7	--	402.2	21	400.7	79	1.3

Table 2 summarizes the occurring nitrogen peaks for the different monolayers and shows their peak area ratios in the spectra.

Zharnikov *et al.*[104] used XPS in a study of the bottom-up assembly of multicomponent coordination oligomers or in other words multicomponent metal-organic multilayers. First, the underlying template layer, which was assembled in a two-step process, was analyzed. As already shown before (see chapter 3.4.4, Figure 26), silicon surfaces were functionalized with (4-chloromethyl-phenyl)-silane and subsequently modified with the Ru-diterpyridine complex. This could be confirmed by clearly identifying the signals of Ru $3d_{3/2}$ in the C 1s spectrum (a) and pyridine nitrogen at 400.4 eV in the N 1s spectrum (b) shown in Figure 42. They could also confirm the formation of the multilayer by XPS. Especially, the N 1s spectrum shown in Figure 42c exhibits characteristic emissions for both the Ru-coordinated terpyridine-nitrogen (assigned as N) at 400.3 eV and the Cu-coordinated pyridine-nitrogen (N*) at 402.8 eV plus pronounced peak at 406.2 eV for NO_3 (NO_2^-) of copper nitrate. Additionally, the spectra of the $AgNO_3$ and the $CuNO_3$ terminated multilayers showed the expected signals for Ag 3d (d) and Cu 2p (e) respectively.

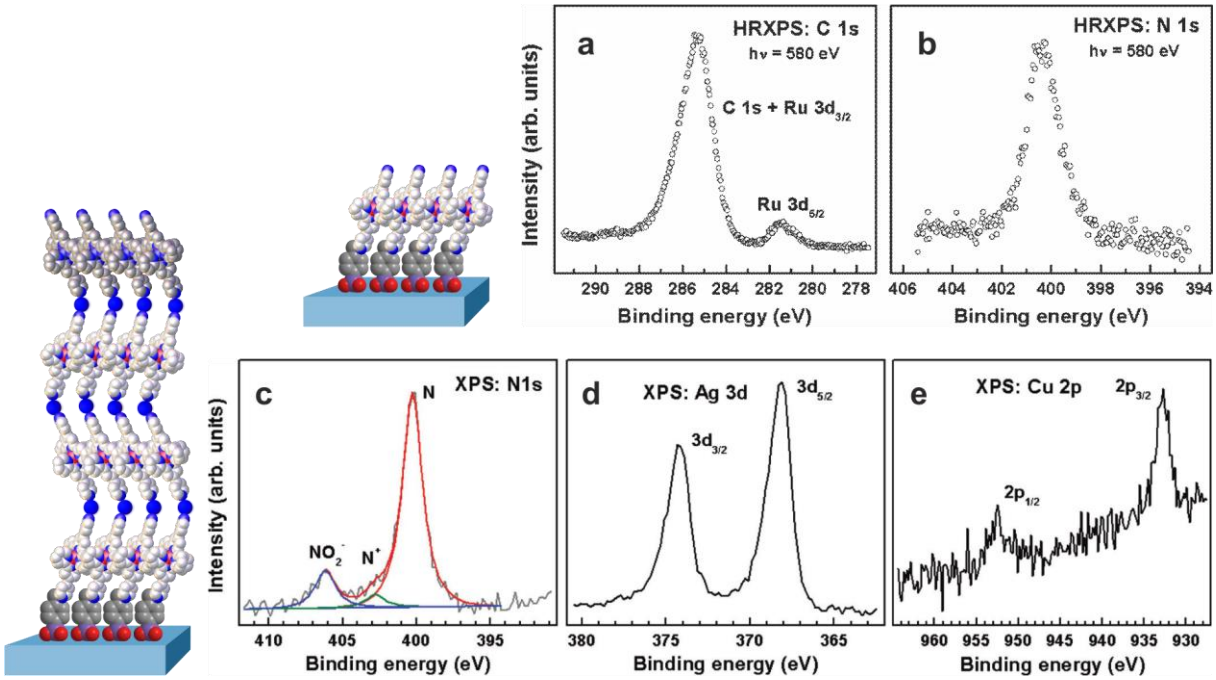

Figure 42. (a) C1s/Ru3d and (b) N1s XPS spectra of the template layer 1 acquired at the synchrotron BESSY II. Some of the characteristic peaks are marked. The Ru $3d_{3/2}$ peak is merged with the C 1s emission. (c) The N1s XPS spectrum (Mg K_α irradiation) of metallo-ligand 1-terminated Cu-based oligomer film, along with the (d) Ag 3d spectrum of the $AgNO_3$ terminated oligomer film, and (e) the Cu 2p spectrum of the $Cu(NO_3)_2$ terminated oligomer film. Reprinted and adapted with permission from P. C. Mondal, J. Yekkoni Lakshmanan, H. Hamoudi, M. Zharnikov, T. Gupta, *J. Phys. Chem. C* 2011, *115*, 16398-16404. Copyright 2011 American Chemical Society.

3.5.3. Near-Edge X-Ray Absorption Fine Structure (NEXAFS)

To obtain more information about adsorbate systems on surfaces, X-ray absorption spectroscopy (XAS) can be utilized. The particular variant of X-ray absorption spectroscopy to be discussed here – near-edge X-ray absorption fine structure spectroscopy (NEXAFS) – was devised in the 1980s. The technique, which can also be referred to as X-ray absorption near edge structure (XANES), was developed in order to provide information on the electronic structure and conformation of molecules bound to solid surfaces, mostly that of metals. When it comes to determining the chemical nature and the orientation of the molecular species on a solid substrate, the most important method is infrared (IRRAS) spectroscopy. But considering sensitivity, NEXAFS is far more applicable as IR applied to metal surfaces only completely detects vibrations with a transition dipole moment perpendicular to the surface, leading to the surface selection rule.[120]

Similar to XP spectroscopy, the photoelectric effect acts as the fundamental basis of XAS. However, this type of synchrotron-based photoelectron spectroscopy needs a continuous incident photon energy. This leads to the disadvantage that it cannot be used in a connection to a laboratory X-ray source that has a fixed photon energy. This technique requires a high performance synchrotron source that provides the needed polarized, monochromatic light. Major

research facilities such as BESSY II (abbreviation for ***B**erliner **E**lektronen**S**peicherring-Gesellschaft für **Sy**nchroton-strahlung*) in Berlin-Adlershof provide such synchrotrons. Here, electrons are vigorously accelerated through a linear accelerator and then forced by strong magnetic fields into a circular orbit. This leads to the release of a lot of their energy in form of electromagnetic radiation that is available on a wide energetic window, from infrared via the UV and visible range through to (hard) X-ray radiation.

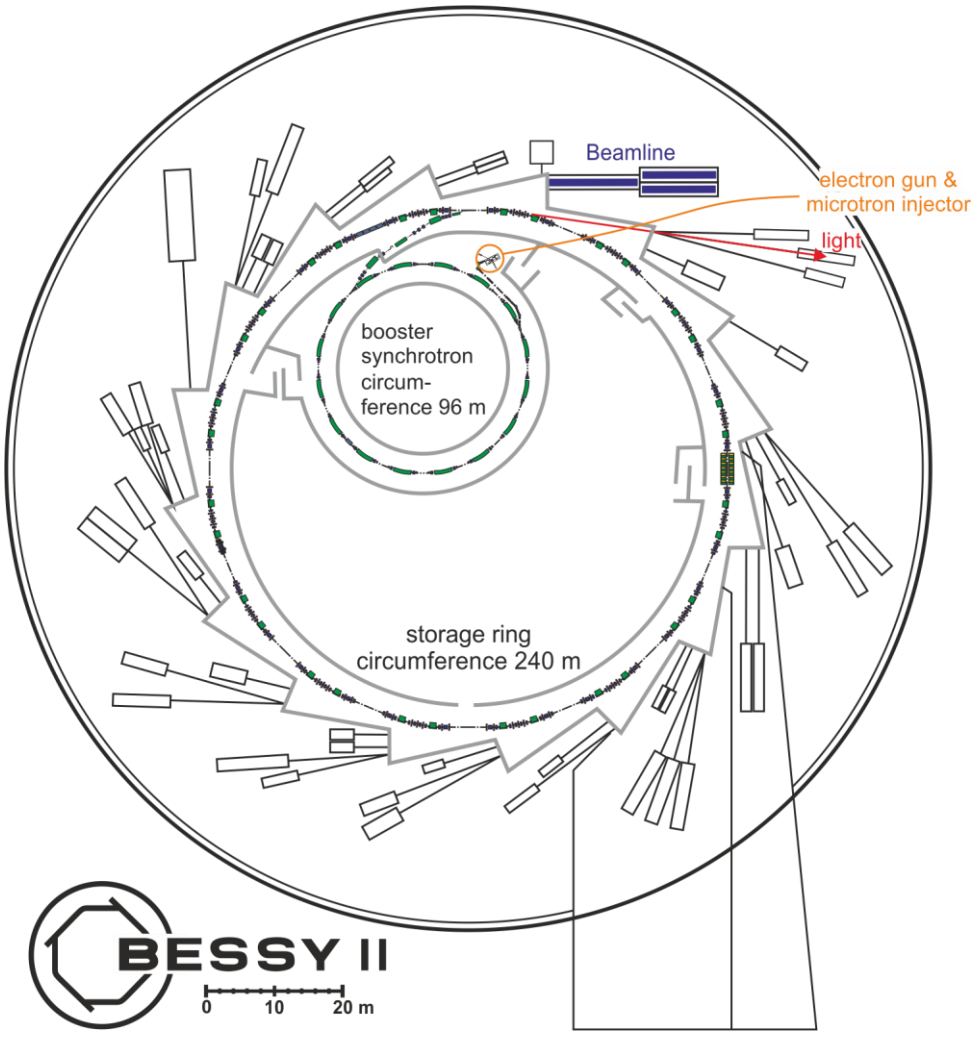

Figure 43. Schematic illustration of the synchrotron at BESSY II.[129]

Figure 43 shows a schematic picture of the electron storage ring BESSY II. Starting from a hot cathode (70 kV acceleration voltage), electrons are pre-accelerated in a microtron and subsequently injected into the synchrotron ring where the electrons will be further accelerated up to 1.7 GeV followed by their injection to the storage ring, in which the electrons packages achieve a life time of about 8 hours. The quantity of electrons in the storage ring corresponds to a current of 300 mA. Due to the extremely high acceleration voltage, the orbiting electrons reach nearly the speed of light (v(electrons@BESSY) = 299792.44 km*s^{-1}, in comparison: v(light) =

299792.458 km*s^{-1}). In the storage ring, the electrons are kept on track by large dipoles with installed quadrupole and sextupoles in order to keep the electron beam stable over a longer period of time. The emitted radiation is linearly polarized in the plane of the ring – above and under this level it is circularly polarized. During an XAS experiment, the radiation is directed by so called beamlines onto the sample of interest inside of the analysis chamber.

As already mentioned, Auger-electrons and/or fluorescence photons are emitted from the atom/molecule when core electrons are excited by X-ray irradiation and the remaining hole is filled with higher shell electrons (see chapter 3.5.2, Figure 37). For the detection of the fluorescence, the fluorescence yield is applied which has an informational depth of a few µm. Therefore, it is not applicable for systems generated in this work and will not be discussed in detail. For the detection of the secondary electrons, some things have to be considered: During their travel through the solid, the excited or secondary electrons experience inelastic scattering to some extent, which leads to single, as well as multiple scattering processes (back scattering). Therefore, the electrons emitted from the surface have different kinetic energies (E_{kin}(Auger) ≥ E_{kin}(electrons)) but can still subsequently be detected. The more electrons are emitted from the surface the higher is the absorption of photons by the surface-attached architecture. Two principal techniques exist for detection of the electron emission: First, the detection of every single emitted electron is possible (total electron yield, TEY) and second by applying a certain retardation voltage, electrons with a lower energy are retarded so that they do not reach the collector (partial electron yield, PEY). Compared to the TEY, the PEY has shown to create much more reproducible results due to an enhanced signal-to-noise ratio and also provides an enhanced surface sensitivity. Therefore, a PEY-detector is used for all experiments published in this work.

Depending on the spectral region that is measured, there is a distinction in the field of X-ray absorption spectroscopy between near-edge X-ray absorption fine structure (NEXAFS) and extended x-ray absorption fine structure (EXAFS). A NEXAFS spectrum reflects the dependence of the photo absorption cross-section on the photon energy for values from just below the core level ionization threshold up to around 50 eV above. With EXAFS, the electronic structure far above this threshold is investigated (see Figure 44).

The shown step is caused by the excitation of core electrons by X-ray photons that at least have to have the same energy as the binding energy of the electrons to excite them into both the vacuum continuum or the unoccupied valence and Rydberg states. When this energy is reached, a sudden increase in absorption of photons - the X-ray absorption edge - is observed. This edge resembles the energy of the ionization potential (IP, vacuum level) of the system.

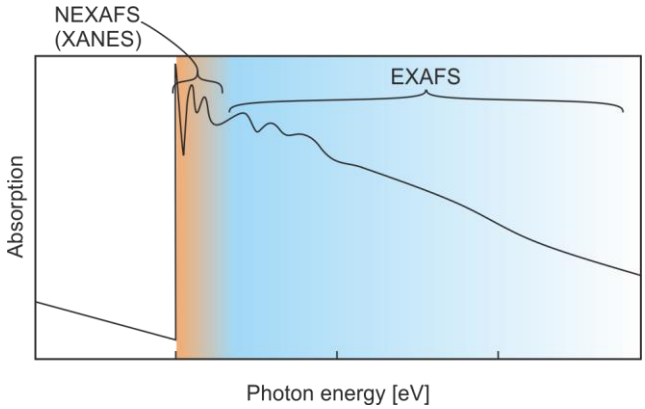

Figure 44. Illustration of the X-ray absorption of a molecular surface-assembly and the areas of XAS.

A typical NEXAFS experimental setup needs a monochromator in order to transmit only light with predefined energy to the sample. The shape of the beam is defined by a set of horizontal and vertical slits. A gold grid (typical transmittance 85%) is placed in the optical path making it possible to monitor the intensity (I_0) of the X-ray photon beam incident on the sample. This is mainly done with highly oriented pyrolytic graphite (HOPG) to calibrate the energy scale. The X-ray beam then enters the analysis chamber and hits the sample that is mounted on a special manipulator to control the sample orientation with respect to the incident beam (polar as well as in azimuthal angles). The detector is positioned close to the sample and also should have an as wide as possible acceptance angle in order to guarantee a good signal-to-noise ratio. Further features of the used detector are explained elsewhere.[120]

The excitations from the core orbitals either into the continuum or in unoccupied molecular or Rydberg orbitals provide the crucial contributions to a NEXAFS spectrum that is therefore composed of the element-characteristic X-ray edge and a superimposing fine-structure. The absorption behavior upon monochromatic scanning of the photon energy around the ionization energy gives detailed insights into the electronic structure of the adsorbed molecules. For a simplified case of a core level electron and in the absence of any other unoccupied electronic states, the spectrum would resemble a step function (Figure 45 right, the dashed purple line). No absorption would take place below the core electron binding energy (IP). However, beyond this threshold a transition of the electron from the core level to the continuum would lead to a sudden increase of photon absorption. This gets significantly more complicated already for a free single atom due electrostatic potential of the positively charged nucleus leading to a significantly higher number of electronic states – below (bound states) and above (unbound states) of the ionization potential. The bound state excitations either occur into valence states at lower energies in vicinity of the core (Figure 45, green) or into Rydberg states (Figure 45, blue) that converge to the vacuum level and give sharp resonances. However, the transitions into unbound states that identify with a (molecular) antibonding state have signals located well

above the ionization threshold with a large energetic half-width. In other words, theses transitions give broad signals in the NEXAFS-spectrum due to their short life time.

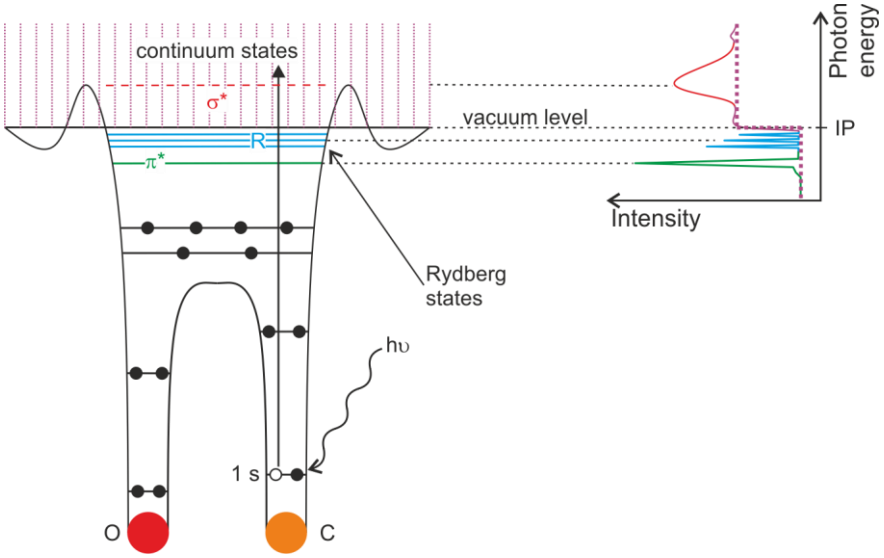

Figure 45. Electronic transitions in a two-atomic molecule (CO) at the X-ray edge and their contribution to a NEXAFS-spectrum.[120]

The resulting spectral features are well explained and understandable for the case of a diatomic molecule, which is shown in Figure 45. The effective electrostatic potential and the corresponding K-edge spectrum are also shown. Around the ionization threshold, resonant transitions are superimposed on the step-like absorption edge as shown in Figure 45, right. The unsaturated π-bonds in the C-K edge correspond to electronic transition from the C 1s core-shell into the unoccupied π* molecular orbitals. In this case resonances at a photon energy of ~285 eV are observed. Of course, these so-called π-resonances can only be observed for molecules with π-bonding, i.e. double and triple bonds or aromatic systems and not for single bonds. The anti-bonding σ* orbitals that lie well above the vacuum level show signals at higher energies than that of the absorption edge. In the energy area between these two transitions, the excitations into the Rydberg-orbitals additionally occur that are however sometimes indistinguishable from other transitions. In CH single bonds for example, a mixing between the Rydberg- and the hydrogen-derived antibonding orbitals with the same symmetry leads to hybridization and therefore to their superimposition. The measured width of a resonance is then a result of the resolution of the instrument (leading to a Gaussian line shape), the life time of the excited state (leading to a Lorentzian line shape), and the vibrational motion of the molecule that results in an unsymmetrical broadening;[120, 130] as a rule of thumb, the higher the resonance lies in the continuum the larger is its line-width.

Besides the information about the electronic structure of a surface-bound molecule or molecular fragment, NEXAFS provides data about their conformational nature and therefore helps

to determine a preferential orientation of molecules or certain functional groups relative to the surface due to an effect called linear dichroism. It describes the anisotropic (directionally dependent) absorption of linearly polarized light by the highly directional bonds or their corresponding molecular orbitals. According to that, the absorption intensity of linear polarized light by an electron excitation depends on the overlap between the electronic transition dipole moment (TDM) and the electric field-vector (**E**) of the incident light which is perpendicular to the direction of the photons. Therefore, the intensity is also dependent on the angle the light hits the surface. The mathematical background is provided by Fermi's golden rule, which describes the dependence of the absorption intensity (**I**) on the vector product of the polarized light electric field-vector with the TDM of unoccupied orbitals.[131]

$$\boldsymbol{I} \propto \boldsymbol{P_{i,f}} \propto |\langle \boldsymbol{f}|\boldsymbol{E}\cdot\boldsymbol{TDM}|\boldsymbol{i}\rangle|$$

Equation 3. Fermi's golden rule. I = absorption intensity, $P_{i,f}$ = transition probability, f = final state, I = initial state, E = electric field-vector, TDM = transition dipole moment.

To show a preferential orientation by showing a linear dichroism, multiple measurements at different angles – sample to incident light – are required.

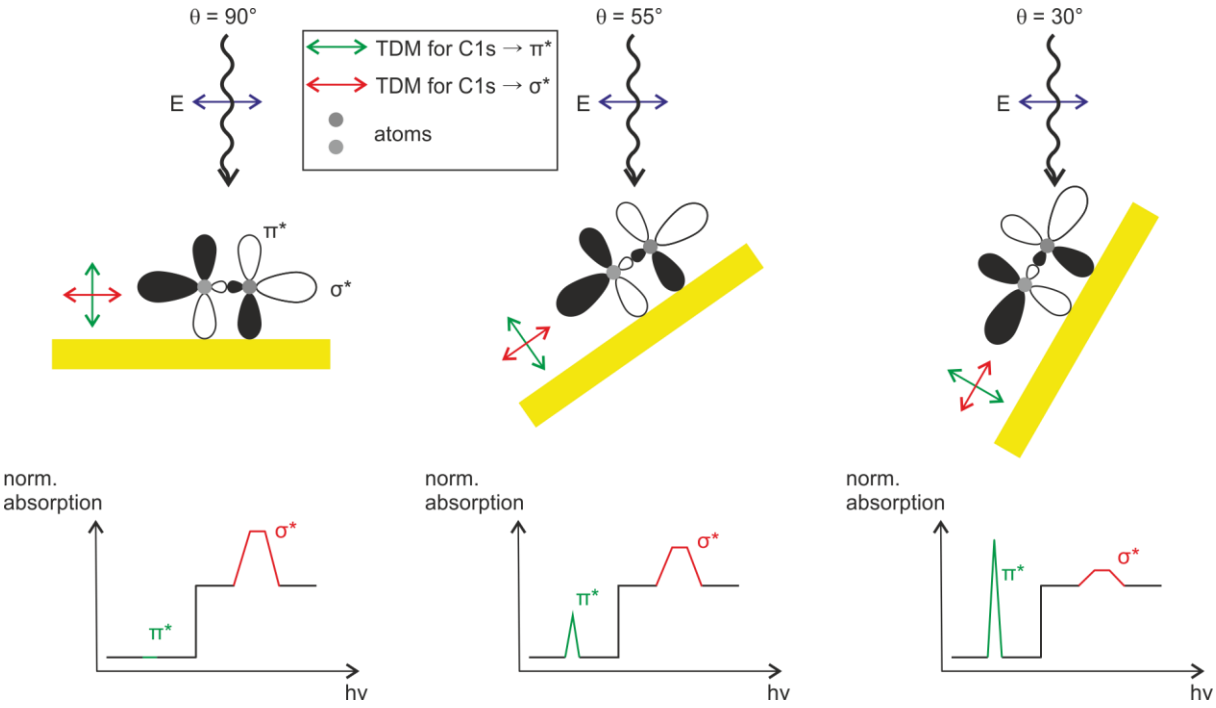

Figure 46. Illustrating the behavior of the π*- and σ* absorption intensities in dependence of their angle to the incident light.[127d]

A gedanken experiment helps to clarify this effect: In Figure 46, a diatomic molecule with a π-bond that lies flat on a substrate is considered. While the transition dipole moment of the π*-orbital is perpendicular to the bond and surface, the TDM of the σ*-orbital lies parallel to the

bond and surface. When the incident light hits the surface with an angle of 90°, the field vector **E** completely overlaps with the TDM of the σ* molecular orbital (MO) and not at all with the one of the π*-MO. This leads to the observation that the absorption intensity of the σ*-transition is very strong while the π*-band completely vanishes. By reducing the angle of the incident light, the absorption intensity of the π*-transition increases and the one of the σ*-transition decreases.

In two quite recent studies, the Schalley group has shown how NEXAFS can be used (together with XPS) to show on one hand the composition and conformational structure of a monolayer that is deposited on the surface and on the other hand how a template influences the orientation of the subsequently deposited layer.

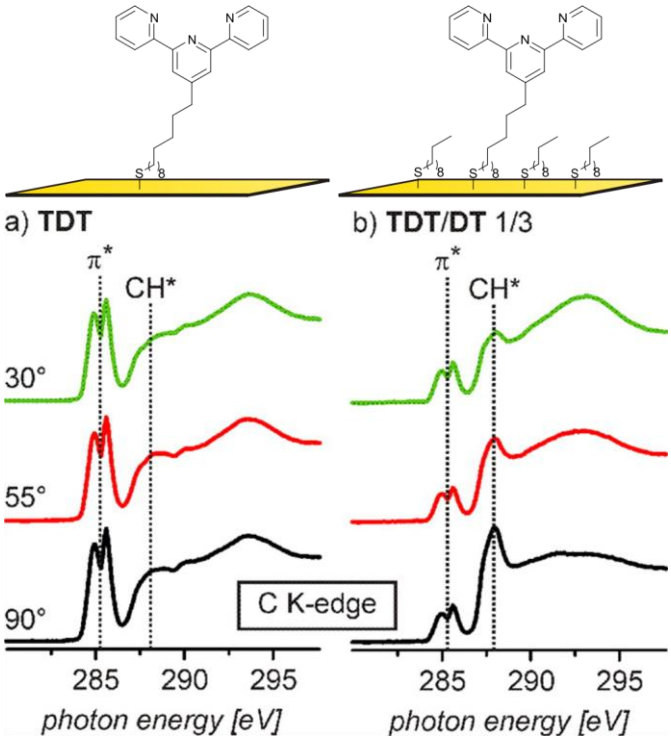

Figure 47. Angle-resolved C K-edge NEXAFS spectra (in units of normalized PEY [au]) of (a) 1:0- and (b) 1:3-(TDT/DT)-SAMs. The π* resonance shows the expected peak splitting that is characteristic for the pyridine-carbons. Reprinted with permission from C. H.-H. Traulsen, E. Darlatt, S. Richter, J. Poppenberg, S. Hoof, W. E. S. Unger, C. A. Schalley, *Langmuir* 2012, *28*, 10755-10763. Copyright 2012 American Chemical Society.

First, the group has developed binary terpyridine-terminated monolayers with different molar solution-ratios that comprises of 12-(2,2′:6′,2″-terpyridine-4′-yl)dodecane-1-thiol (**TDT**) and 1-decanethiol (**DT**) that are shown in Figure 47.[66] In an interplay of XPS and NEXAFS, they could observe that the composition of the (**TDT**/**DT**)-SAMs and with it the surface density of terpyridyl groups correlates linearly with the relative concentrations of the two compounds in the solution used for depositing them. However, the amount of terpyridine-coordinated Pd^{II}

ions does not follow this trend and has a peak at a 1:3 ratio of **TDT**/**DT**. As this indicates a major fraction of the terpyridines in **TDT**-rich SAMs not to be accessible for ion coordination, NEXAFS spectroscopy was measured with a **TDT**-only SAM as well as the supposedly best ratio SAM of 1:3 for an explanation. Both SAMs exhibit resonances for the excitation into π* orbitals at photon energies of 284.9 and 285.6 eV which correspond to the terpyridyl moiety. They also show the electron transition into the CH* orbital at 288.0 eV. However, the CH* resonance of the aliphatic backbone in the monomolecular SAM does not increase from a 30° to a 90° incident light angle with respect to the surface plane. This indicates that there is no order present in this moiety. The 1:3-ratio **TDT**/**DT** SAM shows a different picture: The CH* transition exhibits a distinctive linear dichroism that suggests an upright orientation of the aliphatic chains of both the **TDT** as well as the **DT**. In both cases, the terminal terpyridines of the SAMs do not show a preferential orientation as there is no linear dichroism present. In conclusion, a large fraction of the monomolecular SAM exhibits backfolding and therefore the terpyridines are not accessible for Pd^{II}-coordination. The missing preferential orientation in terpyridines for the mixed SAM however indicates a certain flexibility of the terminal groups. The fact that more Pd^{II} ions can be deposited on the optimized SAM than on a pure **TDT**-SAM also supports the assumption that intermixed phases are formed.

In a second study,[132] the group studied the directional effects on an organic adlayer of macrocycles and rotaxanes that occur when different template layers (SAMs) show different properties in orientation as well as flexibility. For the monolayer of (E)-4-pyridine-4-yl)stilbenethiol (**PST**) introduced in this study, angle-resolved N K-edge and C K-edge NEXFAS revealed a linear dichroism for the π*-transition which gives evidence for a preferentially oriented monolayer. The preferential orientation of the terminating pyridines, however, lies in marked contrast to the flexibility of the pyridines in the **PDT** monolayer.[65] After the metal-mediated self-assembly of the macrocycle and rotaxane onto both of the templating monolayers, the adlayers were compared with respect to density as well as orientation. In terms of density, the **PST** SAM with a rigid pyridine template showed a higher coverage of macrocycles and rotaxanes as shown by ToF-SIMS. In terms of orientation, the results showed the rotaxane to be ordered after deposition onto both of the monolayers. The macrocycle, however, only exhibits a preferential orientation when deposited onto the **PST** template. The intensity change upon angle change in the π* resonances remains more or less constant before and after the deposition of the macrocycle which indicates that the preferential orientation of the **PST** is not affected by the macrocycle layer. Yet, the shape of the signal changes upon angle change as it is clearly visible in Figure 48a. The deposition of the macrocycle onto the **PDT** SAM delivered different results (Figure 48b): The intensity ratio does not change at different angels of incidence. These qualitative observation of the intensity-ratio behavior upon angle change is then confirmed by fitting the two signals and plotting the change of the peak area ratio C2/C1 (C1: intensity of the

peak at 285.1 eV, C2: intensity of the peak at 285.4 eV) over the angle of incidence shown in Figure 48c.

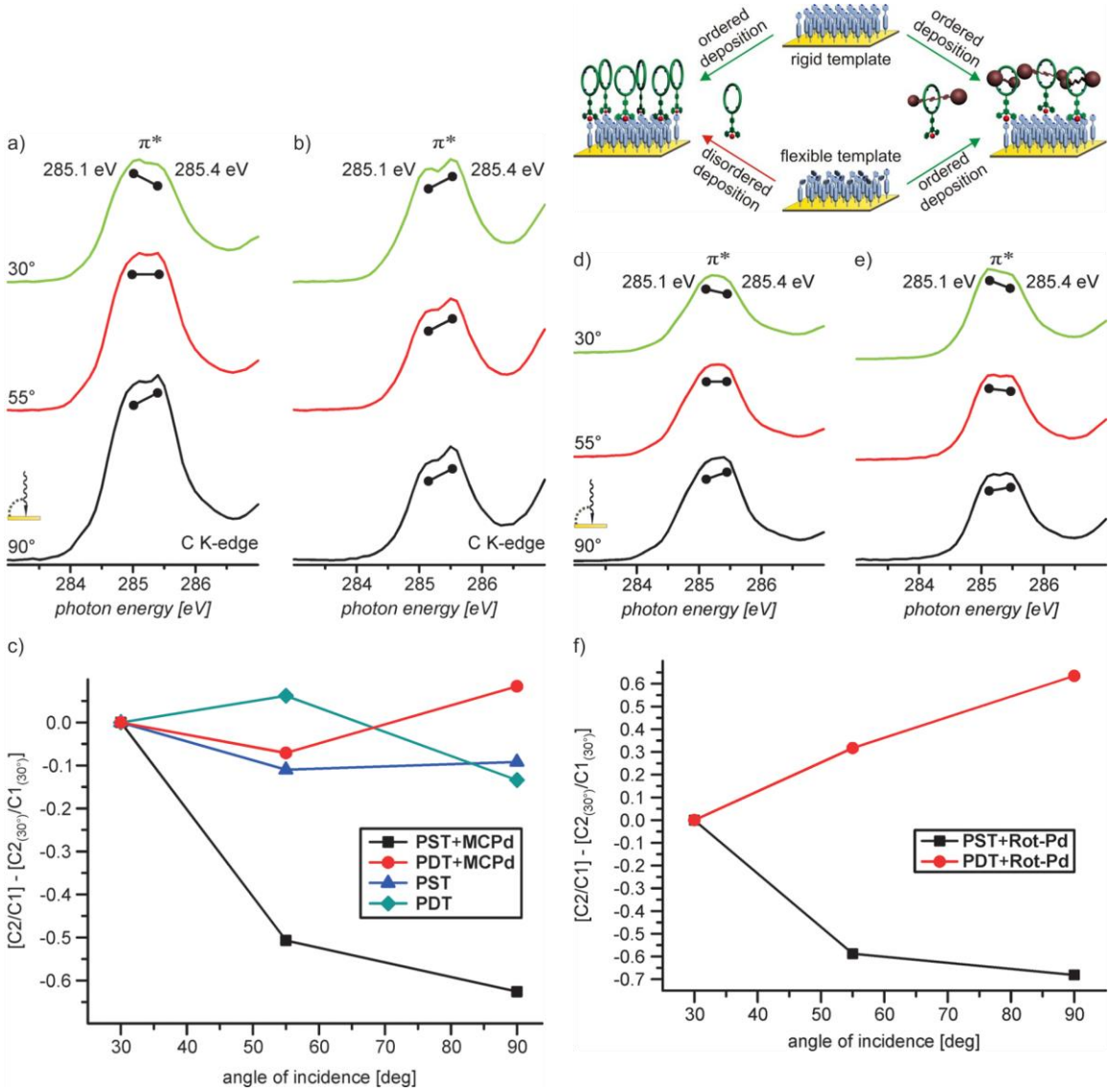

Figure 48. Top: Angle-resolved NEXAFS C K-edge spectra of the π* regions of the macrocycle coordinated to (a) PST and (b) PDT, and the rotaxane coordinated to (d) PST and (e) PDT. Bottom: differences of C2/C1 peak area ratios of the depicted π* resonances at different incident angles of synchrotron light for (c) PST, PDT, PST+Pd-MC, PDT+Pd-MC; and (f) PST+Pd-Rot as well as PDT+Pd-Rot. Reprinted and adapted with permission from S. Richter, J. Poppenberg, C. H.-H. Traulsen, E. Darlatt, A. Sokolowski, D. Sattler, W. E. S. Unger, C. A. Schalley, *J. Am. Chem. Soc.* 2012, *134*, 16289-16297. Copyright 2012 American Chemical Society.

The same analysis was carried out with the rotaxane layers (Figure 48d-f). A small but clearly detectable linear dichroism is observed for the rotaxane layer on both **PST** (d) and on **PDT** (e). This is again demonstrated more clearly by the change in the peak area ratio C2/C1 using different angles of incidence (Figure 48f). Like the macrocycles, the rotaxane wheels are ori-

ented preferentially upright. In contrast to the macrocycles, the rotaxanes obviously pack sufficiently well through lateral interactions on both SAMs to yield ordered arrays irrespective of the template's backbone rigidity and the flexibility of the terminal SAM pyridine groups. In conclusion, for efficient lateral interactions and a preferential orientation, rather densely packed layers are required.

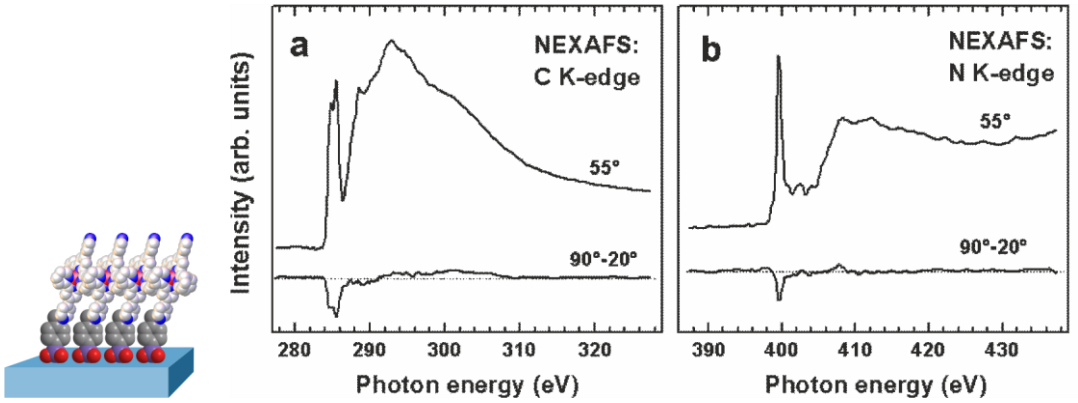

Figure 49. (a) C and (b) N K-edge NEXAFS spectra of the template layer immobilized on functionalized silicon substrate. Reprinted and adapted with permission from P. C. Mondal, J. Yekkoni Lakshmanan, H. Hamoudi, M. Zharnikov, T. Gupta, *J. Phys. Chem. C* 2011, *115*, 16398-16404. Copyright 2011 American Chemical Society.

Zharnikov *et al.* also analyzed their template layer (see chapters 3.4.4 and 3.5.2) with NEXFAS spectroscopy that confirmed the results from XPS of slightly tilted molecules in the monolayer.[104] As it is clearly visible in Figure 49, both C and N K-edge spectra exhibit characteristic resonances that can be assigned to pyridine. Like in the cases discussed above, the C K-edge spectrum exhibits a pronounced doublet in the π* region at ~285 eV and the N K-edge spectrum features a strong π* signal at ~400 eV. Furthermore, the signals in both NEXAFS spectra show a clear and pronounced linear dichroism. This proofs a preferential orientation and is illustrated by the differences between the spectra acquired at 90° and 20°. By using a standard theoretical framework[131], the group could estimate the angle of the molecular backbone to the surface normal to be ~41°. This value could be, however, overestimated because the different torsions of the aromatics in the molecule prevent a larger effect and therefore the tilt appears to larger than in reality.

3.5.4. Time-of-Flight Secondary Ion Mass Spectrometry (ToF-SIMS)

So far, the surface composition could be quantified by XP-spectroscopy, NEXAFS-analyses delivered an insight into the preferential orientation and UV/Vis-spectroscopy showed the presence of different structure elements. For a complete surface analysis, more sophisticated methods such as secondary ion mass spectrometry (SIMS) play a crucial role. It can find tiny

quantities of molecular entities on the surface by analyzing characteristic molecule or fragment ions which are generated by bombarding the sample with a primary ion beam.

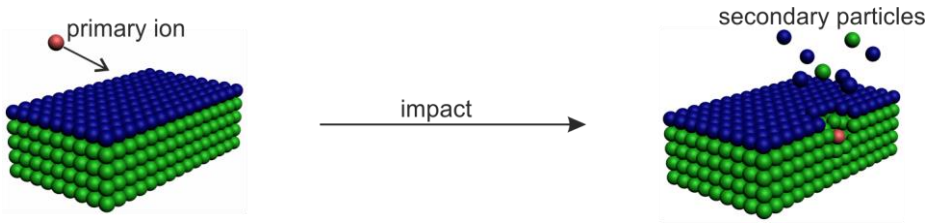

Figure 50. Ionization process during a Tof-SIMS experiment.

In the process of shooting primary ions to the sample, energy is transferred to the molecules or atoms on the surface by elastic scattering collision processes. A cascade of collision emerges between the surface molecules, which leads to the emission of ionized molecules, fragments and atoms from the surface lattice. ToF-SIMS uses a focused, pulsed particle beam to dislodge chemical species on a materials surface. Besides the energy of the primary ions, the fragmentation pattern also depends on the location of the molecules and the material they are embedded in. Particles produced closer to the site of impact tend to be dissociated ions (positive or negative). Secondary particles generated farther from the impact site tend to be molecular compounds, typically fragments of much larger organic (macro-)molecules. To prevent multiple bombardment of the same region on the surface and therefore a gradual disintegration of the surface, the primary ion density is substantially reduced so that, statistically, the same surface region is hit just once by a primary ion. This method is called static-SIMS and is used for the investigation of macrocycle multilayers and rotaxanes as it has delivered reliable results for similar systems.[133]

The principle setup of a ToF-SIMS experiment is depicted in Figure 51. First, an ultra-high vacuum system is required to increase the mean free path of the generated secondary ions and therefore enable them to enter the mass analyzer. The primary ions, which can be atomic (e.g. Cs^+ or Ga^+) or cluster-like (e.g. Bi_3^+, Bi_2^{3+}), are generated in the primary ion source, emitted in very short pulses and then focused to the sample. The pulsing is applied because a non-continuous flight time analysis shall be conducted. Secondary ions are captured by the electric field of the extractor and equally accelerated independently of their mass by an applied potential. In the present case, the flight path of the ions has a linear design using a reflective ion mirror. The detection of ions by means of time-of-flight is based on the principle that ions with variable weights fly at different speeds when they are accelerated with the same kinetic energy. Thus, they arrive at different times at the detector and their mass-to-charge ratio can then be determined on the basis of their time of flight with a simple relationship. The ion mirrors are used, as that enables a better separation of the ions by enlarging the flight distance and thus

a higher resolution of the spectrum is possible. The electron flood gun is used for charge neutralization as sample charging can lead to spectra that do not give the real picture.

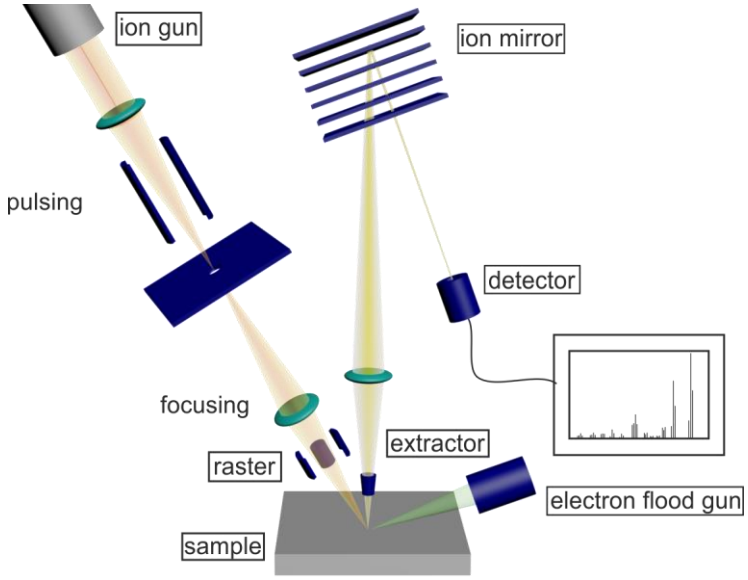

Figure 51. Schematic representation of the experimental setup of a ToF-SIMS measurement.

There are numerous advantages, which make ToF-SIMS a highly applicable method for surface analysis. It is highly sensitive for trace elements or compounds down to the ppm range, makes elemental as well as chemical mapping on a sub-micron scale possible,[134] the analysis is non-destructive in the static mode, conducting as well as insulating samples can be analyzed, and depth-profiling in the near surface environment can be conducted. However, it has also a small number of limitations: Generally, it does not produce quantitative analyses, optical capabilities are typically limited, making it difficult to find regions of interest, and even for very simple systems very complex spectra are generated, which makes an analysis of multilayers especially of large and complex (supra-)molecules difficult. Therefore, Principal Component Analysis (PCA) can be used for a better understanding of the big resulting data.

PCA is a statistical procedure that uses an orthogonal transformation to convert a set of possibly correlated variables into a set of values of linearly uncorrelated variables called principal components. In other words, PCA can identify the major directions of variation in a given dataset. A dataset is defined as a matrix where the rows contain samples and columns contain variables. In the case of ToF-SIMS data, samples are the mass spectra and the variables are the individual m/z ratios. The PCA is calculated from the covariance matrix of this original data set. It is an axis rotation that aligns a new set of axes, called principal components (PCs) with the maximal directions of variance within a dataset. PCA creates three new matrices, containing the scores, the loadings, and the residuals. Its purpose is to structure, simplify and illustrate

extensive data. The analysis of surfaces with ToF-SIMS is greatly simplified by this method especially regarding the analysis of biomolecules.[135]

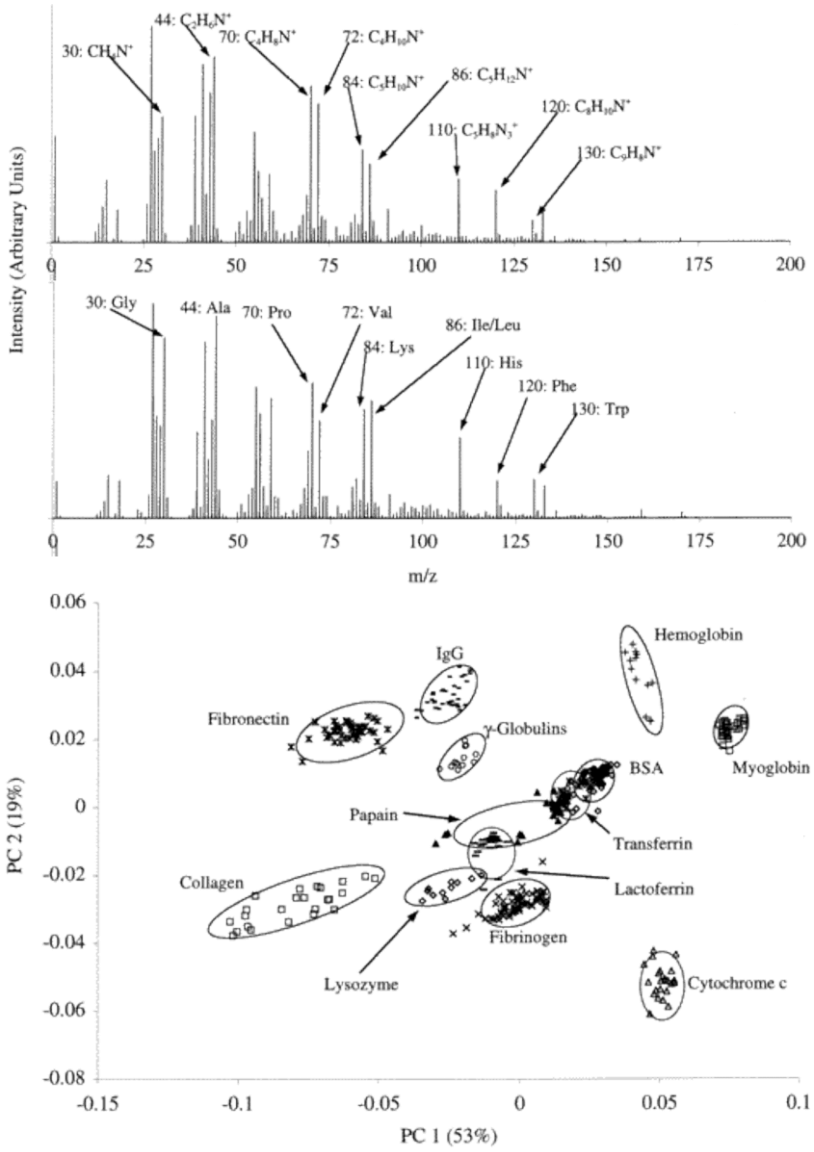

Figure 52. Top: Comparison of the ToF-SIMS spectra of bovine hemoglobin and horse heart myoglobin adsorbed onto mica from a 100 µg/mL single component protein solution. Bottom: Scores plot from PCA of the positive ion spectra of proteins adsorbed onto mica from 100 íg/mL single component protein solutions. Note the excellent separation of several of the protein spectra shown in this figure. Reprinted and adapted with permission from M. S. Wagner, D. G. Castner, *Langmuir* 2001, 17, 4649-4660. Copyright 2012 American Chemical Society.

For example, the distinction of different proteins adsorbed to the surface can be extremely enhanced by the usage of PCA when ToF-SIMS is applied. ToF-SIMS can be a powerful method for the characterization of adsorbed proteins on biomaterial surfaces due to its chemical specificity and surface sensitivity. However, the SIMS fragmentation patterns for proteins are quite complex due to the heterogeneity of the protein sequence. Therefore, PCA is excessively used to obtain a more detailed interpretation of the protein SIMS spectra. Typically, a

fewer number of orthogonal principal components than the original variables (SIMS peaks), that are in fact correlated, is needed to conceive the essential information in a particular data set.

The work of David Castner and coworkers can be taken as an example.[136] Figure 52 shows how PCA can simplify the analysis of different molecular assemblies with similar spectra. The top half shows two SIMS spectra in positive ion mode of two different compounds adsorbed on mica that are almost identical apart from some differences in signal intensity. Similar spectra are obtained when ToF-SIMS is applied to other proteins adsorbed to the surface. If PCA is now used, the data get somewhat easier to interpret. Even if a large number of different proteins with a large number of data points are investigated, the protein spectra can easily be distinguished from each other.

The imaging capabilities of ToF-SIMS can provide elemental and molecular information from defects and particles on the micron scale. If the aim of the measurement is to obtain compositional images of the surface formed from the secondary ion spectrum with minimum possible damage to the surface, then the main problem is to ensure that sufficient signal is obtained at the desired spatial resolution whilst minimizing the ion flux incident on any part of the surface. This is most easily achieved by switching from the traditional approach of using continuous-flux ion guns to using pulsed ion sources. Additionally, ToF mass spectrometers are an efficient way of acquiring spectral data, and also provide good resolution and sensitivity up to very high masses. Using such instruments, SIMS images with a spatial resolution of down to 50 nm are obtainable.[137]

This imaging technique is especially useful for analysis of surface-patterned SAMs. The workgroup of Bart Ravoo showed how it can be applied in order to investigate the quality of the successive deposited (and orthogonal) monolayers, the resulting pattern, and their chemical composition.[138] As shown in chapter 3.4.3, they immobilized a cyclootyne oxime linker by metal-free strain-promoted azide-alkyne cycloaddition (SPAAC).[83a] The resulting azide/oxime pattern was verified by the formation of several oxygen-containing fragments like $C_2H_5O^+$, $C_7H_6NO^+$, and $C_8H_6NO_2^+$ in the positive ion mode as it is shown in Figure 53A. The generation of the aromatic ions $C_7H_7^+$, $C_7H_4N^+$, and C_7H_6NO can be attributed to the presence of the terminal benzaldoxime on the surface. The fragment $C_8H_6NO_2^+$ represents exactly the benzaldoxime with an attached carbonyl group. Moreover, the immobilization of the cyclooctyne oxime linker is indirectly visualized by the Si^+ signal. Si^+ cations are preferentially observed in the interspaces, since the thicker organic layer within the dotted structure leads to enhanced shielding of the underlying SiO_2 against the primary ion beam. Besides fluorescent microscopy, the subsequent immobilization of the biotin residue was investigated by ToF-SIMS imaging, too. In contrast to the azide/oxime-modified surface, SIMS analysis of the same surface after

reaction with biotin alkyne showed significant formation of sulphur containing anions such as S^-, HS^- and $^{34}S^-$ within the dotted pattern.

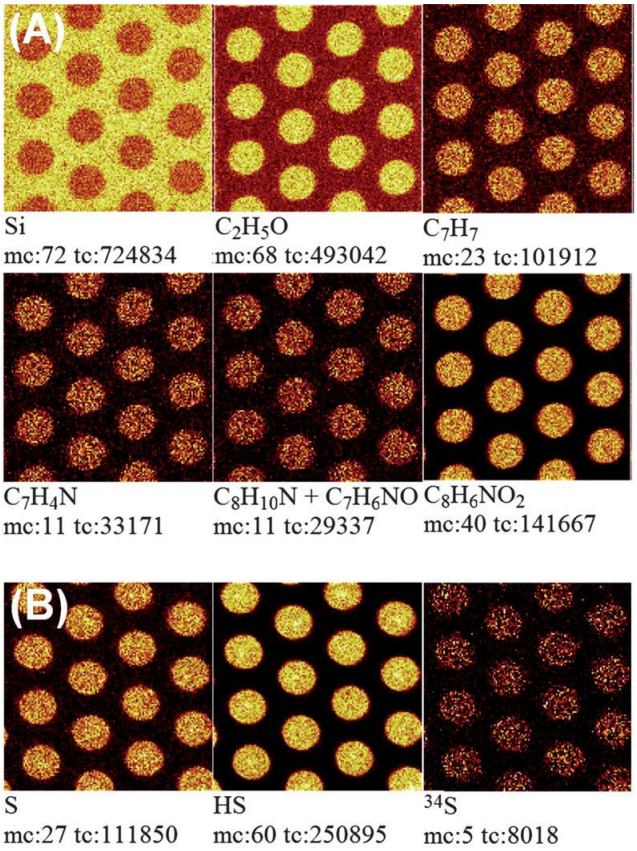

Figure 53. ToF-SIMS analysis of patterned silicon substrates. Analysis of an azide/oxime-patterned silicon substrate in the positive ion mode (A) and analysis of the surface after immobilization of biotin alyne (2) by NOAC in the negative ion mode (B) (mc: maximum counts, tc: total counts). The dots are 10 µm in diameter Reproduced from C. Wendeln, I. Singh, S. Rinnen, C. Schulz, H. F. Arlinghaus, G. A. Burley, B. J. Ravoo, *Chem. Sci.* 2012, *3*, 2479-2484 with permission from The Royal Society of Chemistry.

In a recent publication, Unger *et al.* showed that ToF-SIMS imaging can also be combined with PCA and together with scanning electron microscopy (SEM) help to analyze the degradation prcesses in duplex steels.[139]

3.5.5. Atomic Force Microscopy (AFM)

In order to have a sufficient analysis of an interface, its topographical properties have to be analyzed. Atomic force microscopy (AFM) can do that by mechanically scanning the surface and measuring the atomic forces on the nanometer scale. The technique was introduced in the late 1980s by Gerd Binnig, Calvin Quate, and Christoph Gerber[140] and can therefore be regarded as a relatively young method for surface analysis. AFM is one kind of scanning probe microscopes (SPMs) that are designed to measure local properties, such as height, friction, magnetism, with a probe. To acquire an image, the SPM raster-scans the probe over a small

area of the sample, measuring the local property simultaneously. AFMs operate by measuring force between a probe and the sample. Normally, the probe is a sharp tip, which is a 3-6 µm tall pyramid with 15-40 nm end radius that is mounted onto a cantilever. During collection of sample data, the cantilever bends dependent on the structure of the surface on the specific position due to the physical interaction of the tip with the surface. These deflections are measured and used to compile a topographic image of the surface. Microscopes have also been designed to monitor interactions due to a range of forces, including electrostatic magnetic forces.[141] The most widely used approach in commercial instruments to measure the bending of the cantilever is to adjust a laser beam to it and measure its deflections with a photo detector behind the cantilever like it is depicted in Figure 54.

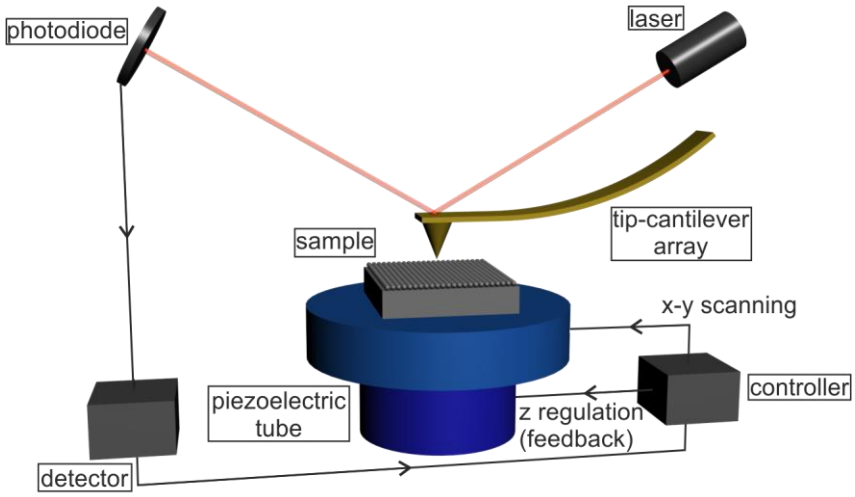

Figure 54. Schematic representation of an AFM-experiment.

However, other methods are also applied like electrical detection methods based on piezoelectric devices. The measured signal is used to control movements of a piezoelectric crystal, on which the sample (cantilever) is mounted, by a feedback system (z regulation) in order to regulate the tip-sample distance and to scan the microscope in the x,y plane.[141] The latter also being true for the methods which use the laser as measuring instrument. In contact mode, the microscope can operate in two different conditions – constant height or constant current mode. In the classical constant height mode, the needle is held at a constant height to the surface. The occurring forces corresponding to the surface structure then cause the deflection of the cantilever which is quantified by the instrument. Since the resulting forces are the higher the bigger the irregularities are, this mode is suited best for smooth as well as hard surfaces. Furthermore, the scanning speeds can reach up to ten seconds per line as no adjustments have to take place perpendicular to the surface. The so-called constant force mode, however,

is realized by manipulating the position or deflection of the cantilever with a piezoelectric element to keep the occurring force between tip and sample constant during the whole experiment. To achieve this, the deflection signal of the cantilever is fed as a control variable in to a control loop which determines the movement of the cantilever spring. Since these control loops have only a finite speed, this method is limited to lower speeds of about 3 to 4 lines per second. Although the pressure applied to the surface forces can be reduced by this approach, still a residual stress remains. In a good regulation, the information about the topography of the surface is included in the manipulated variable of the piezoelectric actuator element.

One of the main advances of AFM and the main distinction to – for example – Scanning Tunneling Microscopy (STM) is that the sample does not have to be an electrical conductor. Effectively, it delivers high resolution microscopy for insulating samples under ambient and liquid conditions. Though the lateral resolution of AFM (in contact mode) is rather low (~30nm) due to convolution, the vertical resolution can be up to 0.1 nm. Both the lateral and the vertical resolution are dependent on the tip size. The end of the tip is ideally one single atom to ensure the highest possible resolution. However, this also increases the possibility of tip-induced damage during the measurement. In reality, contact areas are typically a few nm in diameter which lowers the resolution quality.

An alternative was provided by the development of tapping mode imaging which is considered as a dynamic excitation method. The excitation is applied externally with a fixed frequency near the resonance frequency of the cantilever. Interaction forces between the tip of the cantilever and the sample surface change the resonant frequency of the system and thus reduce the vibration amplitude and the phase change (between excitation and vibration). A control loop tries to keep the amplitude constant between the tip and sample beams by adjusting the distance and therefore the force interaction. In other words, the vibrational amplitude is taken as regulation in the course of the scan. Tapping mode is commonly used in measurements under ambient conditions or in liquids and has thus found widespread use. Another approach to realize the potential of this technique is to use frequency or amplitude modulation (non-contact mode) that uses a fixed drive frequency. The cantilever is excited by an external periodical force and changes in the frequency (amplitude) of oscillation, that act as a feedback signal, are measured when the tip approaches the sample. This method bears, in fact, some similarity to tapping mode. However, it yields much higher resolutions and is therefore most usefully applied to well-defined surfaces to utilize this feature best.[142]

Especially the soft-lithographic µCP approach of depositing molecular architectures onto the surface can be investigated with AFM. Reinhoudt *et al.* could show the localized click reaction of 1-octadecyne with an azide-terminated surface (see also chapter 3.4.3).[88] Figure 55 shows the pattern made by printing 1-octadecyne onto 11-azidoundecylsilane. Visibly, the 3×5-mm line features of the stamp are reproduced on the substrate. The average height of the 3-mm-

wide lines in the pattern is approximately 1 nm which corresponds to a tilted alkyl chain of the deposited alkyne.

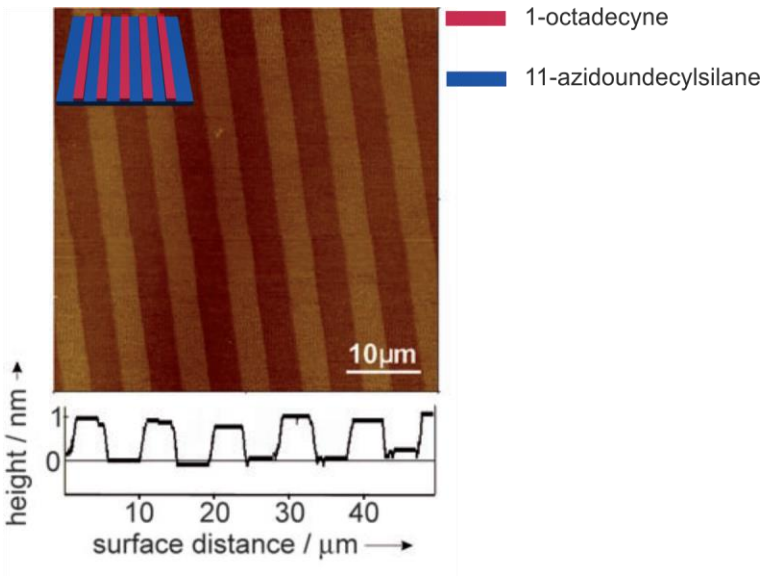

Figure 55. Tapping-mode AFM image (50 × 50 mm) and line section of a 3 × 5-mm line pattern obtained by printing 1-octadecyne onto azido-terminated SAM on a silicon oxide substrate. Adapted with permission from D. I. Rozkiewicz, D. Jańczewski, W. Verboom, B. J. Ravoo, D. N. Reinhoudt, *Angew. Chem. Int. Ed.* 2006, *45*, 5292-5296. Copyright 2006 John Wiley and Sons.

4. Published Results

4.1. Programmable multilayers of nanometer-sized macrocycles on solid support and stimuli-controlled on-surface pseudorotaxane formation

J. Poppenberg, S. Richter, C. H.-H. Traulsen, E. Darlatt, B. Baytekin, T. Heinrich, P. M. Deutinger, K. Huth, W. E. S. Unger, C. A. Schalley

Chem. Sci. **2013**, *4*, 3131−3139.

Submitted 26 February 2013, published on 15 May 2013.

The journal article is electronically available (http://dx.doi.org/10.1039/C3SC50558H).

4.1.1. Summary of the Publication

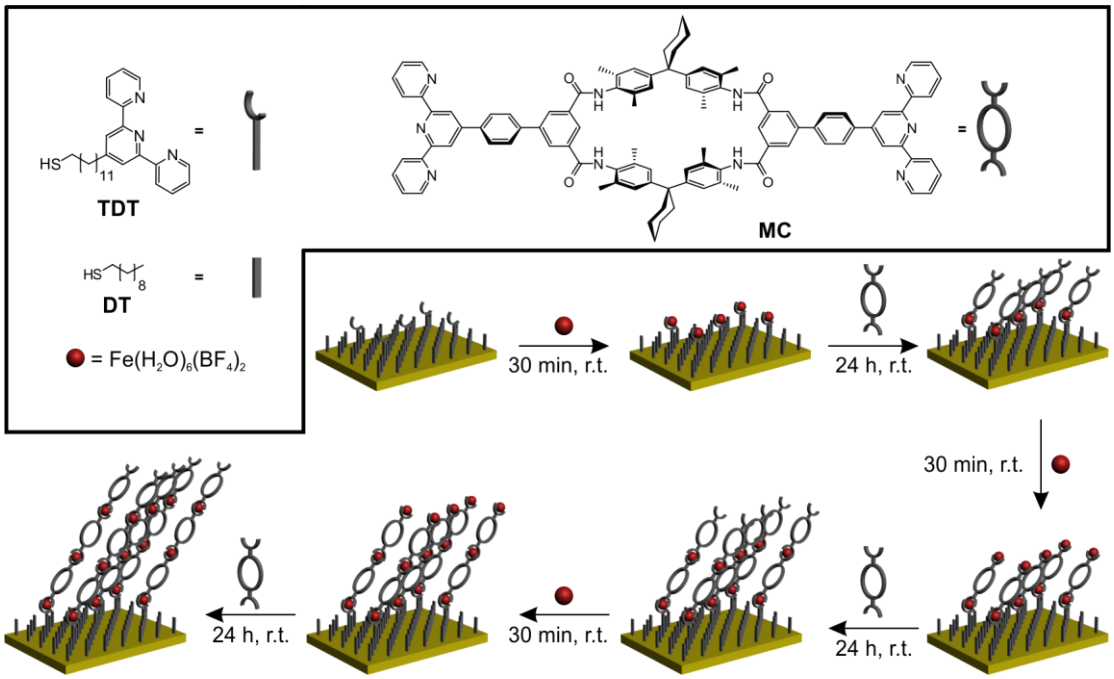

Figure 56. Schematic representation of the layer-by-layer deposition of the macrocycle multilayers; Box: The bisterpyridine-macrocycle, the iron complex, and the underlying template layer used.

In this work, the first successful deposition of tetralactam macrocycles in ordered multilayers on gold is covered. In order to build up these multilayers, the macrocycles were functionalized with terpyridines that can link with octahedrally coordinating metals like iron(II) or nickel(II). In this context, the purification of the compounds by means of dialysis was developed and established. In principle, cobalt(II) and zinc(II) are also available for this kind of multilayer. But as their diterpyridine-complexes are not stable enough, it is not possible to build up multilayers with those metals. As a template layer serves the already described, mixed **TDT**/**DT** 1/3 SAM.[66] The subsequent alternating deposition of metal-ions and macrocycles resulted in the desired multilayers. The programmability is achieved by further deposition of the metal ions in an alternating way. This layer-by-layer approach led to a multilayer with a height of more than 50 nm and more than 30 macrocycle layers. The growth of the multilayers was examined by transmission-UV/Vis and XP spectroscopy. In order to conduct transmission-UV/Vis spectroscopy with the surfaces, semitransparent slides were used consisting of a 20 nm thick gold layer that is vapor deposited onto a glass slide. After each coating step, a spectrum was recorded, to monitor the layer growth by the intensity increase of the particular absorption bands that also observed in the solution spectra (Figure 57a). A plot of the absorption intensity at 270 nm – the π-π^* transition – against the number of macrocycle layers showed a linear increase of the intensity (Figure 57a, inset). This indicates that a controlled layer-growth is present, so that for each step exactly one macrocycle layer is deposited. The analysis by XP spectroscopy verified these results: The layer growth could be confirmed by the expected regular increase of the C 1s/Au $4f_{7/2}$ peak area ratios after each deposition step (Figure 57b). By an approximation based on the Lambert-Beer law, the layer thickness could also be estimated to be ~1.5 nm which corresponds to a macrocycle tilting-angle of ca. 32° as the macrocycle has a ligand-to-ligand length of 3.55 nm.

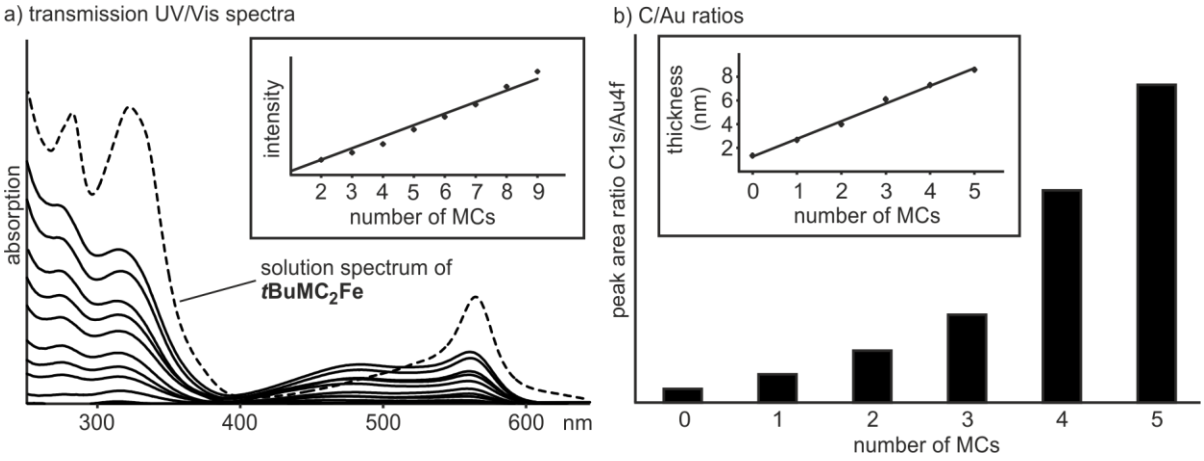

Figure 57. Surface characterization of the macrocycle multilayers. (a) Transmission UV/Vis spectra and (b) C/Au peak area ratios gained from XP spectroscopy for every macrocycle deposition step. Insets: (a) absorption intensity at 270 nm and (b) calculated layer thickness.

MM2 force field calculations of the first macrocycle layer with a metal layer on top supported this approximation. Furthermore, they revealed that the macrocycles are densely packed and arrange to optimize lateral interactions and minimize steric hindrance. The lateral interactions between the macrocycles provide highly stable multilayers that are not even damaged when treated with alkaline EDTA solution for 12 hours. The multilayers also exhibit a clear preferred orientation, which could be detected by means of angle-dependent C-K edge NEXAFS measurements that confirmed the tilting of the macrocycles of about 30° to the surface.

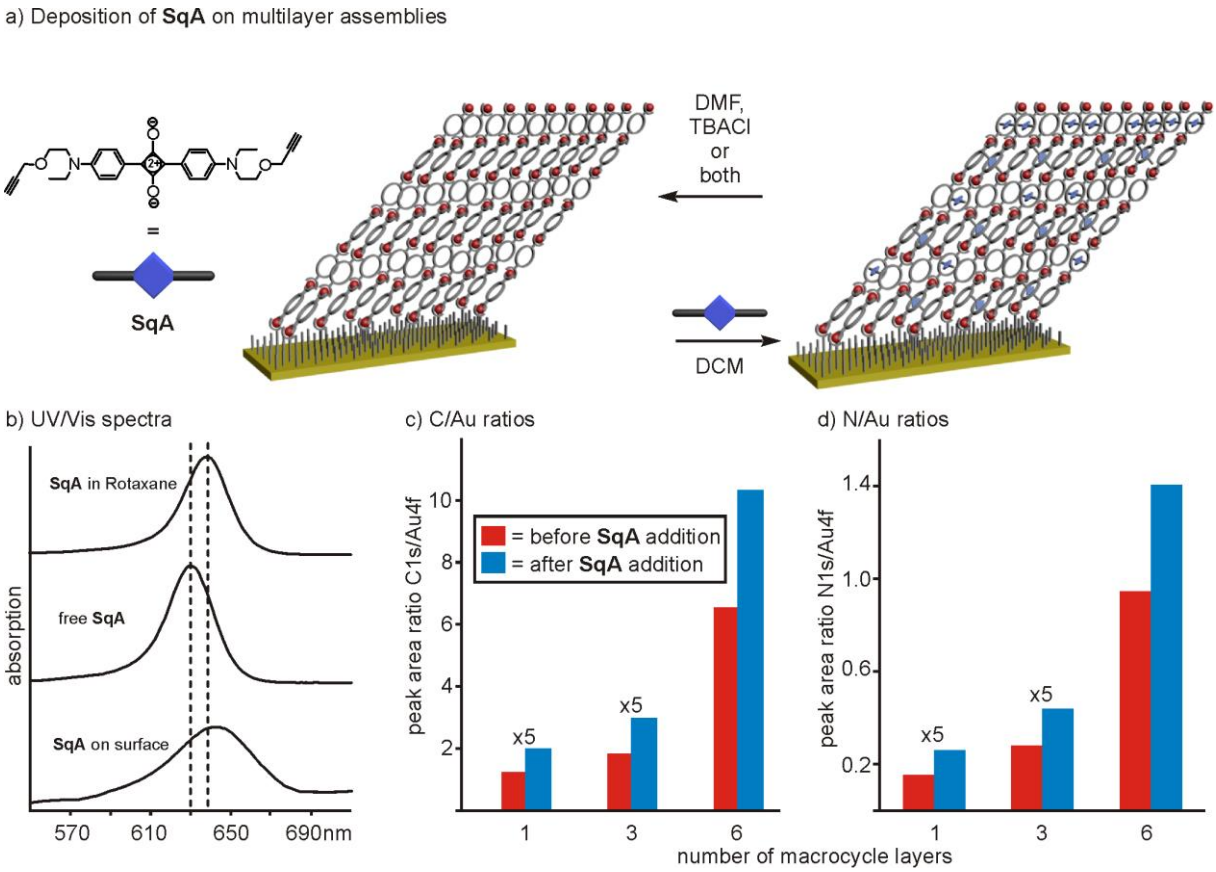

Figure 58. On-surface host-guest experiments. (a) Schematic representation of the squaraine-guest and its behavior in the macrocycle multilayers according to the gained experimental results; (b) UV/Vis spectra of a squaraine-rotaxane and the free axle in solution, and the squaraine incorporated into the multilayers.; (c) C/Au and (d) N/Au peak area ratios before (red) and after (blue) squaraine deposition determined by XPS. The peak area ratios of the one- and three-layered multilayers are multiplied by 5.

In order to investigate the accessibility of the macrocycles in the multilayer for external stimuli, a UV-active squaraine-axle (**SqA**) was synthesized and embedded into the macrocycle multilayer (Figure 58). The successful incorporation of **SqA** into the macrocycles on the surface could be detected by UV/Vis and XP spectroscopy. While the absorption of free **SqA** in solution is at 632 nm, it shifts to 640-650 nm when **SqA** is bound into the macrocycle. By using a competitive guest/solvent such as Cl^- or DMF, the guest uptake can be reversed as confirmed

by the disappearance of the absorption band from the multilayer. Thus, a reversible guest uptake could be observed, which can be repeated over several cycles. Furthermore, monitoring C 1s / Au $4f_{7/2}$ and N 1s / Au $4f_{7/2}$ peak area ratios enabled the tracking of guest uptake by XPS. In both cases the peak area ratio increases significantly when **SqA** is binding into the multilayers. As the ratios are constant for several layers, it could be concluded that the guest not even binds to the top-most layers but also to the macrocycles in the underlying layers. From the N 1s XP-spectra, it was calculated that the ratio of macrocycle to squaraine is ca. 5:1 in the multilayer which is well in line with the structure of the **SqA** as it requires the space that is offered by three macrocycles. One, in which the center piece is bound by hydrogen bonding and two adjacent macrocycles in whose cavities the side-chains reside.

4.1.2. Personal Contribution to this Publication

The synthesis of the macrocycle, the production of multilayers with iron or nickel, as well as all test reactions with other metals and host-guest chemistry experiments on the surface were carried out by Johannes Poppenberg. The preparation of the multilayer with various metals in a sequence was done by Sebastian Richter. The manufacturing of the monolayer, the synthesis and study of the test complex was performed by Christoph H.-H. Traulsen. The synthesis of the squaraine derivative was conducted by Johannes Poppenberg in collaboration with Katharina Huth. The UV/Vis measurements of the multilayers were conducted by the author in cooperation with Johannes Poppenberg and Peter M. Deutinger. The force field calculations (MM2) for the structural model were done by Sebastian Richter and Christoph H.-H. Traulsen. The XPS and NEXAFS measurements were carried out by Erik Darlatt and the author. The interpretation of the results was done by Johannes Poppenberg, Christoph H.-H. Traulsen, Erik Darlatt, and Sebastian Richter. Creating the concept and writing of the manuscript was done by Johannes Poppenberg. All authors contributed to the final version of the manuscript.

4.2. Principal Component Analysis (PCA)-Assisted Time-of-Flight Secondary-Ion Mass Spectrometry (Tof-SIMS): A Versatile Method for the Investigation of Self-Assembled Monolayers and Multilayers as Precursors for the Bottom-Up Approach of Nanoscaled Devices

Markus Holzweber, Thomas Heinrich, Valentin Kunz, Sebastian Richter, Christoph H.-H. Traulsen, Christoph A. Schalley, and Wolfgang E. S. Unger
Anal. Chem. **2014**, *86*, 5740–5748.

Submitted 6 January 2014, published 15 May 2014.

The journal article is electronically available (http://dx.doi.org/10.1021/ac500059a).

4.2.1. Summary of the Publication

ToF-SIMS is sensitive enough to provide the process control needed to produce high-quality layer systems yet data analysis is very demanding. This work shows how a large amount of data generated by a standard ToF-SIMS measurement can be simplified by PCA. It provides the possibility to identify key fragment peaks characterizing a given sample type, a survey of the point-to-point reproducibility across the sample set, and a summary of the relationship between different sample sets. The approach used in this work ensures that the variance in the given data set is due to real sample differences. Two examples were investigated to show how PCA-assisted ToF-SIMS can help to get high-quality mono- and multilayers.

The first example features that different cleaning methods can result in a varying deposition quality of a monolayer. A pyridyldodecane silane (**PDS**) SAM on hydroxyl-terminated silicon is investigated that can be taken as a template for a further coordinative layer-by-layer deposition. Subsequently, a layer of Pd^{II} ions using $Pd(CH_3CN)_4(BF_4)_2$ is deposited. Figure 59a shows the **PDS**-SAM and the corresponding ToF-SIMS mass spectrum obtained in positive-ion mode in the mass range from m/z 0 to 300 which shows the expected fragmentation pattern and therefore indicates the successful formation of the SAM. Initially, a significant contamination of sodium sulfate was detected after the deposition of the SAM. Therefore, three different cleaning procedures of the surfaces before SAM-deposition were developed in order to minimize this contamination. The initial cleaning by rinsing the surface with deionized water for 30 s

(procedure 1) was first extended to 2 min (procedure 2), and then to 2 min of rinsing with an additional immersion of the surface in Millipore water (procedure 3). The score plot from a PCA of the positive secondary ions in a range of *m/z* 0 to 300 of the **PDS**-SAM by the three different cleaning methods was then investigated (Figure 59b). It appears that procedure 1 is clearly separated to the other two procedures and shows a poor point-to-point reproducibility which is reflected by the large scattering of the data in addition to the sodium-sulfate contamination.

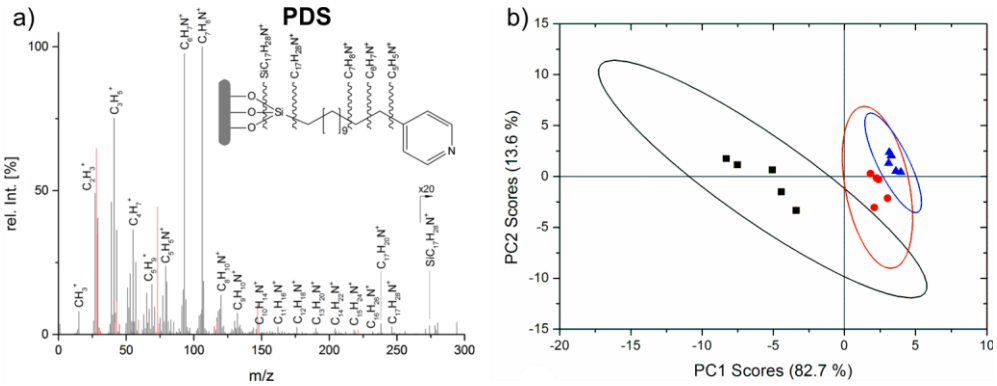

Figure 59. a) Positive-ion-mode ToF-SIMS spectrum of the PDS SAM. Peaks in red correspond to PDMS residues from the preparation procedure. b) Scores plot of the first two principal components for the 3 different cleaning procedures. The percentage in the brackets denotes how much variance is caught by the corresponding principal component. Black squares: procedure 1, blue triangles: procedure 2, red circles: procedure 3. The ellipses show the 95% confidence limit.

The positive loadings – a measure that more secondary ions are generated – highlight fragment ions that are characteristic for the formed **PDS** SAM (i.e., $C_6H_7N^+$ and $C_7H_8N^+$) for procedure 2 and 3 which indicates a more regular and well-oriented SAM and, as a result, a major advantage for these cleaning procedures. In order to distinguish the two improved cleaning procedures, a PCA just with the corresponding data sets was carried out. This lead to the unexpected conclusion that the additional rinsing with Millipore water in cleaning procedure 3 did not improve the quality of the SAM as it is also visible in the scores plot in Figure 59b due to the larger scattering. A PCA was also carried out for the coordination step of Pd^{II} to the **PDS** SAM. In principle, it would be enough to just check for the presence of Pd^+ secondary ions. In fact, these are clearly observable at m/z = 105.90 with the typical isotope pattern. However, a ToF-SIMS mass spectrum usually contains much more information that can be found and interpreted with help of PCA. Indeed, the separation is not just due to the Pd^+ ions but also due to ions from the ligand CH_3CN and adducts containing the acetonitrile ligand in the positive loadings (for the **PDS**+Pd-SAM). In contrast, the suppressed signals in the negative loadings clearly correspond to molecular units of the **PDS**-SAM. This not only shows that Pd(II) is present on the surface but that it sits on top of the **PDS**-SAM.

The second example in this study focuses on the LbL self-assembly of macrocycles and the corresponding stepwise surface modification (see chapter 4.1, Figure 56). Therefore, each deposition step is monitored by ToF-SIMS. The scores plot of the entire data set in Figure 60a revealed that the individual samples are well separated although deviations in the mass spectra are not easily assignable when using a univariate approach. The clustering of the samples with Fe coordinated to terpyridine as the top layer as well as the samples with just terpyridine as the top layer with nearly the same value in the scores plot also indicates that these samples exhibit similar spectra. However, when the PC1 scores are plotted versus the PC2 scores like in Figure 60b, a separation of the **TDT/DT**-SAM with coordinated Fe to the deposition step with a similar surface chemistry becomes visible. This can be explained by the different orientation of the terpyridines in the monolayer compared to a macrocycle layer which is also reflected by clear separation of the pristine **TDT/DT** SAM. Although the third Fe**MC** layer exhibits the same surface chemistry – the terpyridine end-group points toward the surface – which should lead to a similar clustering to the previous macrocycle deposition, it is separated from them. This could be due to a change to a more-tilted orientation of the macrocycle layers or due to an accumulation of defects in the course of the multilayer formation.

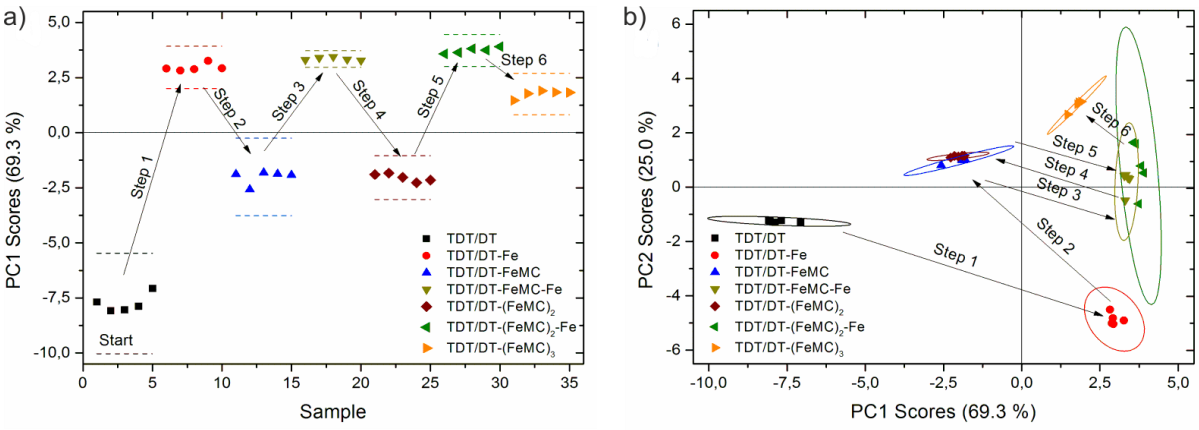

Figure 60. PCA scores plot of the whole layer-by-layer data set; a) PC1 scores versus the sample number and b) PC1 versus PC2 scores.

4.2.2. Personal Contribution to this Publication

Markus Holzweber conducted the ToF-SIMS measurements and processed the data with Principal Component Analysis. The author synthesized the macrocycles under study, deposited them into multilayers and helped with the interpretation as well as processing of the data. Valentin Kunz and Christoph H.-H. Traulsen synthesized the **PDS** molecule and developed the different deposition procedures of the SAM. Sebastian Richter synthesized the **TDT** molecule. Markus Holzweber and the author conceived the concept and wrote the article. All authors contributed to the final version of the manuscript.

4.3. Sequence-Programmable Multicomponent Multilayers of Nanometer-Sized Tetralactam Macrocycles on Gold Surfaces

Sebastian Richter, Christoph H.-H. Traulsen, Thomas Heinrich, Johannes Poppenberg, Charlene Leppich, Markus Holzweber, Wolfgang E. S. Unger, and Christoph A. Schalley

J. Phys. Chem. C **2013**, *117*, 18980–18985.

Submitted 4 June 2013, published 19 August 2013.

The journal article is electronically available (http://dx.doi.org/10.1021/jp405492v).

4.3.1. Summary of the Publication

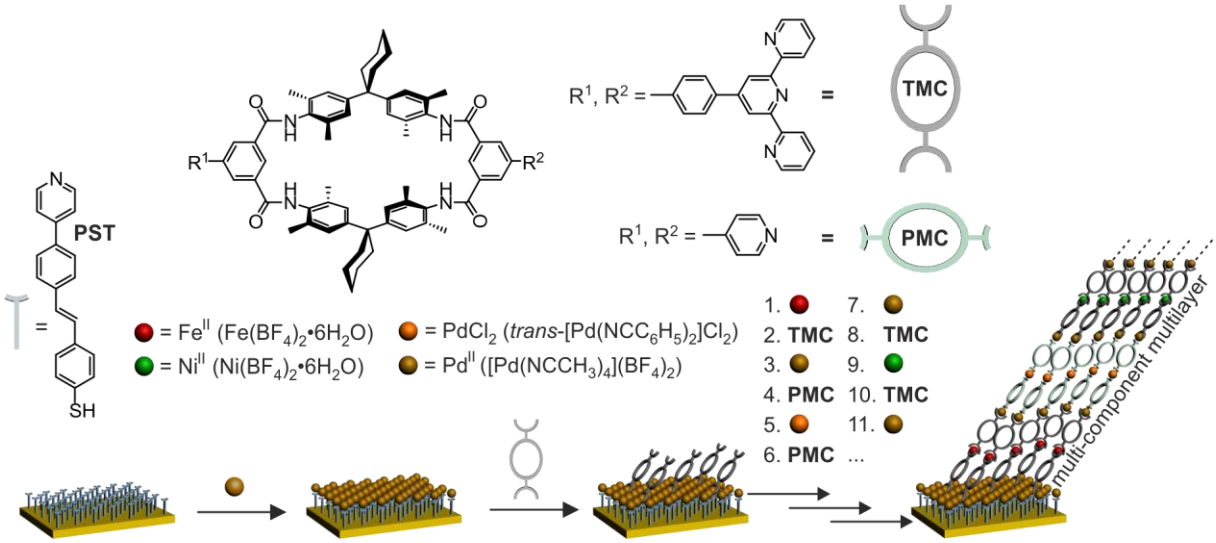

Figure 61. Deposition procedure of the sequence programmable multilayer with a schematic illustration of the organic and metallic compounds used in this work.

In this work, the extension of the sequence programmability of the multilayers was achieved by two differently functionalized macrocycles and four different connecting metal layers for the layer-by-layer deposition of multilayers. As illustrated in Figure 61, the macrocycle used is either functionalized with terpyridine (**TMC**) or the new pyridine-motif (**PMC**). In order to connect these ligands, metals with different coordination spheres are needed: Two terpyridines can be connected by an octahedrally coordinating metal ion like Fe^{II} or Ni^{II}; two pyridines are connected with the linearly coordinating *trans*-$PdCl_2$ metal connector; and a terpyridine is connected to a pyridine with square-planarly coordinating Pd^{II} and vice versa. As the template, the

pyridine-terminated **PST**-SAM was used for every multilayer described in this work. Towards a fully sequence-programmed multilayer, four intermediate steps were taken. First, a dipyridine-terminated macrocycle **PMC** was deposited into a multilayer with *trans*-$PdCl_2$ as the metal connector. This multilayer was analyzed with transmission-UV/Vis and XP spectroscopy. UV/Vis revealed that, although the multilayer grows regularly with every deposition step – also shown by XPS, a self-propagating growth is present for this multilayer. This can be due to the additionally stored metal ions in underlying layers which then contribute to the growth of the subsequently deposited layers. Furthermore, layer thickness calculations gave a mean layer growth of 1.2 nm with every step. This corresponds to a macrocycle tilt angle of ca. 28° to the surface. In a second step, it could be shown that it is in principle possible to deposit multilayers of terpyridine-functionalized macrocycles **TMC** onto the pyridine-terminated template layer. Interestingly, this multilayer does not exhibit self-propagation. Consequently, no additionally stored metals contribute to the layer-growth.

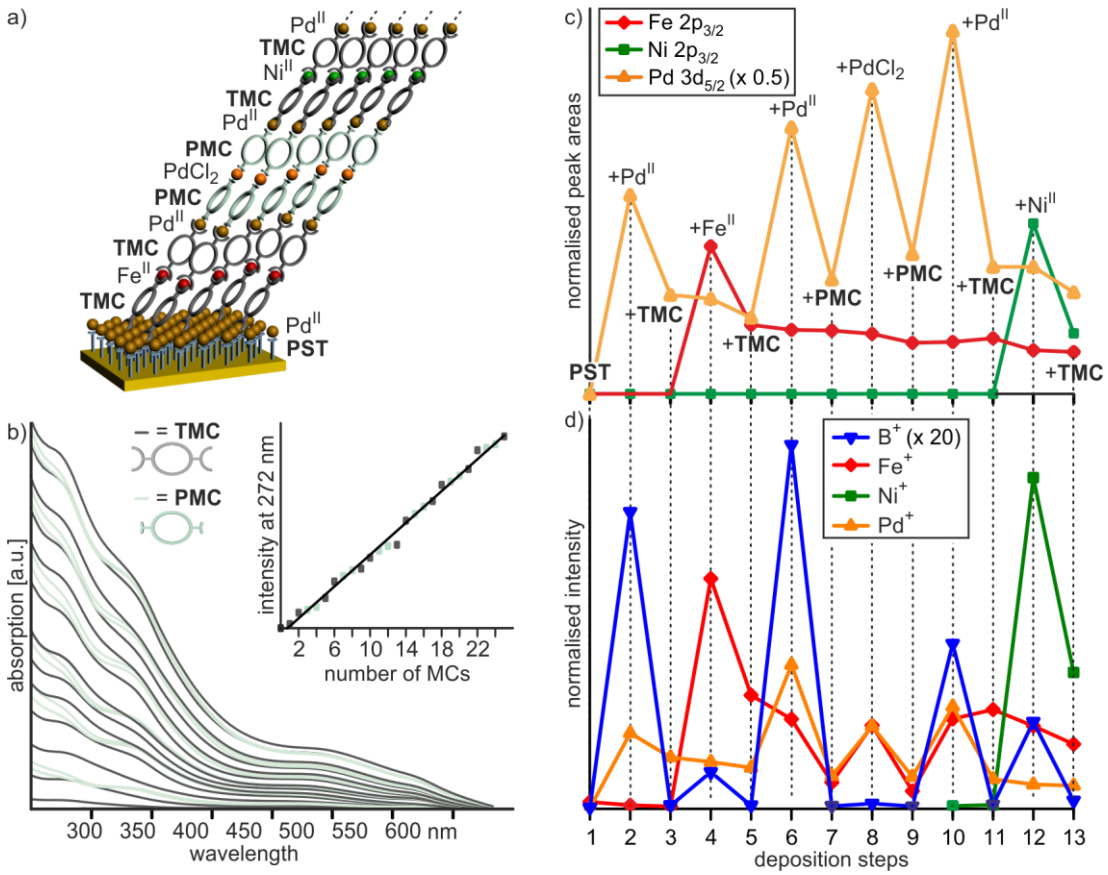

Figure 62. Analysis of the sequence programmable multilayer. (a) Illustration of the idealized programmed multilayer sequence. (b) UV/vis spectra after each macrocycle deposition; inset: intensity growth at 272 nm. (c) XPS peak areas of Pd $3d_{5/2}$, Fe $2p_{3/2}$, and Ni $2p_{3/2}$ as well as (d) ToF-SIMS intensities for B^+, Fe^+, Ni^+, and Pd^+ normalized to the total ion yield after each deposition step.

The third step consisted of the deposition of an alternating multilayer of **PMC** and **TMC**. In order to connect the macrocycles, square-planarly coordinating Pd^{II} metal ions are used. UV/Vis analysis show that the multilayer exhibits a self-propagating growth due to the use of just one metal as a connector.

Finally, a more sophisticated multilayer was designed in which all mentioned components were applied in a sequence to achieve the highest possible complexity (Figure 62). Therefore, the type of macrocycle was changed after every second macrocycle layer to produce a multilayer sequence consisting of 16 layers that can be expressed as follows: **PST**→(Pd^{II}→**TMC**→Fe^{II}→**TMC**→Pd^{II}→**PMC**→*trans*-$PdCl_2$→**PMC**→Pd^{II}→**TMC**→Ni^{II}→**TMC**→ Pd^{II}→**PMC**→*trans*-$PdCl_2$→**PMC**)$_n$. The sequence of different macrocycles and metals can be excellently followed by transmission-UV/Vis, XPS and ToF-SIMS. The continuous growth of the $\pi \rightarrow \pi^*$ band at 272 nm and the red shift of the surface plasmon resonance from 467 to 485 nm in the transmission UV/vis absorption spectra (Figure 62b) provide clear evidence for the multilayer growth. The $\pi \rightarrow \pi^*$ absorption band changes accordingly to the different absorptions of the macrocycles: When **TMC** is located on top of the multilayer, a more intense increase of the absorption band at 280 nm is observed and when **PMC** is on top of the multilayer, a stronger increase is observed at 272 nm. Furthermore, no self-propagating effect is detected. By determining the peak areas, we could show with XPS that the metal connectors can be programmed and are located mainly in their destined layer. This was also confirmed by ToF-SIMS which could also distinguish between the different Pd-ions by investigating B^+ fragments which should only appear with Pd^{II} as this has two BF_4^- as counterions ($Pd(NCCH_3)_4(BF_4)_2$). The multilayer growth, determined with XPS, also showed a linear behavior. The average layer thickness approximately corresponds to a tilt angle of ca. 24° to the surface. A preferred orientation could be demonstrated for these multilayers. The combination of the carried out UV/Vis, XPS and ToF-SIMS studies shows the programmability of the mixed multilayer. In conclusion, a sequential deposition process has been developed that yields programmable macrocycle multilayers. This is particularly important regarding the long-term goal of the project that is the construction of multilayers of differently switchable rotaxanes.

4.3.2. Personal Contribution to this Publication

The synthesis of the metal-macrocycle complexes in solution, the preparation of the mixed multilayers, all UV/Vis experiments, as well as the planning and coordination of the project were carried out by Sebastian Richter. The synthesis of the dipyridine-functionalized macrocycle and the corresponding multilayer was done by Christoph H.-H. Traulsen in cooperation with Charlene Leppich. The preparation of the **TMC** multilayers with Fe^{II}-ions on the **PST**-SAM

was performed by Johannes Poppenberg. All XPS and NEXAFS measurements were performed by the author. The interpretation of the results was done in cooperation with Sebastian Richter, Johannes Poppenberg, and Christoph H.-H. Traulsen. Markus Holzweber conducted ToF-SIMS measurements and interpreted the data. Sebastian Richter conceived the concept and wrote the manuscript. All authors contributed to the final version of the manuscript.

4.4. Synthesis and Coordinative Layer-by-Layer Deposition of Pyridine-Functionalized Gold Nanoparticles and Tetralactam Macrocycles on Silicon Substrates

Christoph H.-H. Traulsen, Valentin Kunz, Thomas Heinrich, Sebastian Richter, Markus Holzweber, Andrea Schulz, Larissa K. S. von Krbek, Ulf T. J. Scheuschner, Johannes Poppenberg, Wolfgang E. S. Unger, and Christoph A. Schalley

Langmuir **2013**, *29*, 14284–14292.

Submitted 20 August 2013, published 25 October 2013.

The journal article is electronically available (http://dx.doi.org/10.1021/la403222x).

4.4.1. Summary of the publication

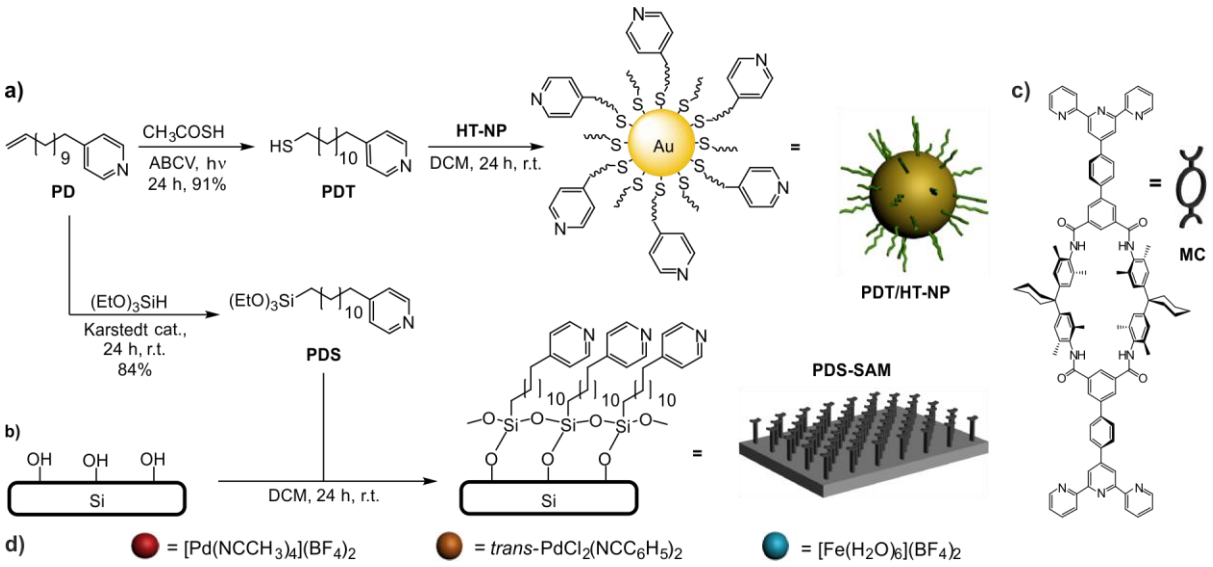

Figure 63. (a) Synthesis of pyridine-terminated templates and preparation of mixed-shell PDT/HT-NPs from hexanethiol-capped HT-NPs. (b) Deposition of PDS on a hydroxylated silicon surface to yield a surface covered with a PDS-SAM, along with (c) the terpyridine-functionalized macrocycle MC and (d) the used metal complexes.

In this work, the synthesis of pyridine-capped gold nanoparticles and their incorporation into composite multilayer on glass and silicon is presented. Furthermore, the uptake of a squaraine axle into macrocycle multilayers that are either capped with a nanoparticle monolayer or into

a mixed multilayer with alternately deposited macrocycle and nanoparticles was studied. Again, the earlier introduced terpyridine-functionalized macrocycle **MC** was used for multilayer formation (Figure 63c). The pyridine-capped nanoparticles **PDT/HF-NP** were obtained by partially exchanging the ligands of previously synthesized hexanethiol-protected nanoparticles **HT-NP** to 12-pyridyl dodecane-1-thiol ligands **PDT** (Figure 63a). Particles of different sizes were prepared and analyzed by TEM, DLS, UV/Vis, NMR and IR measurements. For the deposition of these nanoparticles into multilayers on the surface, a suitable template is needed. As the deposition on gold would lead to a rather complicated analysis by XPS as well as UV/Vis experiments, a triethoxysilane with a dodecane backbone and a pyridine terminus **PDS** was used for the deposition on glass or silicon. The successful deposition of the template layer as well as its high quality and order was demonstrated with XPS, ToF-SIMS, AFM, and NEXAFS measurements. The subsequent deposition of multilayers was initially done and investigated with separately deposited nanoparticles or macrocycles. Similar to the previous study, the macrocycle multilayer was anchored on the template with Pd^{II}-ions and the following layer growth was done with Fe^{II}-ions as connecting metal. For the deposition of the nanoparticle multilayer, only Pd^{II} was used. Both multilayers were analyzed with transmission-UV/Vis spectroscopy in order to follow the layer growth corresponding to their characteristic absorption band at 290 nm for the macrocyles ($\pi - \pi^*$ transition) and 560 nm for the nanoparticles (surface plasmon resonance). The nanoparticle multilayer was also further investigated by XPS which confirmed the regular growth.

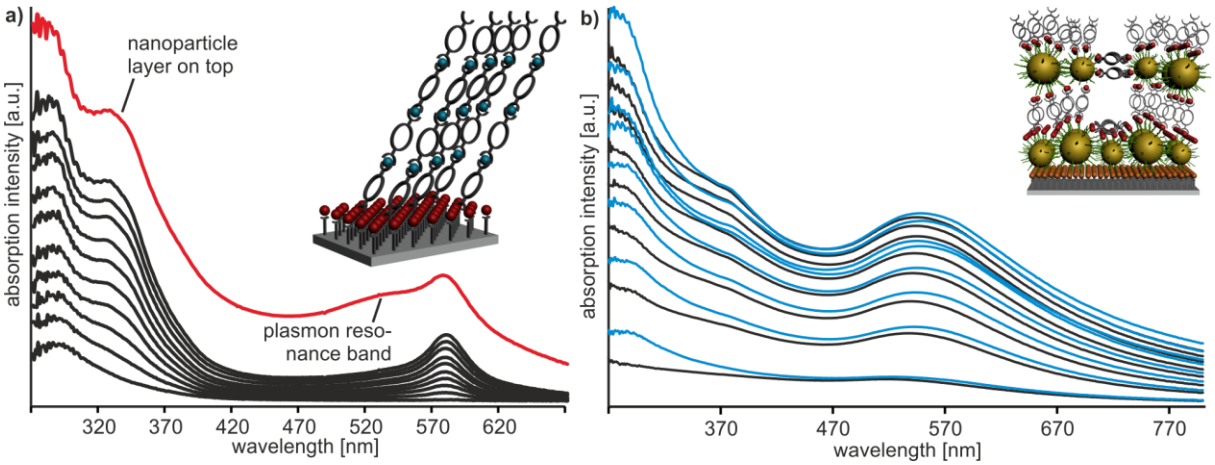

Figure 64. (a) Transmission UV/Vis spectra of MC multilayers on a PDS-SAM recorded after each MC (black) deposition step. The spectrum depicted in red corresponds to a ten-layer stack of macrocycles on top of which Pd^{II} ions followed by a layer of PDT/HT-NP nanoparticles (red) were deposited. (b) Transmission UV/Vis spectra of an alternating MC/PDT/HT-NP multilayer on a PDS-SAM recorded after each NP (black) and MC (blue) deposition.

Moreover, composite multilayers were obtained that, as already stated, differ in their composition. First, the macrocycle multilayer was capped with a nanoparticle layer. The success of

the process was confirmed by a large absorption increase with a strong plasmon band in the UV/Vis spectrum when the nanoparticles are deposited on the multilayer (Figure 64a). In the second case, a mixed multilayer was deposited that contained an alternating sequence of nanoparticles and macrocycles. The composite multilayer showed the expected behavior: With every deposition of the macrocycle, the absorption at 290 nm increased and when the nanoparticles were deposited, their plasmon resonance gave a strong absorption at 540 nm (Figure 64b). XPS showed that the C 1s/Si 2p peak area ratio increases with each deposited layer while the C 1s/Au $4f_{7/2}$ ratio revealed an alternating behavior with a decrease upon nanoparticle and an increase upon macrocycle immobilization.

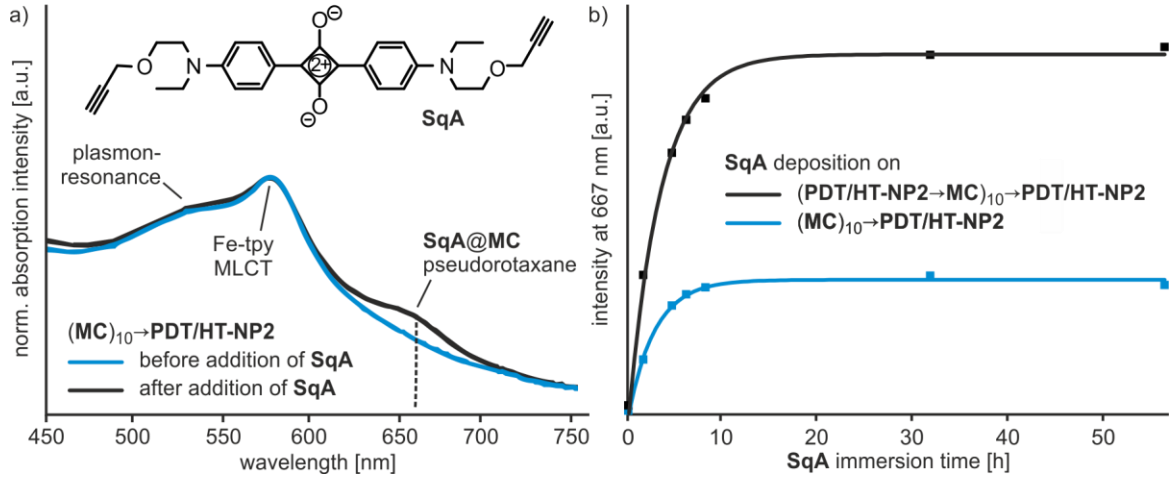

Figure 65. Uptake experiments of two types of multicomponent multilayers with the SqA-axle. (a) Transmission UV/vis spectra of the $(MC)_{10}$→PDT/HT-NP2 multilayer before (blue line) and after (black line) immersion into a 1 mM solution of SqA in DCM. Intensities were normalized to the MLCT band to facilitate comparison. (b) Transmission UV/vis absorption intensity 667 nm plotted versus SqA deposition time for $(MC)_{10}$→PDT/HT-NP2 (blue line) and (PDT/HT-NP2→$MC)_{10}$→ PDT/HT-NP2 (black line) multilayers. Langmuir adsorption kinetics were used to fit the obtained data points.

In the end, the latter two examples were investigated concerning their guest uptake ability and pseudorotaxane formation with the squaraine axle **SqA**. Interestingly, the composite multilayers are able to incorporate more guests than the capped macrocycle multilayers while the uptake rates are not significantly different between the two multilayers as was shown by UV/Vis studies on the time-dependent increase of the **SqA** absorption band at 667 nm that arises when the multilayers are treated with a **SqA** solution (Figure 65a and b). This was ascribed to the introduction of the nanoparticles which leads to a lower order and therefore more space between the macrocycles.

4.4.2. Personal Contribution to this Publication

The synthesis of the nanoparticles functionalized with only **PDT** was carried out by Christoph H.-H. Traulsen in collaboration with Larissa K. S. von Krbek. The synthesis of **SqA**, its deposition into composite multilayers, and their preparation was done by Christoph H.-H. Traulsen. Valentin Kunz synthesized **PDS**, all particles used for surface deposition, and carried out the deposition of these substances into multilayers. The author synthesized the macrocycle under study, conducted all XPS and NEXAFS measurements, and did the theoretical evaluation of the Langmuir absorption kinetics. Sebastian Richter deposited the pure macrocycle multilayers on **PDS**. The development of an appropriate procedure for monolayers on glass or silicon surfaces using triethoxysilanes was carried out by Johannes Poppenberg in collaboration with Ulf T. J. Scheuschner. Markus Holzweber conducted ToF-SIMS and Andrea Schulz AFM, SEM and TEM measurements. The interpretation of the results was done by the author in collaboration with Christoph H.-H. Traulsen, Valentin Kunz, Sebastian Richter and Johannes Poppenberg. Creating the concept and writing the manuscript was done by Christoph H.-H. Traulsen. All authors contributed to the final version of the manuscript.

4.5. The versatility of „click“ reactions: molecular recognition at interfaces

Thomas Heinrich, Christoph H.-H. Traulsen, Erik Darlatt, Sebastian Richter, Johannes Poppenberg, Nora L. Traulsen, Igor Linder, Andreas Lippitz, Paul M. Dietrich, Baha Dib, Wolfgang E. S. Unger, and Christoph A. Schalley
RSC Adv. **2014**, *4*, 17694−17702.

Submitted 27 February 2014, published 31 March 2014.

The journal article is electronically available (http://dx.doi.org/10.1039/C4RA01730G).

4.5.1. Summary of the Publication

Although the previous reported LbL self-assembly shows promising results, the transfer of supramolecular structures and processes from solution to solid supports is still challenging. The approach showed in this work combines SAMs, that can be covalently functionalized, with molecular recognition and should therefore act as an example for the covalent deposition of supramolecular switches on to surfaces. An azide-terminated undecanethiol SAM is covalently functionalized by CuAAC-reactions with host or guest molecules which allow the specific non-covalent attachment of another layer through supramolecular interactions.

Before the click reactions are realized, the X-ray induced decomposition of the azide-terminus had to be investigated. The irradiation damage has earlier caused major characterization problems as it yielded a new nitrogen compound which interfered with the newly built triazole and the additional nitrogen signals of the deposited molecules. To have a deeper insight and clearly assign the products that can arise, 35 N 1s XP spectra were recorded in 4 min intervals at the same spot. This was sufficient to follow the time course of the decomposition until just a small part of intact azide remained. The observed decomposition behavior led to the conclusion that a highly reactive nitrene compound is formed followed by a 1,2-hydrogen shift from the adjacent carbon to the nitrogen that leads to the formation of an imine. This assumption could be supported by N 1s XPS and N-K edge NEXAFS measurements.

After the determination of the decomposition product, the deposition of an overlying supramolecular layer via click chemistry and subsequent host-guest complexation experiments were

studied. On-surface CuAAC reactions were performed using different alkyne-substituted supramolecules such as tetralactam (**TLM1**) and crown ether (**CE1**) macrocycles, as well as diketopiperazine (**DP1**) and ammonium (**AM1**) guests. In order to clearly assign all observed XPS peaks, an unfunctionalized alkyne (**HEX**) was included in this series as a reference (Scheme 4).

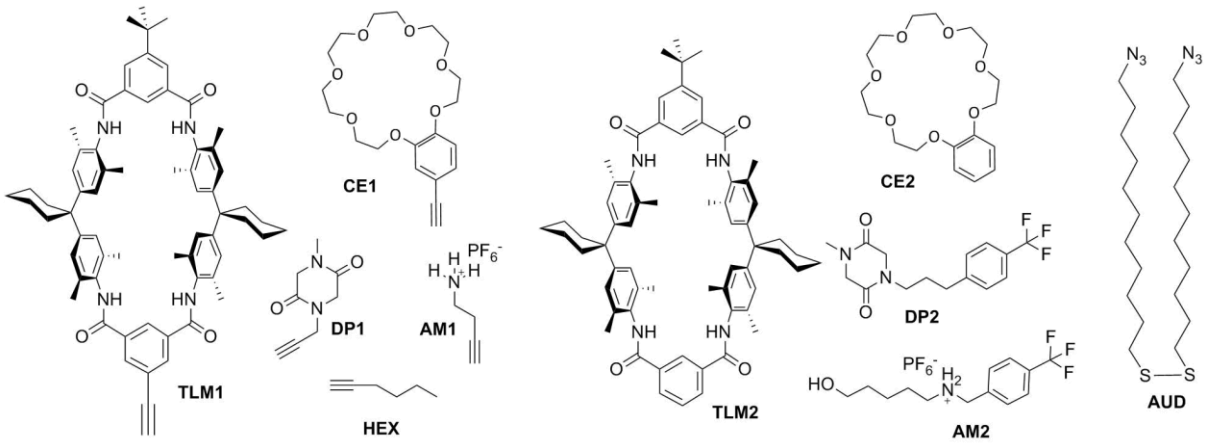

Scheme 4. The molecules used in this study. Left: Alkyne-functionalized host and guest molecules and control compound HEX. Middle: The corresponding guests and host. Right: Monolayer-forming AUD.

The N 1s XP spectra of all compounds revealed the formation of a compound with three or more different nitrogens that are in line with those of a newly built triazole. Furthermore, the N-K edge NEXAFS spectra revealed three new nitrogen signal for all conducted cycloadditions except for **TLM1** (Figure 66, left). However, the cycloaddition could also be verified for **TLM1** by additional irradiation experiments. In addition, the C 1s spectra of the different compounds reveal new signals that can be assigned to the carbons that are characteristic for the particular compounds. (Angle-resolved) C-K edge NEXAFS measurements showed new signals for all deposited compounds except for **HEX**. Additionally, **CE1** and **DP1** seem to exhibit a certain preferential orientation as their spectra show a linear dichroism. In conclusion, the azide-alkyne cycloaddition worked for every compound under study. However, the tetralactam macrocycle showed low azide turnover as it has the highest steric demand and the clicked **AM1** did not show the presence of an ammonium ion but of an unprotonated amine which can be due to the deprotonation of the ammonium as a result of rinsing after the click reaction. As amines are not able to strongly bind crown ethers, **AM1** can be taken as a reference for the subsequent four different host-guest experiments that are possible: To **TLM1**, a CF_3-functionalized diketopiperazine (**DP2**) was added, to **DP1**, another tetralactam macrocycle **TLM2** can be added, a CF_3-functionalized ammonium compound can be deposited to the **CE1** layer, and **AM1** can be treated with a crown ether (**CE2**).

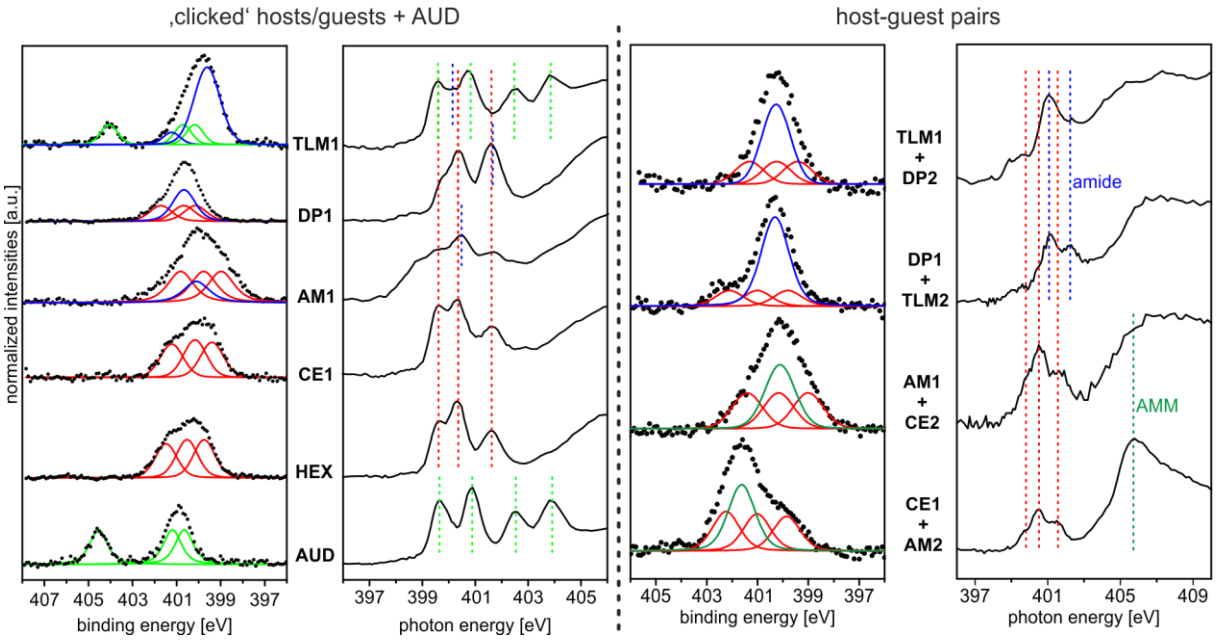

Figure 66. Left: Qualitative N 1s XP spectra of the surfaces of HEX, CE1, AM1, DP1 and TLM1 in comparison to that of the pristine AUD SAM (hv = 500 eV and 0° emission angle) and the corresponding NEXAFS spectra. Right: Qualitative N 1s XP spectra of the four host–guest pairs (hv = 500 eV and 0° emission angle) and their corresponding NEXFAS spectra (55° incident angle).

Again, the N 1s XP spectra as well as the N-K edge NEXAFS give a detailed insight (Figure 66, right). The **CE1**-**AM2** surface for example shows a prominent feature (AMM) in the N K-edge NEXAFS spectrum which is a clear sign for the presence of an ammonium-ion and therefore also **AM2**. Deposition of the tetralactam macrocycle **TLM2** to **DP1** can also be clearly observed in the N 1s XP spectra: The intensity of the peak representing the amides in **DP1** as well as **TLM2** experiences a significant increase after **TLM2** treatment. The picture is not as clear when the opposite pairs are analyzed. Therefore, the C 1s XP spectrum has to provide more detailed insight. In fact, it gives a clear indication for the presence of **DP2**, as the signal for its CF_3-group is clearly visible in the corresponding spectrum. This is also true for the **CE1**-**AM2** host-guest pair. Furthermore, the presence of **TLM2** is confirmed by the altered C 1s XP spectrum that significantly differs to the one of the untreated **DP1**. Again, these results give a clear indication that the experiments were successfully conducted with the expected results. When the surfaces are analyzed by angle-resolved C-K edge NEXAFS spectra, it becomes apparent that just the **CE1**-**AM2** pair retains its preferred orientation: Only here, the linear dichroism is even more pronounced and the π*-resonance exhibits a new angular dependency. Reversibility was shown with the **DP1**-**TLM2** pair and the corresponding N 1s as well as C 1s spectra. After rinsing with DMF, the surface resembles the initial spectra again. This is a clear indication that the macrocycle is washed off again.

4.5.2. Personal Contribution to this Publication

The author was responsible for the conceptual development and the coordination of project. He also performed the click reactions on the azide-terminated SAMs, conducted the XPS and NEXAFS experiments of the host-guest experiments, and interpreted the resulting spectra. The author also conceived and wrote the article. Christoph H.-H. Traulsen helped with the conceptual development and interpretation of the XPS and NEXAFS spectra, and conducted the on-surface host-guest experiments. E. Darlatt conducted the XPS and NEXAFS experiments on the decay of the azide terminus as well as the click reactions, and interpreted the results. Sebastian Richter, Johannes Poppenberg, Nora L. Traulsen, Igor Linder, and Baha Dib contributed to the synthesis of the compounds under study. Andreas Lippitz and Paul M. Dietrich helped with XPS and NEXAFS measurements. All authors contributed to the final version of the manuscript.

4.6. Photocontrolled On-Surface Pseudorotaxane Formation with Well-Ordered Macrocycle Multilayers

Felix B. Schwarz, Thomas Heinrich, J. Ole Kaufmann, Andreas Lippitz, Rakesh Puttreddy, Kari Rissanen, Wolfgang E. S. Unger, and Christoph A. Schalley
Chem. Eur J. **2016**, *22*, 14383-14389.

Submitted 01 July 2016, accepted 01 August 2016.

The journal article is electronically available (http://dx.doi.org/10.1002/chem.201603156).

4.6.1. Summary of the Publication

An unambiguous analysis of the structural changes inside rotaxane mulitayers on surfaces that come with their stimuli-induced switching is crucial for understanding these processes. A chemical stimulus in fact unavoidably brings impurities into the system and it is not sure if it addresses the rotaxanes even in the lowest layers. In this work, photochemically switchable molecules were designed and synthesized to incorporate them into the previously described macrocycles in solution as well as in multilayers on solid support to enable pseudorotaxane studies. The molecule was designed in such a way that the *cis-trans* photoisomerism of azobenzene is able to control the threading and dethreading of the diketopiperazine axle-piece into a tetralactam macrocycle. The photoswitch as well as the diketopiperazine were attached to a rigid xanthene backbone which keeps them in a fixed position to each other. This enables the azobenzene to influence the binding strength of the the diketopiperazine by steric hinderance: When the azobenzene is in its trans-configuration, the binding-site is blocked, but in the cis-isomer, the binding-site becomes available. The axle was synthesized over ten steps in a 14% yield. Methylation of the diketopiperazine-NH was carried out in order to prevent additional hydrogen bonding. Crystal structures revealed that the azonbenzene is in its *trans* configuration almost coplanar to the xanthene-unit while the diketopiperazine is almost perpendicular to the backbone due to steric hinderance. This facilitates a binding into the macrocycle cavity when the azobenzene is in its cis configuration as revealed by MM2 calculations of the pseudorotaxane complex.

In a first step, the pseudorotaxane formation was investigated in solution by UV/Vis and NMR spectroscopy. Photoisomerization of the axle from *trans* to *cis* was carried out by irradiating a solution of it in CH_2Cl_2 with a wavelength of λ_1 = 365 nm for 10 min to get the photostationary

state. The back isomerization to the *trans* configuration was performed by either irradiation with an LED lamp at λ_2 = 470 nm or by equilibration in the dark at room temperature for 24 hours. The UV/Vis spectrum of the axle in the *trans* configuration (Figure 67b) shows the characteristic absorption band for the π→π* transition of the azobenzene at 323 nm, which experiences a decrease when irradiated at λ_1, indicating the formation of the *cis* configuration. After irradiation at λ_2 for 10 minutes or equilibration in the dark over 24 h, the spectrum resembled the initial state. Reversibility was tested by alternating irradiation over five cycles (Figure 67c). UV/Vis analysis was also carried out with a 1:1 mixture of the axle and a *tert*-butyl-substituted macrocycle. No shifts of absorption maxima could be observed due to the small influence of the chromophor's electronic properties by the binding.

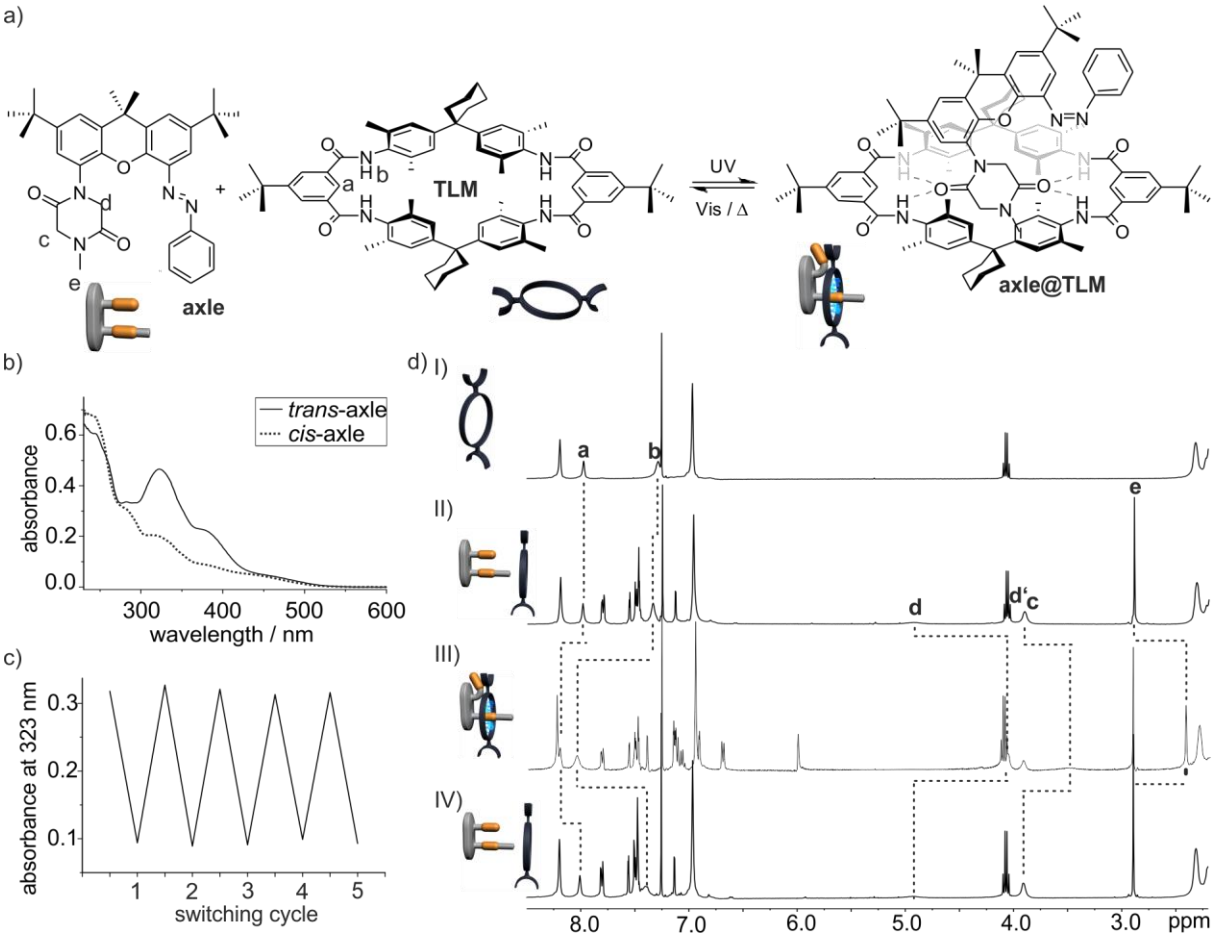

Figure 67. Solution-phase studies. a) Photoswitchable pseudorotaxane formation. b) UV/Vis spectra of the axle in CH_2Cl_2 in *cis* and *trans* configuration. c) Reversible photoswitching in CH_2Cl_2, tested by alternating irradiation at λ_1 = 365 nm and λ_2 = 470 for 10 min in each step. d) NMR analysis (298 K, $CDCl_3$) of pseudorotaxane switching. I: TLM. II: TLM + axle, 1:1. III: TLM + axle after 10 min irradiation at λ_1. IV: TLM + axle after 24 h in the dark at r.t.

NMR spectroscopy was applied to gain structural information and evidence for switchable pseudorotaxane formation. It revealed that the amide protons of the macrocycle only undergo a small shift upon addition of one equivalent *trans* axle (Figure 67d, I to II). After 10 minutes

irradiation at λ_1 (Figure 67d, III), a second set of signals for the *cis* configuration appears with a ratio of *cis*- to *trans* of approx. 2:1. Due to hydrogen bonding, the macrocycle protons **a** and **b** are now significantly shifted downfield and the diketopiperazine protons **c**, **d**, and **e** are shifted upfield as they are shielded by the macrocycle aromatics. This clearly confirms the pseudorotaxane formation of the axle in its *cis* configuration. Equilibrium in the dark for 24 h yielded a spectrum equal to the initial one which shows reversible binding. NMR titrations provided binding constants of <15 M^{-1} for the *trans* and 1,650 ± 165 M^{-1} for the *cis* configuration. After the successful demonstration of reversible pseudorotaxane formation, the concept was transferred to well-established macrocycle multilayers and with that to surface. Multilayers were obtained by layer-by-layer self-assembly with pyridine-terminated **PDS** on glass and Pd^{II} and Fe^{II} ions as metal connectors like it was shown in chapter 4.4.

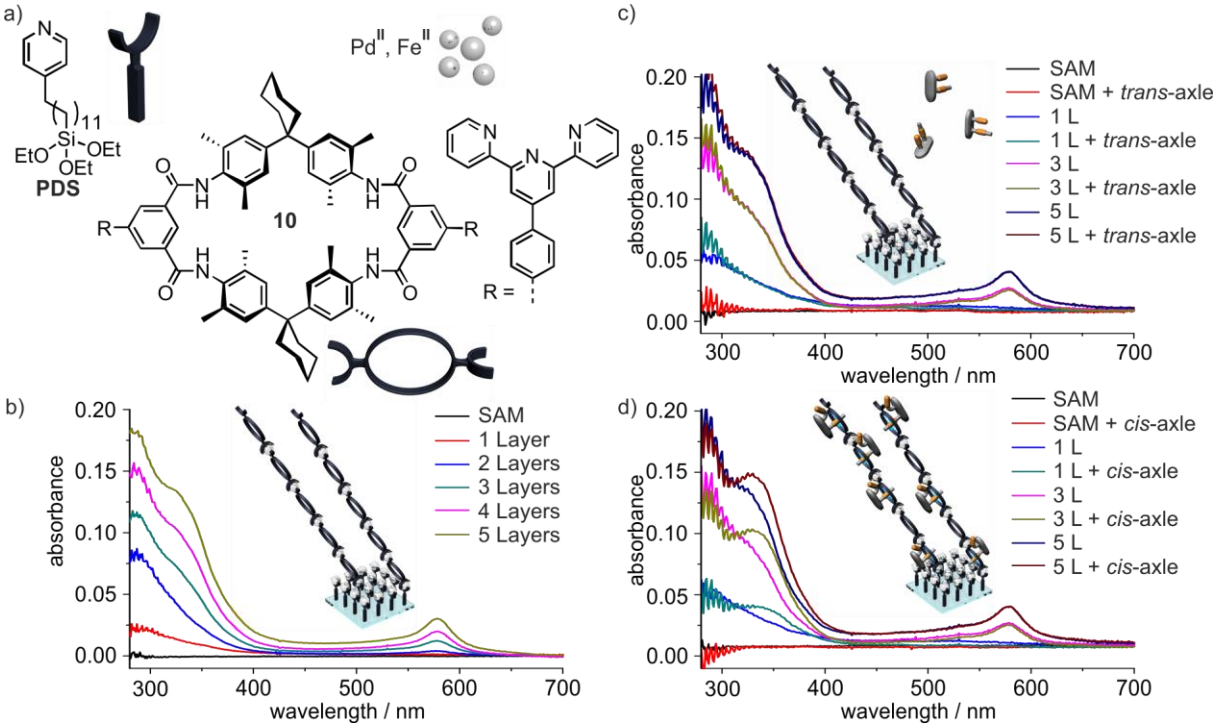

Figure 68. Transmission-UV/Vis investigations. a) Di-terpyridine-TLM, PDS-SAM, metal ions used for the self-assembly of macrocycle multilayers. b) Transmission-UV/Vis spectra showing multilayer deposition. c) UV/Vis spectra of surfaces before and after immersion in *trans* axle solution. d) UV-Vis spectra of surfaces before and after immersion in *cis* axle solution.

First, transmission-UV/Vis experiments were conducted in order to follow the multilayer assembly as well as the binding of the axle to it. Multilayer assembly was confirmed by the measurement of UV/Vis spectra after each macrocycle-layer deposition. To see whether the axle binds to the multilayer, the one-, three- and five-layered systems were investigated and the pristine SAM was taken as control. The surfaces were immersed into a solution of the axle either untreated to show the binding behavior of the axle in its *trans* configuration or under

constant irradiation at λ_1 to do the same for the *cis* configuration. Subsequent, immersion of the surfaces into CH_2Cl_2 for 10 minutes ensured that no unspecifically bound material remained. The then recorded UV/Vis spectra revealed different behavior for trans and cis: The spectra of the surfaces with one, three and five layers of TLM showed a substantial increase of the absorption around 350 nm when immersed in *cis* solution, while no change was observed for the same surfaces immersed in *trans* solution. This indicates that the axle could be deposited in its *cis* configuration. Interestingly, the axle does not – unlike the squarain axle – bind to the lower layers when more than three macrocycle layers are deposited as revealed by the difference spectra. This can be explained by the different structures of the two guests: While the squarain has a somewhat linear structure and is therefore able to slip through the multilayer into the macrocycle cavities, the axle described here is stoppered at one end through the xanthene backbone which makes it sterically demanding for it to diffuse through the multilayer.

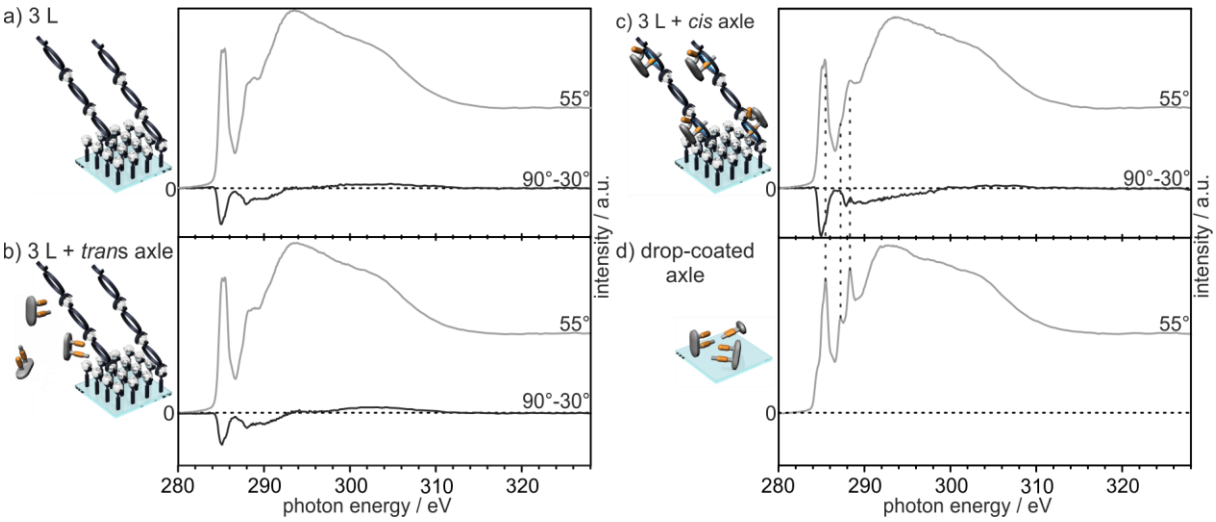

Figure 69. C K-edge NEXAFS spectra acquired at an incidence angle of the linearly polarized synchrotron light of (grey) 55° and (black) the difference between the spectra acquired at 90° and 30° of (a) a three-layered macrocycle multilayer, (b) the multilayer treated with a solution of *trans* axle, (c) the multilayer treated with a solution of *cis* axle, and (d) the drop-coated axle.

The surfaces with three layers of macrocycles were also analyzed by means of XPS and NEXAFS. While XPS just showed a small hint for the presence of axle by an altered ratio of different N 1s signals, NEXAFS displayed some interesting results. By comparing the N-K edge NEXAFS-spectra of the pristine multilayer, multilayers either treated with a solution of trans or cis axle-configuration, and the drop-coated axle, it was concluded that the *cis* axle was indeed deposited to the multilayer. Although, there is a substantial overlap between the signals present, the spectra clearly support the results gained from UV/Vis studies. Angle-dependent C K-edge NEXAFS spectra provide a more detailed picture (Figure 69). The spectra of the pristine macrocycle multilayer clearly exhibit a linear dichroism, showing that a preferential

orientation is present. The multilayer treated with the solution of trans axle shows the same signals as well as a similar dichroism, indicating that no incorporation of axle is taking place. In contrast, the spectrum of the multilayer treated with a solution of cis axle exhibits two peaks that are superimposed by two new signals. The spectrum of the drop-coated axle shows that these signals are due to the additional axle on the surface. Moreover, the increased linear dichroism confirms a higher order in the multilayer and therefore indicates an incorporation of the axle into the cavities of the macrocycle.

Finally, the reversibility of the pseudorotaxane-formation on the surface was tested by irradiating the surfaces with bound axle at λ_2 which showed no changes in the UV/Vis spectra and therefore indicating that not cis-trans isomerism is taking place. Immersing the surfaces in CH_2Cl_2 for 24 h also had no effect. When the surfaces are immersed in DMF, which is a strong hydrogen-bond competitor, the guest could be removed from the multilayers.

4.6.2. Personal Contribution to this Publication

Felix B. Schwarz was responsible for the conceptual development and wrote the article. Together with J. Ole Kaufmann, he synthesized the axle. He also conducted the solution-phase as well as transmission-UV/Vis studies, MM2 calculations, and crystallized the axle. The author synthesized the macrocycles, conducted the NEXAFS and XPS measurements, interpreted the data and helped with the conceptual development as well as writing the article. Andreas Lippitz helped with NEXAFS and XPS measurements. Rakesh Putreddy measured the crystal and calculated the structure. All authors contributed to the final version of the manuscript.

4.7. Coupled Molecular Switching Processes in Ordered Mono- and Multilayers of Stimulus-Responsive Rotaxanes on Gold Surfaces

Thomas Heinrich, Christoph H.-H. Traulsen, Markus Holzweber, Sebastian Richter, Valentin Kunz, Sarah K. Kastner, Sven O. Krabbenborg, Jurriaan Huskens, Wolfgang E. S. Unger, and Christoph A. Schalley

J. Am. Chem. Soc. **2015**, 137, 4382–4390.

Submitted 12 December 2014, published 17 March 2015.

The journal article is electronically available (http://dx.doi.org/10.1021/ja512654d).

4.7.1. Summary of the Publication

The basis of this work is the idea that functional multilayers of molecules in ordered arrays can easily be fabricated on surfaces through layer-by-layer self-assembly. Moreover, the well-controlled axle shuttling of stimuli-responsive, ordered rotaxanes is an excellent candidate for a coupled mechanical motion. The present work demonstrates the successful deposition of ordered mono- and multilayers of chemically switchable rotaxanes on gold surfaces. In order to transfer the switching process in solution of the well-studied rotaxane to surfaces, it is necessary to functionalize the rotaxane with terpyridines (**Rot6**) similar to the previous reported macrocycle (**MC3**) or an alkyne function (**Rot3**). The well-studied diketopiperazine is used as an axle. When triazole-moieties are attached to the central axle-piece, the addition of chloride induces a translation of the macrocycle from the diketopiperazine to the adjacent triazoles. The macrocycle then shuttles from one triazole to another. When chloride is removed, the macrocycle translates back into its initial state (see chapter 3.3). ^{1}H NMR studies revealed that chloride addition to the rotaxane **Rot6** in $CDCl_3$ induces significant signal shifts of hydrogens on both the axle and the macrocycle (Figure 70). This strongly indicates that the proposed translocation of the macrocycle indeed takes place.

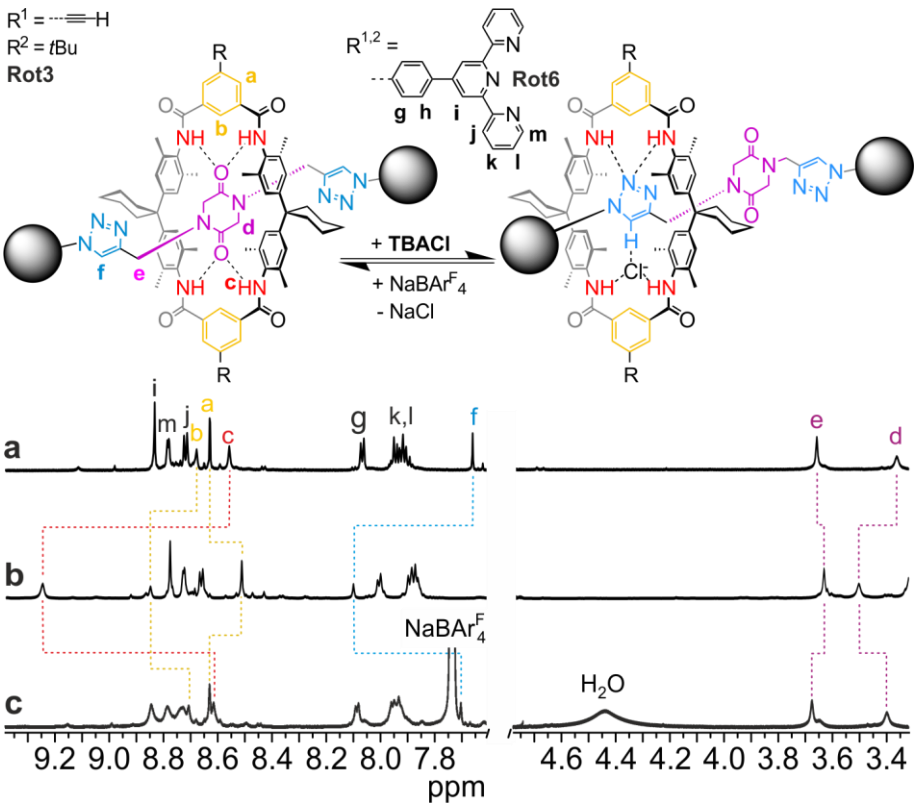

Figure 70. ^{1}H NMR data confirming chloridemediated switching of the rotaxane Rot6. Top: Chloride-induced switching within the rotaxane. Bottom: partial ^{1}H NMR spectra (4 mM, $CDCl_3$, 298 K) of (a) the rotaxane before addition of 1 equiv of tetrabutylammonium chloride ((TBA)Cl), (c) rotaxane Rot6 after addition of 1 equiv of (TBA)Cl, and (c) Rot6 after chloride removal by precipitation of NaCl with 1 equiv of sodium tetrakis(3,5-bis(trifluoromethyl)phenyl)borate ($NaBArF_4$).

The alkyne- and *tert*-butyl-substituted roaxane **Rot3** was deposited onto the azide-terminated monolayer of bis(11-azidoundecyl) disulfide **AUD** by CuAAC (Figure 71a). **Rot6** however is deposited into mono- and mulitlayers by a coordination-based layer-by-layer self-assembly process onto a rigid template functionalized with pyridine (**PST**) or onto a flexible, terpyridine-functionalized template with diluted coordination sites (**TDT**/**DT** 1/3). The connecting metal layer is composed of tetrahedrally coordinating Pd^{II}-ions for **PST** or octahedrally coordinating Fe^{II}-ions in case of the **TDT**/**DT**-SAM (Figure 71b).

Mono- and multilayer formation could be shown by XPS, transmission-UV/Vis and AFM measurements. Similar to the previous studies dealing with the macrocycle multilayers, the C 1s/Au $4f_{7/2}$ peak-area ratios showed an increase after every deposition step which is due to the attenuation of the gold signal by the increasing organic layer. Analogous, the multilayer formation was followed by transmission-UV/Vis spectroscopy. All bands initially observed in the solution spectrum of the complex reappeared in the spectra of each layer deposition and the absorption also increases in a linear fashion, which indicates that a constant amount of rotaxane was deposited with every deposition step. When a micropatterned surface is investigated by AFM, the thickness of one rotaxane layer was determined to be ~1.6 nm which very

well matches the layer thickness of the macrocycle multilayers where the macrocycles have a tilting angle of ca. 35° (see chapter 4.1). In conclusion, the rotaxanes behave very similarly to the macrocycles when deposited into multilayer on the surface with a similar tilting-angle. One additional observation is worth noticing: The C 1s/Au $4f_{7/2}$ peak area ratios of the rotaxane multilayer on **PST** have much greater values than those of the rotaxane multilayer on **TDT**/**DT**. This indicates that the rotaxanes are more diluted on the **TDT**/**DT**-template and that close packing is not present in this case.

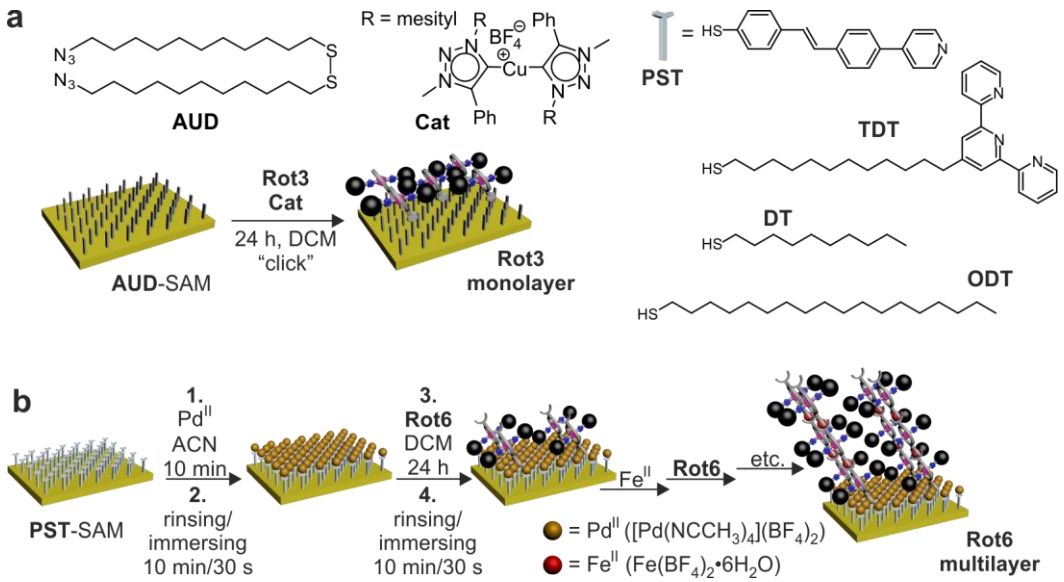

Figure 71. Fabrication of mono- and multilayers of switchable rotaxanes. (a) Monolayers of covalently fixed Rot3 are made by first depositing an azide-terminated SAM of AUD onto a gold surface. Afterward, the acetylene-substituted rotaxane Rot3 is "clicked" to the azides. (b) On a (ter-)pyridine-terminated SAM, Pd^{II}-ions are deposited and then mediate the connection to the first layer of Rot6 deposited from dichloromethane solution. Subsequently, this monolayer can be converted into multilayers by an alternating deposition of Fe^{II}- ions and Rot6.

The on-surface switching process was initially investigated with contact-angle measurements. These revealed that chloride addition to the mono- and multilayers leads to a decrease of ~20° for all rotaxane layers which is reversed when the chloride ions are removed. In order to rule out that this observation was just due to the presence of chloride-ions, the same experiment was done with a macrocycle multilayer. Here, just a small angle change of ~3° was observed which indicates that the polarity change is due to an axle-translocation in the rotaxane multilayers. The observed linear dichroism effects in angle-resolved NEXAFS spectra delivered evidence for a reversible switching of the rotaxanes bound to the surface in a coupled manner. Such a concerted switching process is observed only when the surfaces are well packed, while less densely packed surfaces lacking lateral order do not exhibit such effects. In detail, the mono- and multilayers are switchable between two ordered state when deposited on the rigid,

pyridine-terminated template. When deposited onto the flexible template with more diluted terpyridine binding-sites, the rotaxane multilayers do not exhibit a linear dichroism before and after chloride addition. In conclusion, no coupled switching takes place in this multilayer. To show that the observed orientational effects are not due to the incorporation of the counterion tetrabutylammonium (TBA), the switching was repeated with a smaller counterion tetramethylammonium (TMA). These experiments showed a similar linear-dichroism and therefore also orientational behavior. The alkyne-functionalized rotaxane **Rot3** clicked to the surface exhibits a linear dichroism similar to the one of **Rot6** on **PST**. When chloride is added, this effect almost completely vanishes but is retained after chloride is removed from the monolayer. Consequently, this rotaxane also exhibits a coupled switching.

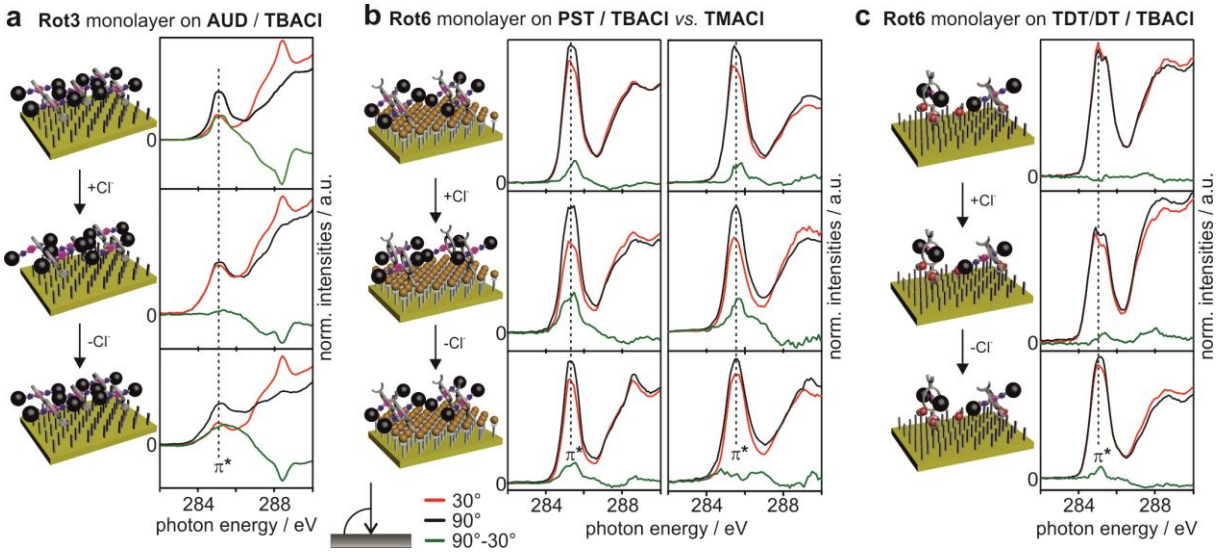

Figure 72. Investigation of the chloride-induced switching process. Angle-resolved NEXAFS spectra of (a) a Rot3 monolayer on AUD and (b) a Rot6 monolayer on PST. Left: Switching induced by (TBA)Cl; right: Switching induced by (TMA)Cl). (c) NEXAFS of a Rot6 monolayer on TDT/DT (1:3). In each case, the NEXAFS results obtained for the pristine layer, that after chloride addition, and that after chloride removal with $NaBArF_4$ are shown (top to bottom). Red and black lines represent the NEXAFS spectra obtained at 30° and 90° angles of the incident synchrotron light beam, respectively. Difference spectra are shown in green.

Finally, the triple layer of **Rot6** on **PST** again exhibits linear dichroism effects on the π* resonance that change with chloride addition and removal. The concept of concerted switching observed for the **PST-Rot6** monolayer is consequently transferable to multilayers of **Rot6** on **PST** as well.

4.7.2. Personal Contribution to this Publication

The author conceived the synthethic route and synthesized **MC1**, **MC2**, **MC3**, **Rot5**, **Rot6**, and all needed precursors. In cooperation with Sarah K. Kastner, the author also synthesized **Rot1**, **Rot2** and **Rot3**. Furthermore, the author deposited the mono- and multilayers of the rotaxanes,

and conducted all XPS, NEXAFS, UV/Vis, as well as contact angle experiments and interpreted the data. Christoph H.-H. Traulsen did the µCP approach in cooperation with Sven O. Krabbenborg and analyzed the samples by AFM. Markus Holzweber measured the ToF-SIMS images. Sebastian Richter synthesized the SAM molecules and Valentin Kunz synthesized **Rot4**. The author was responsible for the conceptual development and the coordination of the project as well as conceiving and writing the article. All authors contributed to the final version of the manuscript.

5. Conclusion and Outlook

In the course of this thesis, mono- and multilayers of different supramolecules were obtained as well as analyzed and their behavior upon the addition of suitable binding partners or an external stimulus was investigated. It is particularly noteworthy that it could be shown that switchable rotaxanes were deposited onto solid supports and switched in a coupled manner between two well-ordered states when treated with an external stimulus such as the addition of chloride ions.

As a part of a greater project, this work has first focused on the improvement and the assurance of the surface analysis by transmission-UV/Vis, XP, and NEXAFS spectroscopy as well as ToF-SIMS. Based on earlier results that resulted in the generation of suitable monolayers, the deposition of nanometer-sized macrocycles in multilayers was investigated with transmission UV/Vis, XPS and NEXAFS which confirmed a regular growth and also a preferential-orientation. Then, (PCA assisted) ToF-SIMS was established as an analytical tool to ensure a high-quality deposition of SAMs and the already established macrocycle multilayers due to its high sensitivity to impurities as well as a survey of the point-to-point reproducibility of a certain sample set. Furthermore, a (sequence) programmable multilayer with different metals as well as functionalized macrocycle was developed and investigated with XPS and ToF-SIMS. It could be shown that the metals are discretely distributed in the multilayer which confirmed the sequential multilayer assembly which can act as a proof-of-principle for the fabrication of multilayers comprising differently addressable rotaxanes. Additionally, angle-resolved NEXAFS measurements provided an indication for their preferential orientation. A reversible host-guest complex formation was also successfully carried out in mono- and multilayers of different supramolecules both covalently and coordinatively bound to the surface. This proved that these assemblies are in principle available for an external stimulus. It could be also shown that the macrocycle-multilayer is available for pseudorotaxane or host-guest formation all the way down to the lowest layer. By introducing roughness to the multilayer after the incorporation of nanoparticles, the uptake of guests could be increased due to a decrease of order. Pseudorotaxane-formation experiments with photoswitchable axles were also successful and showed even an increase of preferential orientation after guest incorporation.

These studies delivered the basis for the subsequent part of the project, where rotaxanes, that exhibit axle translocation in the wheel to the presence of chloride, were synthesized, effectively deposited on gold substrates, and switched. It was not only shown that the rotaxanes are ordered in the multilayer but also that chloride-addition induces the generation of an even more ordered state. Subsequent chloride removal leads to the recovery of the initial order – i.e. the structural change is reversible. Various control experiments and the comparison between dif-

ferent layers led to the conclusion that the occurring electronic (structural) effects can be ascribed to the axle translocation in the wheel and are not from other possible origins like the incorporation of the chloride counterion. Furthermore, the significant change of surface wettability upon chloride addition is only present for the rotaxane but not the macrocycle multilayers which indicates that the change in hydrophobicity is not solely due to the presence of the applied salt. Consequently, the switching of the applied rotaxane has successfully been transferred from the solution to the surface.

In order to generate a directional switching of mechanically interlocked molecules in the future, one key aspect has to be taken from this work: A dense packing of the rotaxanes induces order and a coupling between the individual switches. It also results in limited degrees of freedom for the axles of each rotaxane through spatial constraints caused by the next neighbors. The switching of the rotaxanes in the multilayer is therefore probably able to deliver a unidirectional switching process that can later be harnessed to produce a macroscopic effect such as lifting/transport of a cargo caused by the tilting-up of the rotaxanes in a coupled fashion. However, a perfectly simultaneous switching of all rotaxanes in a domain is unlikely, because the overall barrier would be expected to be very high. Therefore, the switching process presumably follows a nucleation/growth mechanism. To overcome the probably high barrier of synchronized switching, one could think of the introduction of side chains or stoppers with opposing properties such as dipoles, hydrogen-bond donors/acceptors or electron-poor/electron-rich aromatic systems. In a very recent study, Hla and coworkers could show that the rotation of a molecular 2D-assembly can be coordinated and synchronized by the incorporation of a dipole into a hexagonal rotor that is deposited onto a gold surface leading to potential application in, for example, information transport on the mesoscale.[143] If the axle can be equipped with the mentioned oppositely constituted molecular units, the switching can also be coordinated and synchronized. Furthermore, the hydrogen-bonding moieties used by Giuseppone and coworkers for their self-assembled supramolecular, muscle-like fibers can be employed as stopper units to connect the axles with each other.[144] This will probably lead to an amplification of the structural change during the switching process and therefore to an increase of its directionality.

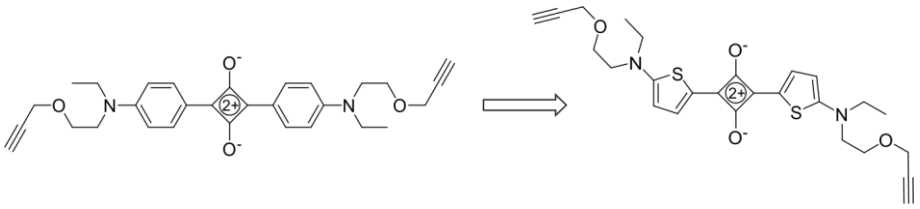

Scheme 5. Suggested modification of the squaraine unit in order to gain more stability.

For an easier analysis and even an optical read-out of the switching, a rotaxane with a squaraine dye as described in chapter 3.3 was employed. However, stability and synthetic

issues made it impossible to deposit such a rotaxane on the surface. The squaraine dye proposed now contains two electron-donating 2-aminothiophene units, which diminish the electrophilicity of the central C_4O_2 core so that it resists nucleophilic attacks by aqueous media.[145] This was a major issue before as water was shown to be always present in the course of the mono- and multilayer fabrication. Such a rotaxane shall be deposited by the already employed click approach as the diiodo-functionalized macrocycle used for the rotaxanes-synthesis in this work is not soluble enough to form a complex with the squarain-axle.

Additionally, switchable rotaxanes are supposed to be used that only possess two distinct binding sites, so that the directionality of the surface-bound switching is facilitated and can be better determined. This was already done with a diketopiperazine rotaxane that is shown in Scheme 6 (right). When it is deposited onto solid support in multilayers, it however showed no structural change upon chloride addition. We ascribe this to the flexible and rather long linker between the diketopiperazine and the stopper or triazole which increases the degrees of freedom of the rotaxanes and therefore diminishes probably occurring structural effects. Consequently, an analogous rotaxane was designed that has a shorter as well as more rigid linker (Scheme 6, middle). This should lead to a reduction of the degrees of freedom, and therefore to an amplification of the order as well as switching directionality.

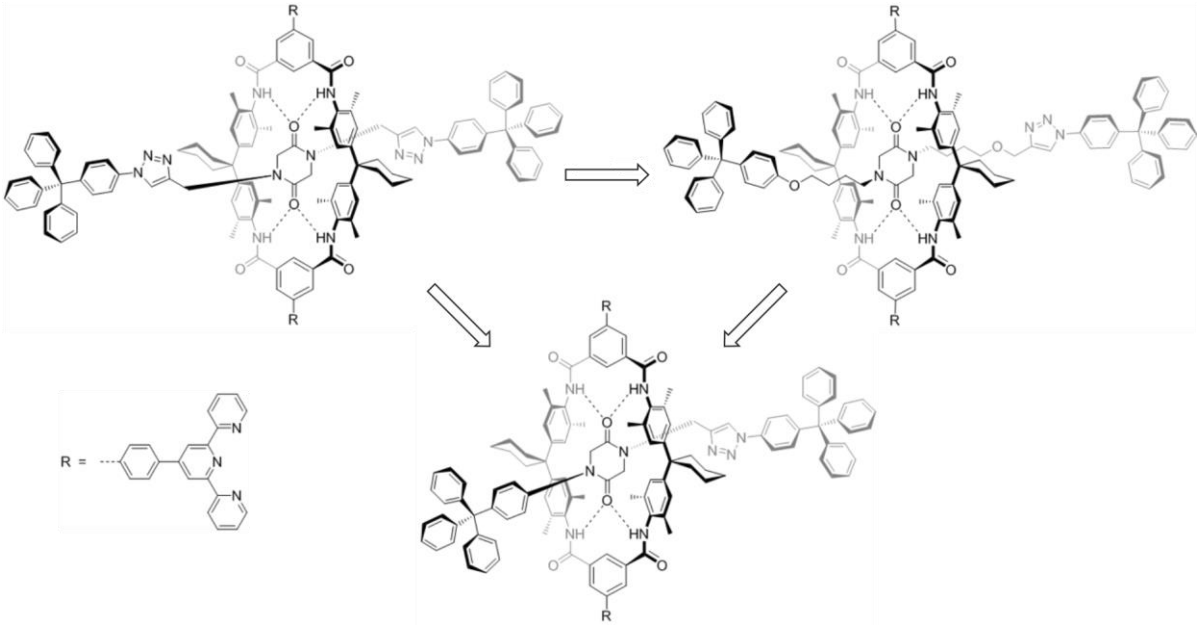

Scheme 6. Proposed modification of the rotaxane used in this work in order to gain a direction within the molecule.

The conformational change of these rotaxanes is however rather small which also probably leads to a smaller effect on the macroscale. Thus, rotaxanes should be designed that have a larger conformational change which can be realized by the incorporation of longer but rigid linkers or even a poly- or oligomerized axle.

Obviously, the stimulus should also be changed to a ‘noninvasive’ one – i.e. the chemical stimulus leads to more and more contaminations inside of the multilayers and therefore to a probable rearrangement of the switches. This could be overcome by applying a photochemical – analogous to the pseudorotaxane studies in the most recent publication – or an electrochemical stimulus. In particular, redox-switchable crown-ether rotaxanes can be incorporated as organic linkers in multilayers in order to use them as functional electrodes and potential data storage devices and to translate the molecular motion from the nanoscale to macroscopic property changes. Additionally, photoswitchable rotaxanes, that contain the tetralactam macrocycle, have optical properties, and can be deposited into a monolayer on the surface, have already been designed and synthesized.

To further reduce the degrees of freedom that the rotaxanes have to assemble, the cross-linking of the metal-connector should also be considered. This will not only lead to a more determined assembly of the switches in the multilayers and therefore probably a higher order but will also pave the way for an alternative analytical method which is namely X-ray diffraction (XRD) which was not applicable for the multilayers produced in this work. The in this manner fabricated SurMOFs are particularly interesting. They represent highly stable scaffolds where the employed switches can evenly be distributed throughout a regular grid that can easily be adjusted to the length of the axle or macrocycle molecule enabling not just a coupled but also synchronous switching.

However, even if the proposed seminal steps help to improve the switching and we gain a certain simultaneity and alignment of the molecular motion, it does not certainly generate a directional movement displayed by a macroscopic effect. The last examples from Leigh and Stoddart, in which rotaxane switches are incorporated into larger arrays that give a macroscopic effect, have been reported more than a decade ago and the molecular motors, rotors, switches, and machines reported in recent years are not more than rudimentary. This raises the question whether a molecular motion is able to have an impact on a macroscopic level at all and therefore whether molecular machines are able to deliver the desired applications. In detail, the stability as well as the mechanical performance is limited, which prevents them to fulfill a useful task. The community has therefore reached a crossroads. It will be important to decide whether seminal steps to provide improvements to the switching process or complete new approaches have to be considered. This will be the crucial part of future integrations of molecular machines into larger devices. This work can deliver a substantial contribution in understanding the factors that direct the switching or mechanical processes inside the desired devices and therefore should help in finding an answer to the questions that arise in the future.

6. References

[1] R. Feynman, *Sci. Eng.* **1960**, *23-36*, 22.

[2] S. Erbas-Cakmak, D. A. Leigh, C. T. McTernan, A. L. Nussbaumer, *Chem. Rev.* **2015**, *115*, 10081-10206.

[3] S. Kassem, A. T. L. Lee, D. A. Leigh, A. Markevicius, J. Solà, *Nat. Chem.* **2016**, *8*, 138-143.

[4] T.-G. Cha, J. Pan, H. Chen, J. Salgado, X. Li, C. Mao, J. H. Choi, *Nat. Nanotechnol.* **2014**, *9*, 39-43.

[5] A. Coskun, M. Banaszak, R. D. Astumian, J. F. Stoddart, B. A. Grzybowski, *Chem. Soc. Rev.* **2012**, *41*, 19-30.

[6] a) B. K. Juluri, A. S. Kumar, Y. Liu, T. Ye, Y.-W. Yang, A. H. Flood, L. Fang, J. F. Stoddart, P. S. Weiss, T. J. Huang, *ACS Nano* **2009**, *3*, 291-300; b) T. Ye, A. S. Kumar, S. Saha, T. Takami, T. J. Huang, J. F. Stoddart, P. S. Weiss, *ACS Nano* **2010**, *4*, 3697-3701.

[7] a) A. Coskun, M. Hmadeh, G. Barin, F. Gándara, Q. Li, E. Choi, N. L. Strutt, D. B. Cordes, A. M. Z. Slawin, J. F. Stoddart, J.-P. Sauvage, O. M. Yaghi, *Angew. Chem. Int. Ed.* **2012**, *51*, 2160-2163; b) Q. Li, C.-H. Sue, S. Basu, A. K. Shveyd, W. Zhang, G. Barin, L. Fang, A. A. Sarjeant, J. F. Stoddart, O. M. Yaghi, *Angew. Chem. Int. Ed.* **2010**, *49*, 6751-6755.

[8] C. A. Schalley, *Analytical Methods in Supramolecular Chemistry,* 2 ed., VCH, Weinheim, **2007**.

[9] D. J. Cram, J. M. Cram, *Science* **1974**, *183*, 803-809.

[10] W. Saenger, J. Jacob, K. Gessler, T. Steiner, D. Hoffmann, H. Sanbe, K. Koizumi, S. M. Smith, T. Takaha, *Chem. Rev.* **1998**, *98*, 1787-1802.

[11] a) V. Aucagne, J. Berná, J. D. Crowley, S. M. Goldup, K. D. Hänni, D. A. Leigh, P. J. Lusby, V. E. Ronaldson, A. M. Z. Slawin, A. Viterisi, D. B. Walker, *J. Am. Chem. Soc.* **2007**, *129*, 11950-11963; b) M. S. Vickers, P. D. Beer, *Chem. Soc. Rev.* **2007**, *36*, 211-225.

[12] a) F. Vögtle, T. Dünnwald, T. Schmidt, *Acc. Chem. Res.* **1996**, *29*, 451-460; b) F. Vögtle, S. Meier, R. Hoss, *Angew. Chem. Int. Ed. Engl.* **1992**, *31*, 1619-1622.

[13] W. Jiang, H. D. F. Winkler, C. A. Schalley, *J. Am. Chem. Soc.* **2008**, *130*, 13852-13853.

[14] P. Ghosh, O. Mermagen, C. A. Schalley, *Chem. Commun.* **2002**, *38*, 2628-2629.

[15] C. A. Schalley, T. Weilandt, J. Brüggemann, F. Vögtle, *Top. Curr. Chem.* **2004**, *248*, 285-295.

[16] C. A. Schalley, K. Beizai, F. Vögtle, *Acc. Chem. Res.* **2001**, *34*, 465-476.

[17] G. M. Hübner, J. Gläser, C. Seel, F. Vögtle, *Angew. Chem. Int. Ed.* **1999**, *38*, 383-386.

[18] S. S. Zhu, M. Nieger, J. Daniels, T. Felder, I. Kossev, T. Schmidt, M. Sokolowski, F. Vögtle, C. A. Schalley, *Chem. Eur. J.* **2009**, *15*, 5040-5046.

[19] a) I. Kossev, T. Felder, C. A. Schalley, F. Vögtle, M. Sokolowski, *Top. Curr. Chem.* **2009**, *127*, 235-245; b) I. Kossev, W. Reckien, B. Kirchner, T. Felder, M. Nieger, C. A. Schalley, F. Vögtle, M. Sokolowski, *Adv. Funct. Mater.* **2007**, *17*, 513-519; c) I. Kossev, S. Fahrenholz, A. Görling, W. Hieringer, C. A. Schalley, M. Sokolowski, *Synthetic Met.* **2004**, *147*, 159-164.

[20] a) B. Baytekin, S. S. Zhu, B. Brusilowskij, J. Illigen, J. Ranta, J. Huuskonen, L. Russo, K. Rissanen, L. Kaufmann, C. A. Schalley, *Chem. Eur. J.* **2008**, *14*, 10012-10028; b) E. V. Dzyuba, B. Baytekin, D. Sattler, C. A. Schalley, *Eur. J. Org. Chem.* **2012**, 1171-1178.

[21] J. Broichhagen, T. Podewin, H. Meyer-Berg, Y. von Ohlen, N. R. Johnston, B. J. Jones, S. R. Bloom, G. A. Rutter, A. Hoffmann-Röder, D. J. Hodson, D. Trauner, *Angew. Chem. Int. Ed.* **2015**, *54*, 15565-15569.

[22] M. Borowiak, W. Nahaboo, M. Reynders, K. Nekolla, P. Jalinot, J. Hasserodt, M. Rehberg, M. Delattre, S. Zahler, A. Vollmar, D. Trauner, O. Thorn-Seshold, *Cell* **2015**, *162*, 403-411.

[23] J. Broichhagen, J. A. Frank, D. Trauner, *Acc. Chem. Res.* **2015**, *48*, 1947-1960.
[24] H. M. D. Bandara, S. C. Burdette, *Chem. Soc. Rev.* **2012**, *41*, 1809-1825.
[25] a) N. Koumura, R. W. J. Zijlstra, R. A. van Delden, N. Harada, B. L. Feringa, *Nature* **1999**, *401*, 152-155; b) B. L. Feringa, *Acc. Chem. Res.* **2001**, *34*, 504-513.
[26] a) J. D. Badjić, V. Balzani, A. Credi, S. Silvi, J. F. Stoddart, *Science* **2004**, *303*, 1845-1849; b) M. Xue, Y. Yang, X. Chi, X. Yan, F. Huang, *Chem. Rev.* **2015**, *115*, 7398-7501.
[27] A. M. Brouwer, C. Frochot, F. G. Gatti, D. A. Leigh, L. c. Mottier, F. Paolucci, S. Roffia, G. W. H. Wurpel, *Science* **2001**, *291*, 2124-2128.
[28] P. L. Anelli, N. Spencer, J. F. Stoddart, *J. Am. Chem. Soc.* **1991**, *113*, 5131-5133.
[29] R. A. Bissell, E. Cordova, A. E. Kaifer, J. F. Stoddart, *Nature* **1994**, *369*, 133-137.
[30] A. Altieri, G. Bottari, F. Dehez, D. A. Leigh, J. K. Y. Wong, F. Zerbetto, *Angew. Chem. Int. Ed.* **2003**, *42*, 2296-2300.
[31] J. J. Gassensmith, J. M. Baumes, B. D. Smith, *Chem. Commun.* **2009**, *45*, 6329-6338.
[32] a) J. J. Gassensmith, S. Matthys, J.-J. Lee, A. Wojcik, P. V. Kamat, B. D. Smith, *Chem. Eur. J.* **2010**, *16*, 2916-2921; b) J. J. Gassensmith, L. Barr, J. M. Baumes, A. Paek, A. Nguyen, B. D. Smith, *Org. Lett.* **2008**, *10*, 3343-3346.
[33] E. V. Dzyuba, L. Kaufmann, N. L. Löw, A. K. Meyer, H. D. F. Winkler, K. Rissanen, C. A. Schalley, *Org. Lett.* **2011**, *13*, 4838-4841.
[34] a) B. Lewandowski, G. De Bo, J. W. Ward, M. Papmeyer, S. Kuschel, M. J. Aldegunde, P. M. E. Gramlich, D. Heckmann, S. M. Goldup, D. M. D'Souza, A. E. Fernandes, D. A. Leigh, *Science* **2013**, *339*, 189-193; b) G. De Bo, S. Kuschel, D. A. Leigh, B. Lewandowski, M. Papmeyer, J. W. Ward, *J. Am. Chem. Soc.* **2014**, *136*, 5811-5814.
[35] M. A. Watson, S. L. Cockroft, *Chem. Soc. Rev.* **2016**.
[36] C. Cheng, P. R. McGonigal, S. T. Schneebeli, H. Li, N. A. Vermeulen, C. Ke, J. F. Stoddart, *Nat. Nanotechnol.* **2015**, *10*, 547-553.
[37] G. Ragazzon, M. Baroncini, S. Silvi, M. Venturi, A. Credi, *Nat Nano* **2015**, *10*, 70-75.
[38] R. G. Nuzzo, D. L. Allara, *J. Am. Chem. Soc.* **1983**, *105*, 4481-4483.
[39] C. Vericat, M. E. Vela, G. Benitez, P. Carro, R. C. Salvarezza, *Chem. Soc. Rev.* **2010**, *39*, 1805-1834.
[40] a) O. Azzaroni, M. H. Fonticelli, G. Benítez, P. L. Schilardi, R. Gago, I. Caretti, L. Vázquez, R. C. Salvarezza, *Adv. Mater.* **2004**, *16*, 405-409; b) R. H. Terrill, T. A. Postlethwaite, C.-h. Chen, C.-D. Poon, A. Terzis, A. Chen, J. E. Hutchison, M. R. Clark, G. Wignall, *J. Am. Chem. Soc.* **1995**, *117*, 12537-12548; c) B. R. Martin, D. J. Dermody, B. D. Reiss, M. Fang, L. A. Lyon, M. J. Natan, T. E. Mallouk, *Adv. Mater.* **1999**, *11*, 1021-1025.
[41] a) J. C. Love, L. A. Estroff, J. K. Kriebel, R. G. Nuzzo, G. M. Whitesides, *Chem. Rev.* **2005**, *105*, 1103-1170; b) U. Drechsler, B. Erdogan, V. M. Rotello, *Chem. Eur. J.* **2004**, *10*, 5570-5579.
[42] a) O. Azzaroni, M. Cipollone, M. E. Vela, R. C. Salvarezza, *Langmuir* **2001**, *17*, 1483-1487; b) G. Brunoro, A. Frignani, A. Colledan, C. Chiavari, *Corros. Sci.* **2003**, *45*, 2219-2231; c) C. M. Whelan, M. Kinsella, L. Carbonell, H. Meng Ho, K. Maex, *Microelectron. Eng.* **2003**, *70*, 551-557.
[43] Y. Wang, Y. Zhou, J. Sokolov, B. Rigas, K. Levon, M. Rafailovich, *Biosens. Bioelectron.* **2008**, *24*, 162-166.
[44] T. J. Huang, B. Brough, C.-M. Ho, Y. Liu, A. H. Flood, P. A. Bonvallet, H.-R. Tseng, J. F. Stoddart, M. Baller, S. Magonov, *Appl. Phys. Lett.* **2004**, *85*, 5391-5393.
[45] a) B. D. Gates, Q. Xu, M. Stewart, D. Ryan, C. G. Willson, G. M. Whitesides, *Chem. Rev.* **2005**, *105*, 1171-1196; b) J. A. Rogers, R. G. Nuzzo, *Mater. Today* **2005**, *8*, 50-56.
[46] a) D. Xiang, X. Wang, C. Jia, T. Lee, X. Guo, *Chem. Rev.* **2016**, *116*, 4318-4440; b) J. M. Tour, *Acc. Chem. Res.* **2000**, *33*, 791-804; c) A. Lio, D. H. Charych, M. Salmeron, *J. Phys. Chem. B* **1997**, *101*, 3800-3805; d) T. Sugawara, M. M. Matsushita, *J. Mater. Chem.* **2009**, *19*, 1738-1753; e) L. A. Bumm, J. J. Arnold, M. T. Cygan, T. D. Dunbar,

T. P. Burgin, L. Jones, D. L. Allara, J. M. Tour, P. S. Weiss, *Science* **1996**, *271*, 1705-1707.
[47] a) R. Levicky, T. M. Herne, M. J. Tarlov, S. K. Satija, *J. Am. Chem. Soc.* **1998**, *120*, 9787-9792; b) B. Bonanni, A. R. Bizzarri, S. Cannistraro, *J. Phys. Chem. B* **2006**, *110*, 14574-14580; c) E. T. Castellana, P. S. Cremer, *Surf. Sci. Rep.* **2006**, *61*, 429-444.
[48] M. Brust, M. Walker, D. Bethell, D. J. Schiffrin, R. Whyman, *J. Chem. Soc., Chem. Commun.* **1994**, 801-802.
[49] T. Shimizu, T. Teranishi, S. Hasegawa, M. Miyake, *J. Phys. Chem. B* **2003**, *107*, 2719-2724.
[50] G. F. Paciotti, L. Myer, D. Weinreich, D. Goia, N. Pavel, R. E. McLaughlin, L. Tamarkin, *Drug Deliv.* **2004**, *11*, 169-183.
[51] K. J. C. van Bommel, A. Friggeri, D. Mateman, F. A. J. Geurts, K. G. C. van Leerdam, W. Verboom, F. C. J. M. van Veggel, D. N. Reinhoudt, *Adv. Funct. Mater.* **2001**, *11*, 140-146.
[52] a) R. Haag, M. A. Rampi, R. E. Holmlin, G. M. Whitesides, *J. Am. Chem. Soc.* **1999**, *121*, 7895-7906; b) Y.-J. Han, J. Aizenberg, *Angew. Chem. Int. Ed.* **2003**, *42*, 3668-3670.
[53] A. Ulman, *Chem. Rev.* **1996**, *96*, 1533-1554.
[54] D. P. Woodruff, *Phys. Chem. Chem. Phys.* **2008**, *10*, 7211-7221.
[55] a) G. E. Poirier, E. D. Pylant, *Science* **1996**, *272*, 1145-1148; b) H. Kondoh, M. Iwasaki, T. Shimada, K. Amemiya, T. Yokoyama, T. Ohta, M. Shimomura, S. Kono, *Phys. Rev. Lett.* **2003**, *90*, 066102 066101-066104; c) H. Grönbeck, A. Curioni, W. Andreoni, *J. Am. Chem. Soc.* **2000**, *122*, 3839-3842; d) J. Zhang, Chi, J. Ulstrup, *Langmuir* **2006**, *22*, 6203-6213; e) X. Torrelles, E. Barrena, C. Munuera, J. Rius, S. Ferrer, C. Ocal, *Langmuir* **2004**, *20*, 9396-9402.
[56] a) O. Voznyy, J. J. Dubowski, J. T. Yates, P. Maksymovych, *J. Am. Chem. Soc.* **2009**, *131*, 12989-12993; b) P. Maksymovych, D. C. Sorescu, O. Voznyy, J. T. Yates, *J. Am. Chem. Soc.* **2013**, *135*, 4922-4925.
[57] L. Strong, G. M. Whitesides, *Langmuir* **1988**, *4*, 546-558.
[58] A. Ulman, *Acc. Chem. Res.* **2001**, *34*, 855-863.
[59] A. Ulman, *Adv. Mater.* **1990**, *2*, 573-582.
[60] S. R. Wasserman, Y. T. Tao, G. M. Whitesides, *Langmuir* **1989**, *5*, 1074-1087.
[61] N. Subramanian, R. Schmidt, P. M. Wood-Adams, C. E. DeWolf, *Langmuir* **2010**, *26*, 18628-18630.
[62] N. Tillman, A. Ulman, J. S. Schildkraut, T. L. Penner, *J. Am. Chem. Soc.* **1988**, *110*, 6136-6144.
[63] R. Helmy, A. Y. Fadeev, *Langmuir* **2002**, *18*, 8924-8928.
[64] C. R. Kessel, S. Granick, *Langmuir* **1991**, *7*, 532-538.
[65] J. Poppenberg, S. Richter, E. Darlatt, C. H.-H. Traulsen, H. Min, W. E. S. Unger, C. A. Schalley, *Surf. Sci.* **2012**, *606*, 367-377.
[66] C. H.-H. Traulsen, E. Darlatt, S. Richter, J. Poppenberg, S. Hoof, W. E. S. Unger, C. A. Schalley, *Langmuir* **2012**, *28*, 10755-10763.
[67] a) T. P. Sullivan, W. T. S. Huck, *Eur. J. Org. Chem.* **2003**, 17-29; b) C. Haensch, M. Chiper, C. Ulbricht, A. Winter, S. Hoeppener, U. S. Schubert, *Langmuir* **2008**, *24*, 12981-12985.
[68] M. V. Baker, J. D. Watling, *Langmuir* **1997**, *13*, 2027-2032.
[69] a) N. Balachander, C. N. Sukenik, *Langmuir* **1990**, *6*, 1621-1627; b) G. E. Fryxell, P. C. Rieke, L. L. Wood, M. H. Engelhard, R. E. Williford, G. L. Graff, A. A. Campbell, R. J. Wiacek, L. Lee, A. Halverson, *Langmuir* **1996**, *12*, 5064-5075; c) Y. Wang, J. Cai, H. Rauscher, R. J. Behm, W. A. Goedel, *Chem. Eur. J.* **2005**, *11*, 3968-3978; d) Y. Ofir, N. Zenou, I. Goykhman, S. Yitzchaik, *J. Phys. Chem. B* **2006**, *110*, 8002-8009; e) C. Haensch, C. Ott, S. Hoeppener, U. S. Schubert, *Langmuir* **2008**, *24*, 10222-10227.
[70] a) S. Onclin, A. Mulder, J. Huskens, B. J. Ravoo, D. N. Reinhoudt, *Langmuir* **2004**, *20*, 5460-5466; b) A. Heise, M. Stamm, M. Rauscher, H. Duschner, H. Menzel, *Thin Solid Films* **1998**, *327–329*, 199-203.

[71] a) P. M. Dietrich, N. Graf, T. Gross, A. Lippitz, B. Schüpbach, A. Bashir, C. Wöll, A. Terfort, W. E. S. Unger, *Langmuir* **2010**, *26*, 3949-3954; b) N. Graf, A. Lippitz, T. Gross, F. Pippig, A. Holländer, W. E. S. Unger, *Anal. Bioanal. Chem.* **2009**, *396*, 725-738.
[72] B. T. Houseman, E. S. Gawalt, M. Mrksich, *Langmuir* **2003**, *19*, 1522-1531.
[73] a) R. D. Rutledge, C. L. Warner, J. W. Pittman, R. S. Addleman, M. Engelhard, W. Chouyyok, M. G. Warner, *Langmuir* **2010**, *26*, 12285-12292; b) P. Jonkheijm, D. Weinrich, M. Köhn, H. Engelkamp, P. C. M. Christianen, J. Kuhlmann, J. C. Maan, D. Nüsse, H. Schroeder, R. Wacker, R. Breinbauer, C. M. Niemeyer, H. Waldmann, *Angew. Chem. Int. Ed.* **2008**, *47*, 4421-4424.
[74] N. Patel, M. C. Davies, M. Hartshorne, R. J. Heaton, C. J. Roberts, S. J. B. Tendler, P. M. Williams, *Langmuir* **1997**, *13*, 6485-6490.
[75] G. J. Leggett, C. J. Roberts, P. M. Williams, M. C. Davies, D. E. Jackson, S. J. B. Tendler, *Langmuir* **1993**, *9*, 2356-2362.
[76] Y. Luo, M. Piantek, J. Miguel, M. Bernien, W. Kuch, R. Haag, *Appl. Phys. A* **2008**, *93*, 293-301.
[77] E. W. L. Chan, M. N. Yousaf, *J. Am. Chem. Soc.* **2006**, *128*, 15542-15546.
[78] M. N. Yousaf, B. T. Houseman, M. Mrksich, *Angew. Chem. Int. Ed.* **2001**, *40*, 1093-1096.
[79] a) J. P. Collman, N. K. Devaraj, C. E. D. Chidsey, *Langmuir* **2004**, *20*, 1051-1053; b) J. P. Collman, N. K. Devaraj, T. P. A. Eberspacher, C. E. D. Chidsey, *Langmuir* **2006**, *22*, 2457-2464; c) I. F. Gallardo, L. J. Webb, *Langmuir* **2010**, *26*, 18959-18966.
[80] C. Nicosia, J. Huskens, *Mater. Horiz.* **2014**, *1*, 32-45.
[81] H.-J. Himmel, A. Terfort, C. Wöll, *J. Am. Chem. Soc.* **1998**, *120*, 12069-12074.
[82] a) C. W. Tornøe, C. Christensen, M. Meldal, *J. Org. Chem.* **2002**, *67*, 3057-3064; b) V. V. Rostovtsev, L. G. Green, V. V. Fokin, K. B. Sharpless, *Angew. Chem. Int. Ed.* **2002**, *41*, 2596-2599.
[83] a) C. Wendeln, I. Singh, S. Rinnen, C. Schulz, H. F. Arlinghaus, G. A. Burley, B. J. Ravoo, *Chem. Sci.* **2012**, *3*, 2479-2484; b) J. Escorihuela, A. T. M. Marcelis, H. Zuilhof, *Adv. Mater. Interf.* **2015**, *2*, doi: 10.1002/admi.201500135.
[84] a) A. Kumar, G. M. Whitesides, *Appl. Phys. Lett.* **1993**, *63*, 2002-2004; b) A. Kumar, H. A. Biebuyck, G. M. Whitesides, *Langmuir* **1994**, *10*, 1498-1511; c) L. W. James, K. Amit, A. B. Hans, K. Enoch, G. M. Whitesides, *Nanotechnology* **1996**, *7*, 452-457; d) P. Vettiger, U. Staufer, D. P. Kern, Y. Xia, X.-M. Zhao, G. M. Whitesides, *Microelectron. Eng.* **1996**, *32*, 255-268.
[85] H. Schmid, B. Michel, *Macromolecules* **2000**, *33*, 3042-3049.
[86] A. Perl, D. N. Reinhoudt, J. Huskens, *Adv. Mater.* **2009**, *21*, 2257-2268.
[87] D. Wasserberg, C. Nicosia, E. E. Tromp, V. Subramaniam, J. Huskens, P. Jonkheijm, *J. Am. Chem. Soc.* **2013**, *135*, 3104-3111.
[88] D. I. Rozkiewicz, D. Jańczewski, W. Verboom, B. J. Ravoo, D. N. Reinhoudt, *Angew. Chem. Int. Ed.* **2006**, *45*, 5292-5296.
[89] J. J. Richardson, M. Björnmalm, F. Caruso, *Science* **2015**, *348*, aaa2491 2491-2411.
[90] a) A. Winter, S. Hoeppener, G. R. Newkome, U. S. Schubert, *Adv. Mater.* **2011**, *23*, 3484-3498; b) G. de Ruiter, M. Lahav, M. E. van der Boom, *Acc. Chem. Res.* **2014**, *47*, 3407-3416.
[91] L. Cheng, S. Dong, *Electrochem. Commun.* **1999**, *1*, 159-162.
[92] a) V. Piñón, M. Weck, *Langmuir* **2012**, *28*, 3279-3284; b) S. Yang, Y. Zhang, L. Wang, S. Hong, J. Xu, Y. Chen, C. Li, *Langmuir* **2006**, *22*, 338-343.
[93] G. K. Such, J. F. Quinn, A. Quinn, E. Tjipto, F. Caruso, *J. Am. Chem. Soc.* **2006**, *128*, 9318-9319.
[94] G. Decher, *Science* **1997**, *277*, 1232-1237.
[95] H. K. Arslan, O. Shekhah, J. Wohlgemuth, M. Franzreb, R. A. Fischer, C. Wöll, *Adv. Funct. Mater.* **2011**, *21*, 4228-4231.
[96] C. Jiang, S. Markutsya, V. V. Tsukruk, *Adv. Mater.* **2004**, *16*, 157-161.
[97] R. K. Iler, *J. Coll. Interf. Sci.* **1966**, *21*, 569-594.

[98] a) D. Zacher, O. Shekhah, C. Wöll, R. A. Fischer, *Chem. Soc. Rev.* **2009**, *38*, 1418-1429; b) O. Shekhah, H. Wang, S. Kowarik, F. Schreiber, M. Paulus, M. Tolan, C. Sternemann, F. Evers, D. Zacher, R. A. Fischer, C. Wöll, *J. Am. Chem. Soc.* **2007**, *129*, 15118-15119; c) O. Shekhah, H. Wang, M. Paradinas, C. Ocal, B. Schupbach, A. Terfort, D. Zacher, R. A. Fischer, C. Woll, *Nat. Mater.* **2009**, *8*, 481-484; d) O. Shekhah, H. Wang, D. Zacher, R. A. Fischer, C. Wöll, *Angew. Chem. Int. Ed.* **2009**, *48*, 5038-5041; e) O. Shekhah, H. Wang, T. Strunskus, P. Cyganik, D. Zacher, R. Fischer, C. Wöll, *Langmuir* **2007**, *23*, 7440-7442; f) O. Shekhah, H. Wang, D. Zacher, R. A. Fischer, C. Wöll, *Angew. Chem. Int. Ed.* **2009**, *48*, 5038-5041; g) B. Liu, M. Ma, D. Zacher, A. Bétard, K. Yusenko, N. Metzler-Nolte, C. Wöll, R. A. Fischer, *J. Am. Chem. Soc.* **2011**, *133*, 1734-1737; h) O. Shekhah, K. Hirai, H. Wang, H. Uehara, M. Kondo, S. Diring, D. Zacher, R. A. Fischer, O. Sakata, S. Kitagawa, S. Furukawa, C. Woll, *Dalton Trans.* **2011**, *40*, 4954-4958; i) D. Zacher, R. Schmid, C. Wöll, R. A. Fischer, *Angew. Chem. Int. Ed.* **2011**, *50*, 176-199; j) D. Zacher, K. Yusenko, A. Bétard, S. Henke, M. Molon, T. Ladnorg, O. Shekhah, B. Schüpbach, T. de los Arcos, M. Krasnopolski, M. Meilikhov, J. Winter, A. Terfort, C. Wöll, R. A. Fischer, *Chem. Eur. J.* **2011**, *17*, 1448-1455; k) D. Zacher, A. Baunemann, S. Hermes, R. A. Fischer, *J. Mater. Chem.* **2007**, *17*, 2785-2792.

[99] Y. Chaikin, H. Leader, R. Popovitz-Biro, A. Vaskevich, I. Rubinstein, *Langmuir* **2011**, *27*, 1298-1307.

[100] N. Tuccitto, I. Delfanti, V. Torrisi, F. Scandola, C. Chiorboli, V. Stepanenko, F. Würthner, A. Licciardello, *Phys. Chem. Chem. Phys.* **2009**, *11*, 4033-4038.

[101] a) M. Maskus, H. D. Abruña, *Langmuir* **1996**, *12*, 4455-4462; b) T. Kurita, Y. Nishimori, F. Toshimitsu, S. Muratsugu, S. Kume, H. Nishihara, *J. Am. Chem. Soc.* **2010**, *132*, 4524-4525; c) Y. Nishimori, K. Kanaizuka, M. Murata, H. Nishihara, *Chem. Asian J.* **2007**, *2*, 367-376; d) N. Tuccitto, V. Torrisi, M. Cavazzini, T. Morotti, F. Puntoriero, S. Quici, S. Campagna, A. Licciardello, *Chem. Phys. Chem.* **2007**, *8*, 227-230; e) N. Tuccitto, V. Ferri, M. Cavazzini, S. Quici, G. Zhavnerko, A. Licciardello, M. A. Rampi, *Nat. Mater.* **2009**, *8*, 41-46; f) A. Auditore, N. Tuccitto, G. Marzanni, S. Quici, F. Puntoriero, S. Campagna, A. Licciardello, *Chem. Commun.* **2003**, 2494-2495.

[102] K.-i. Terada, H. Nakamura, K. Kanaizuka, M.-a. Haga, Y. Asai, T. Ishida, *ACS Nano* **2012**, *6*, 1988-1999.

[103] M. Altman, A. D. Shukla, T. Zubkov, G. Evmenenko, P. Dutta, M. E. van der Boom, *J. Am. Chem. Soc.* **2006**, *128*, 7374-7382.

[104] P. C. Mondal, J. Yekkoni Lakshmanan, H. Hamoudi, M. Zharnikov, T. Gupta, *J. Phys. Chem. C* **2011**, *115*, 16398-16404.

[105] G. de Ruiter, M. Lahav, G. Evmenenko, P. Dutta, D. A. Cristaldi, A. Gulino, M. E. van der Boom, *J. Am. Chem. Soc.* **2013**, *135*, 16533-16544.

[106] L. Fang, M. Hmadeh, J. Wu, M. A. Olson, J. M. Spruell, A. Trabolsi, Y.-W. Yang, M. Elhabiri, A.-M. Albrecht-Gary, J. F. Stoddart, *J. Am. Chem. Soc.* **2009**, *131*, 7126-7134.

[107] G. Du, E. Moulin, N. Jouault, E. Buhler, N. Giuseppone, *Angew. Chem. Int. Ed.* **2012**, *51*, 12504-12508.

[108] T. Kudernac, N. Ruangsupapichat, M. Parschau, B. Macia, N. Katsonis, S. R. Harutyunyan, K.-H. Ernst, B. L. Feringa, *Nature* **2011**, *479*, 208-211.

[109] R. Eelkema, M. M. Pollard, J. Vicario, N. Katsonis, B. S. Ramon, C. W. M. Bastiaansen, D. J. Broer, B. L. Feringa, *Nature* **2006**, *440*, 163-163.

[110] K.-Y. Chen, O. Ivashenko, G. T. Carroll, J. Robertus, J. C. M. Kistemaker, G. London, W. R. Browne, P. Rudolf, B. L. Feringa, *J. Am. Chem. Soc.* **2014**, *136*, 3219-3224.

[111] U. G. E. Perera, F. Ample, H. Kersell, Y. Zhang, G. Vives, J. Echeverria, M. Grisolia, G. Rapenne, C. Joachim, S. W. Hla, *Nat. Nanotechnol.* **2013**, *8*, 46-51.

[112] Y. Sun, J. Ma, D. Tian, H. Li, *Chem. Commun.* **2016**, *52*, 4602-4612.

[113] L. Luo, X. Zhang, N. Feng, D. Tian, H. Deng, H. Li, *Sci. Rep.* **2015**, *5*, 8982.

[114] L. Luo, G. Nie, D. Tian, H. Deng, L. Jiang, H. Li, *Angew. Chem. Int. Ed.* **2016**, doi: 10.1002/anie.201603906.

[115] D. Patra, H. Zhang, S. Sengupta, A. Sen, *ACS Nano* **2013**, *7*, 7674-7679.

[116] Y. Liu, A. H. Flood, P. A. Bonvallet, S. A. Vignon, B. H. Northrop, H.-R. Tseng, J. O. Jeppesen, T. J. Huang, B. Brough, M. Baller, S. Magonov, S. D. Solares, W. A. Goddard, C.-M. Ho, J. F. Stoddart, *J. Am. Chem. Soc.* **2005**, *127*, 9745-9759.
[117] J. Berná, D. A. Leigh, M. Lubomska, S. M. Mendoza, E. M. Pérez, P. Rudolf, G. Teobaldi, F. Zerbetto, *Nat. Mater.* **2005**, *4*, 704-710.
[118] K. Zhu, C. A. O'Keefe, V. N. Vukotic, R. W. Schurko, S. J. Loeb, *Nat. Chem.* **2015**, *7*, 514-519.
[119] P. R. McGonigal, P. Deria, I. Hod, P. Z. Moghadam, A.-J. Avestro, N. E. Horwitz, I. C. Gibbs-Hall, A. K. Blackburn, D. Chen, Y. Y. Botros, M. R. Wasielewski, R. Q. Snurr, J. T. Hupp, O. K. Farha, J. F. Stoddart, *Proc. Natl. Acad. Sci. USA* **2015**, *112*, 11161-11168.
[120] A. Nefedov, C. Wöll, in *Surface Science Techniques* (Eds.: G. Bracco, B. Holst), Springer, Berlin, Heidelberg, **2013**, pp. 277-303.
[121] M. Altman, O. Zenkina, G. Evmenenko, P. Dutta, M. E. van der Boom, *J. Am. Chem. Soc.* **2008**, *130*, 5040-5041.
[122] a) P. A. DiMilla, J. P. Folkers, H. A. Biebuyck, R. Haerter, G. P. Lopez, G. M. Whitesides, *J. Am. Chem. Soc.* **1994**, *116*, 2225-2226; b) M. Wanunu, R. Popovitz-Biro, H. Cohen, A. Vaskevich, I. Rubinstein, *J. Am. Chem. Soc.* **2005**, *127*, 9207-9215; c) M. Wanunu, A. Vaskevich, I. Rubinstein, *J. Am. Chem. Soc.* **2004**, *126*, 5569-5576; d) N. Katsonis, T. Kudernac, M. Walko, S. J. van der Molen, B. J. van Wees, B. L. Feringa, *Adv. Mater.* **2006**, *18*, 1397-1400.
[123] a) A. D. Shukla, D. Strawser, A. C. B. Lucassen, D. Freeman, H. Cohen, D. A. Jose, A. Das, G. Evmenenko, P. Dutta, M. E. van der Boom, *J. Phys. Chem. B* **2004**, *108*, 17505-17511; b) F. Würthner, T. E. Kaiser, C. R. Saha-Möller, *Angew. Chem. Int. Ed.* **2011**, *50*, 3376-3410.
[124] a) A. Einstein, *Ann. Phys.* **1905**, *322*, 132-148; b) H. Hertz, *Ann. Phys.* **1887**, *267*, 983-1000.
[125] B. D. Ratner, D. G. Castner, in *Surface Analysis – The Principal Techniques*, Wiley, Chichester, UK, **2009**, pp. 47-112.
[126] a) M. Salmeron, R. Schlögl, *Surf. Sci. Rep.* **2008**, *63*, 169-199; b) D. E. Starr, Z. Liu, M. Havecker, A. Knop-Gericke, H. Bluhm, *Chem. Soc. Rev.* **2013**, *42*, 5833-5857.
[127] a) R. Hesse, *Unifit für Windows - Universelles Spektrenbearbeitungs-, Analyse- und Präsentationsprogramm für XPS und XAS (Unifit 2013 Benutzerhandbuch)*, Leipzig, **2012**; b) R. Hesse, Dissertation thesis, Universität Leipzig (Leipzig), **2006**; c) R. Hesse, P. Streubel, R. Szargan, *Surf. Interface Anal.* **2005**, *37*, 589-607; d) E. Darlatt, Dissertation thesis, Freie Universität Berlin (Berlin), **2013**.
[128] Y. Zubavichus, M. Zharnikov, Y. Yang, O. Fuchs, E. Umbach, C. Heske, A. Ulman, M. Grunze, *Langmuir* **2004**, *20*, 11022-11029.
[129] I. Helms*, Vol. 2016*, **2015**.
[130] D. Hübner, F. Holch, M. L. M. Rocco, K. C. Prince, S. Stranges, A. Schöll, E. Umbach, R. Fink, *Chem. Phys. Lett.* **2005**, *415*, 188-192.
[131] J. Stöhr, *NEXAFS Spectroscopy*, Springer, Heidelberg, Germany, **1992**.
[132] S. Richter, J. Poppenberg, C. H.-H. Traulsen, E. Darlatt, A. Sokolowski, D. Sattler, W. E. S. Unger, C. A. Schalley, *J. Am. Chem. Soc.* **2012**, *134*, 16289-16297.
[133] a) A. Benninghoven, *Angew. Chem. Int. Ed. Engl.* **1994**, *33*, 1023-1043; b) D. J. Graham, B. D. Ratner, *Langmuir* **2002**, *18*, 5861-5868; c) S.-J. Xiao, M. Wieland, S. Brunner, *J. Colloid Interf. Sci.* **2005**, *290*, 172-183.
[134] J. C. Vickerman, D. Briggs, *ToF-SIMS - Surface analysis by mass spectrometry*, IM Publications and Surface Spectra Limited, Manchester, UK, **2001**.
[135] E. S. F. Berman, K. S. Kulp, M. G. Knize, L. Wu, E. J. Nelson, D. O. Nelson, K. J. Wu, *Anal. Chem.* **2006**, *78*, 6497-6503.
[136] a) S. Muramoto, D. J. Graham, M. S. Wagner, T. G. Lee, D. W. Moon, D. G. Castner, *J. Phys. Chem. C* **2011**, *115*, 24247-24255; b) M. S. Wagner, D. G. Castner, *Langmuir* **2001**, *17*, 4649-4660.

[137] a) M. Senoner, W. E. S. Unger, *J. Anal. At. Spectrom.* **2012**, *27*, 1050-1068; b) M. Holzweber, A. Lippitz, K. Krueger, J. Jankowski, W. E. S. Unger, *Biointerphases* **2015**, *10*, 019011.
[138] a) I. Singh, C. Wendeln, A. W. Clark, J. M. Cooper, B. J. Ravoo, G. A. Burley, *J. Am. Chem. Soc.* **2013**, *135*, 3449-3457; b) C. Wendeln, B. J. Ravoo, *Langmuir* **2012**, *28*, 5527-5538.
[139] O. Sobol, G. Holzlechner, M. Holzweber, H. Lohninger, T. Boellinghaus, W. E. S. Unger, *Surf. Interface Anal.* **2016**, *48*, 474-478.
[140] G. Binnig, C. F. Quate, C. Gerber, *Phys. Rev. Lett.* **1986**, *56*, 930-933.
[141] G. J. Leggett, in *Surface Analysis – The Principal Techniques*, Wiley, Chichester, UK, **2009**, pp. 479-562.
[142] a) F. J. Giessibl, *Science* **1995**, *267*, 68-71; b) S. Morita, R. Wiesendanger, E. Meyer, *Noncontact Atomic Force Microscopy,* 1 ed., Springer-Verlag, Berlin, **2002**; c) T. R. Albrecht, P. Grütter, D. Horne, D. Rugar, *J. Appl. Phys.* **1991**, *69*, 668-673.
[143] Y. Zhang, H. Kersell, R. Stefak, J. Echeverria, V. Iancu, U. G. E. Perera, Y. Li, A. Deshpande, K. F. Braun, C. Joachim, G. Rapenne, S. W. Hla, *Nat. Nanotechnol.* **2016**, *doi: 10.1038/nnano.2016.69*.
[144] A. Goujon, G. Du, E. Moulin, G. Fuks, M. Maaloum, E. Buhler, N. Giuseppone, *Angew. Chem. Int. Ed.* **2016**, *55*, 703-707.
[145] E. M. Peck, W. Liu, G. T. Spence, S. K. Shaw, A. P. Davis, H. Destecroix, B. D. Smith, *J. Am. Chem. Soc.* **2015**, *137*, 8668-8671.

7. Appendix

7.1. Acknowledgements

First of all, I would like to thank Prof. Dr. Christoph A. Schalley and Dr. Wolfgang E. S Unger for giving me the opportunity to elaborate a very interesting topic in their working groups during the course of my doctoral studies. Their support, advice and trust enabled me to approach, plan, and coordinate the presented research in an autonomous and independent fashion.

I also thank Prof. Dr. Rainer Haag for accepting to be the second referee of my thesis.

My thanks go to all the group members of the Schalley and Unger groups for great teamwork and a very nice working atmosphere. Special thanks goes to the Schalley surface “sub”-group: Dr. Sebastian Richter, Dr. Johannes Poppenberg, Dr. Christoph H.-H. Traulsen, Felix B. Schwarz and Valentin Kunz supported me the whole time with numerous fruitful discussions and a lot of advice. It was always fun to work with them and at last, resulted in a very productive research project. The support from my many students (Frenio A. Redecker, Sarah K. Kastner, Valentin Popov, Sebastian Pochert, Franz-Lucas Haut, Charlene Leppich, and Ivan Ilic) doing their theses and internships in the course of my work is gratefully acknowledged. For their synthetic contribution, I also thank Nora L. Traulsen and Igor Linder.

I would also like to acknowledge the kind help of the NMR and MS department, Dr. Andreas Schäfer, Dr. Andreas Springer and their co-workers, for numerous NMR and MS measurements. I thank Sebastian Müller for his help in separation and synthetic problems and Andrea Schulz for a lot of AFM measurements.

I would also like to thank Dr. Erik Darlatt who introduced me to new analytical methods. I want to thank Dr. Markus Holzweber with whom I had a lot of interesting discussions about our mutual research and who conducted as well as interpreted countless ToF-SIMS spectra. I also thank Dr. Thomas Gross and Dieter Treu for the measurement of numerous XP-spectra at the Kratos XPS instrument. Thanks further goes to Andreas Lippitz who helped me with the ESCA instrument at BAM and during our many measurements at BESSY II. I moreover thank Dr. Paul Dietrich, Carolin Nietzhold, Henryk Kalbe, and Nele Lange for their support during the measurements at BESSY II.

I furthermore thank Dr. A. Nefedov (Karlsruhe Institute of Technology, KIT) from the HE-SGM collaborate research group at BESSY II and Dr. O. Schwartzkopf, Dr. A. Vollmer and M. Mast (all BESSY II) for support during our activities at HZB.

Last but not least, I thank my whole family, and especially my girlfriend and my little son who were there for me whenever I needed them and made this work possible with their patience, love, and support.

7.2. Curriculum Vitae

The curriculum vitae is not available online
due to privacy policies.

7.3. Publications

Peer-Review Journal Articles

1. *Programmable, Ordered Multilayers of Nanometer-Sized Macrocycles in Solid Support and Stimuli-Controlled On-Surface Pseudorotaxane Formation*
J. Poppenberg, S. Richter, C. H.-H. Traulsen, E. Darlatt, B. Baytekin, T. Heinrich, P. M. Deutinger, K. Huth, W. E. S. Unger, C. A. Schalley, *Chem. Sci*. **2013**, *4*, 3131-3139.

2. *Sequence-Programmable Multi-Component Multilayers of Nanometer-Sized Tetralactam Macrocycles on Gold Surfaces*
S. Richter, C. H.-H. Traulsen, T. Heinrich, J. Poppenberg, C. Leppich, M. Holzweber, W. E. S. Unger, C. A. Schalley *J. Phys. Chem. C* **2013**, *117*, 18980–18985.

3. *Synthesis and Coordinative Layer-by-Layer Deposition of Pyridine-Functionalized Gold Nanoparticles and Tetralactam Macrocycles on Silicon Substrates*
C. H.-H. Traulsen, V. Kunz, T. Heinrich, S. Richter, M. Holzweber, A. Schulz, L. K. S. von Krbek, J. Poppenberg, U. T. J. Scheuschner, W. E. S. Unger, C. A. Schalley *Langmuir* **2013**, *29*, 14284-14292.

4. *The versatility of „click" reactions: molecular recognition at interfaces*
T. Heinrich, C. H.-H. Traulsen, E. Darlatt, S. Richter, J. Poppenberg, N. L. Traulsen, I. Linder, A. Lippitz, P. M. Dietrich, B. Dib, W. E. S. Unger, and C. A. Schalley *RSC Adv.* **2014,** *4*, 17694-17702.

5. *Principal Component Analysis (PCA)-Assisted Time-of-Flight Secondary-Ion Mass Spectrometry (Tof-SIMS): A Versatile Method for the Investigation of Self-Assembled Monolayers and Multilayers as Precursors for the Bottom-Up Approach of Nanoscaled Devices*
M. Holzweber, T. Heinrich, V. Kunz, S. Richter, C. H.-H. Traulsen, C. A. Schalley, W. E. S. Unger *Anal. Chem.* **2014,** *86*, 5740-5748.

6. *Gas-Phase Chemistry of Molecular Containers*
Z. Qi, T. Heinrich, M. Suresh, C. A. Schalley *Chem. Soc. Rev.* **2015**, *44,* 515-531.

7. Coupled Molecular Switching Processes in Ordered Mono- and Multilayers of Stimulus-Responsive Rotaxanes on Gold Surfaces
T. Heinrich, C. H.-H. Traulsen, M. Holzweber, S. Richter, V. Kunz, S. K. Kastner, S. O. Krabbenborg, J. Huskens, W. E. S. Unger, C. A. Schalley *J. Am. Chem. Soc.* **2015**, *137*, 4382–4390.

8. *Photocontrolled On-Surface Pseudorotaxane Formation with Well-Ordered Macrocycle Multilayers*
F. B. Schwarz, T. Heinrich, J. O. Kaufmann, A. Lippitz, R. Puttreddy, K. Rissanen, W. E. S. Unger, C. A. Schalley *Chem. Eur J.* **2016**, accepted for publication.

Talks

1. “Synthesis and ordered deposition of macrocycles and switchable rotaxanes on gold surfaces.” G4 – Joint Meeting on Supramolecular Chemistry, Berlin, Aug. 23rd, 2013.

2. “Concerted switching of stimuli-responsive rotaxanes on surfaces.” G4 – Joint Meeting on Supramolecular Chemistry, Bonn, Aug. 18th, 2015.

3. “(Coupled) Molecular Switching Processes in Ordered Mono- and Multilayers of Stimuli-Responsive Rotaxanes on solid supports” PhD student’s day of the SFB 765 Multivalency, Berlin, March 17th 2016.

4. “Programmable multilayers and concerted switching of rotaxanes on surfaces” FUB-DU Joint Research Workshop on Supramolecular Chemistry and Nanoscale Systems, Berlin, June 9th 2016.

Poster Presentations

1. T. Heinrich, C. H.-H. Traulsen, M. Holzweber, S. Richter, S. K. Kastner, W. E. S. Unger, C. A. Schalley "Coupled Molecular Switching Processes in Ordered Mono- and Multilayers of Stimuli-Responsive Rotaxanes on Gold Surfaces", SupraChem **2015**, Berlin/Germany, Feb. 24th.

2. T. Heinrich, C. H.-H. Traulsen, M. Holzweber, S. Richter, W. E. S. Unger, C. A. Schalley "Coupled Molecular Switching Processes in Ordered Mono- and Multilayers of Stimuli-Responsive Rotaxanes on Gold Surfaces", Gordon Research Conference **2015**, Easton MA/USA, June 7th – 12th.

3. T. Heinrich, C. H.-H. Traulsen, M. Holzweber, S. Richter, S. K. Kastner, W. E. S. Unger, C. A. Schalley "Chemically Induced Switching of Rotaxane Mono- and Multilayers between two Ordered States", Tag der Chemie **2015**, Berlin/Germany, June 18th.

4. T. Heinrich, C. H.-H. Traulsen, M. Holzweber, B. Dib, W. E. S. Unger, C. A. Schalley, “The influence of the rotaxane-design to the occurring of coupled molecular switching processes”, BESSY-II user-meeting **2015**, Berlin/Germany, December 10th.

7.4. Prints of the Published Works

7.4.1. Programmable multilayers of nanometer-sized macrocycles on solid support and stimuli-controlled on-surface pseudorotaxane formation

J. Poppenberg, S. Richter, C. H.-H. Traulsen, E. Darlatt, B. Baytekin, T. Heinrich, P. M. Deutinger, K. Huth, W. E. S. Unger, C. A. Schalley
Chem. Sci. **2013**, *4*, 3131−3139.

Submitted 26 February 2013, published 15 May 2013.

The journal article is electronically available (http://dx.doi.org/10.1039/C3SC50558H).

7.4.2. Principal Component Analysis (PCA)-Assisted Time-of-Flight Secondary-Ion Mass Spectrometry (Tof-SIMS): A Versatile Method for the Investigation of Self-Assembled Monolayers and Multilayers as Precursors for the Bottom-Up Approach of Nanoscaled Devices

Markus Holzweber, Thomas Heinrich, Valentin Kunz, Sebastian Richter, Christoph H.-H. Traulsen, Christoph A. Schalley, and Wolfgang E. S. Unger
Anal. Chem. **2014**, *86*, 5740–5748.

Submitted 6 January 2014, published 15 May 2014.

The journal article is electronically available (http://dx.doi.org/10.1021/ac500059a).

7.4.3. Sequence-Programmable Multicomponent Multilayers of Nanometer-Sized Tetralactam Macrocycles on Gold Surfaces

Sebastian Richter, Christoph H.-H. Traulsen, Thomas Heinrich, Johannes Poppenberg, Charlene Leppich, Markus Holzweber, Wolfgang E. S. Unger, and Christoph A. Schalley
J. Phys. Chem. C **2013**, *117*, 18980–18985.

Submitted 4 June 2013, published 19 August 2013.

The journal article is electronically available (http://dx.doi.org/10.1021/jp405492v).

7.4.4. Synthesis and Coordinative Layer-by-Layer Deposition of Pyridine-Functionalized Gold Nanoparticles and Tetralactam Macrocycles on Silicon Substrates

Christoph H.-H. Traulsen, Valentin Kunz, Thomas Heinrich, Sebastian Richter, Markus Holzweber, Andrea Schulz, Larissa K. S. von Krbek, Ulf T. J. Scheuschner, Johannes Poppenberg, Wolfgang E. S. Unger, and Christoph A. Schalley
Langmuir **2013**, *29*, 14284–14292.

Submitted 20 August 2013, published 25 October 2013.

The journal article is electronically available (http://dx.doi.org/10.1021/la403222x).

7.4.5. The versatility of „click“ reactions: molecular recognition at interfaces

Thomas Heinrich, Christoph H.-H. Traulsen, Erik Darlatt, Sebastian Richter, Johannes Poppenberg, Nora L. Traulsen, Igor Linder, Andreas Lippitz, Paul M. Dietrich, Baha Dib, Wolfgang E. S. Unger, and Christoph A. Schalley
RSC Adv. **2014**, *4*, 17694−17702.

Submitted 27 February 2014, published 31 March 2014.

The journal article is electronically available (http://dx.doi.org/10.1039/C4RA01730G).

7.4.6. Photocontrolled On-Surface Pseudorotaxane Formation with Well-Ordered Macrocycle Multilayers

Felix B. Schwarz, Thomas Heinrich, J. Ole Kaufmann, Andreas Lippitz, Rakesh Puttreddy, Kari Rissanen, Wolfgang E. S. Unger, and Christoph A. Schalley
Chem. Eur J. **2016**, *22*, 14383-14389.

Submitted 01 July 2016, accepted 01 August 2016.

The journal article is electronically available (http://dx.doi.org/10.1002/chem.201603156).

7.4.7. Coupled Molecular Switching Processes in Ordered Mono- and Multilayers of Stimulus-Responsive Rotaxanes on Gold Surfaces

Thomas Heinrich, Christoph H.-H. Traulsen, Markus Holzweber, Sebastian Richter, Valentin Kunz, Sarah K. Kastner, Sven O. Krabbenborg, Jurriaan Huskens, Wolfgang E. S. Unger, and Christoph A. Schalley

J. Am. Chem. Soc. **2015**, 137, 4382–4390.

Submitted 12 December 2014, published 17 March 2015.

The journal article is electronically available (http://dx.doi.org/10.1021/ja512654d).

A copy of the original work is not included in the online version due to restrictions by the publisher.